Chapter 4

Sulfur K-edge X-ray Absorption Studies of Electronic Structural Variation in Perturbed Blue Copper Sites

4.1. Introduction

Blue copper centers are characterized spectroscopically by a very intense absorption band in the visible region (~600 nm, $\varepsilon > 3000\ M^{-1}cm^{-1}$), and by a small $A_{||}$ hyperfine splitting ($\sim 60 \times 10^{-4}\ cm^{-1}$) in the $g_{||}$ region of EPR spectra. The intense optical absorption (~600 nm) which gives blue copper proteins their color has been assigned as a S(Cys) $p_\pi \longrightarrow d_{x^2-y^2}$ ligand-to-metal charge transfer (CT) transition.[1,2] The small $A_{||}$ EPR hyperfine splitting has been shown to be a result of an unusually covalent Cu-S(Cys) bond (see Chapter 3). Blue copper sites have also been extensively investigated using resonance Raman (rR) spectroscopy.[3,4] The dominant rR frequency is generally at ~400 cm^{-1}. While many modes contribute to this vibration, it is ascribed primarily to the Cu-S(Cys) stretch and reflects the strength of the Cu-S(Cys) bond. These spectroscopic characteristics are in contrast to normal copper which displays an optical absorption spectrum with Abs ~450 nm > Abs ~630 nm, an EPR $A_{||}$ splitting $>120 \times 10^{-4}\ cm^{-1}$, and, for normal Cu-thiolate complexes, a lower Cu-S rR frequency than for blue copper.[5]

Blue copper sites most commonly serve a role in electron transfer and can be found in metalloproteins both as mononuclear centers and as one of a number of metal active sites in a system.[5,6] X-ray crystal structure determinations[6] of blue copper proteins have revealed a highly conserved site in which a copper ion is coordinated by one cysteine sulfur and two histidine nitrogens in a nearly trigonal array, with a longer bond to an axial ligand (usually methionine) (see Figure 4.1a). The most unusual structural feature of blue copper sites is a very short Cu-S(Cys) bond length.

While both the spectroscopic and structural features of blue copper sites are highly conserved, important variations in the structures, redox properties, and spectroscopic characteristics are observed for these sites. Table 4.1 provides an abbreviated summary of active site structural parameters for blue copper (and blue copper containing) proteins relevant to this study. For a more comprehensive review of structural similarity and variation, the reader is directed to reference 6. Table 4.2 provides a summary of the reduction potentials and spectral features of copper sites included in this study. The reduction potentials for known blue copper sites range from 184 mV in stellacyanin[7] to 785 mV for the blue (Type 1) site in fungal laccase.[7]

In addition to the dominant optical absorption at ~600 nm, all blue copper sites also exhibit an absorption at ~450 nm, which is generally much less intense than the absorption at ~600 nm. Blue copper centers which exhibit increased absorption at ~450 nm are categorized as perturbed sites. The magnetic circular dichroism (MCD) of blue copper sites has demonstrated that several transitions contribute intensity to this

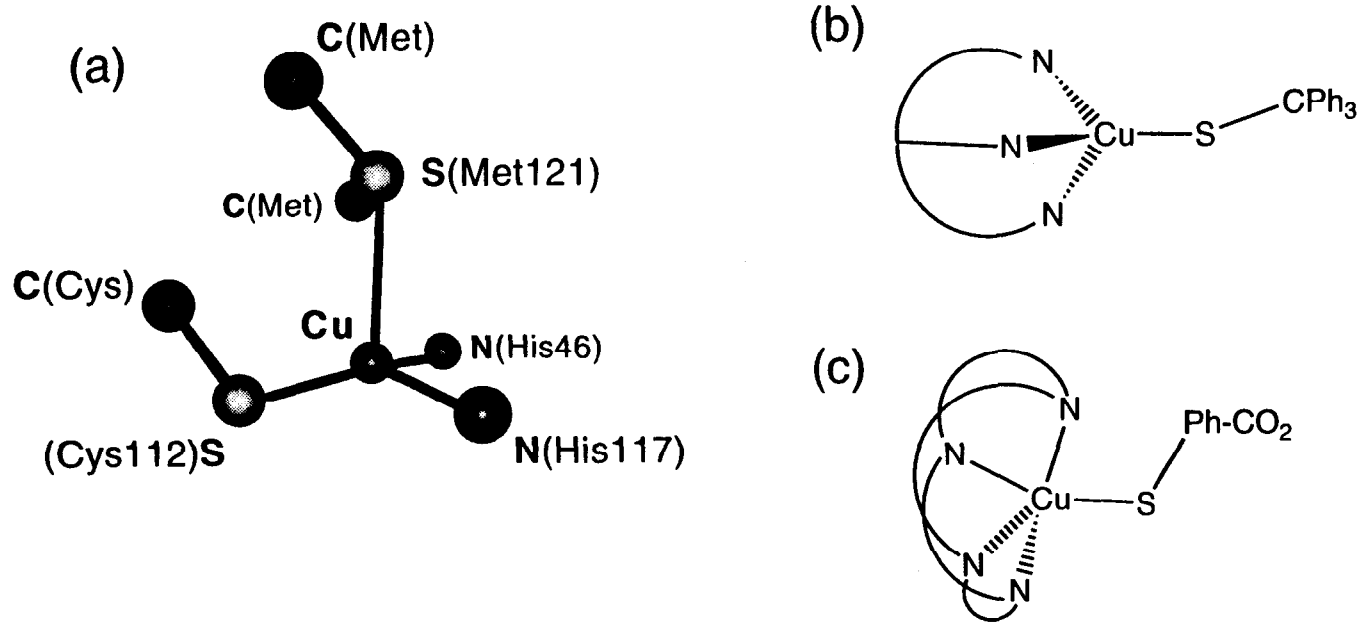

Figure 4.1. Schematic representations of the structures of (a) a blue copper protein active site with residues labeled according to the backbone of azurin, (b) LCu(SCPh$_3$) and (c) Cu-tet *b*.

Table 4.1. Summary of Bond Distances[a] and Coordination in Blue Copper Proteins and Cu-thiolate Model Compounds

Protein	Abbrev.	Cu-S(Cys)	Cu-N(His)	Cu-N(His)	Cu-S*(Met) (apical)	Cu-N_2S Plane	Ref.
Poplar Plastocyanin	Pc	2.07	1.91	2.06	2.82	0.36	*c*
Pseudomonas aeruginosa							
Wild Type Azurin (ave)[b]	*Pa*WT	2.25	2.03	2.11	3.15	0.10	*d*
His35Gln	H35Q	2.05	2.03	2.05	3.04	0.10	*e*
Alcaligenes denitrificans							
Wild Type Azurin	*Ad*WT	2.15	2.08	2.00	3.11	0.12	*f*
Met121Gln (ave)[b]	M121Q	2.12	1.93	2.04	2.26	0.26	*g*
Rhus vernicifera Stellacyanin [EXAFS]	Stella	2.21	1.93	1.93			*h*
Achromobacter cycloclastes Nitrite Reductase	NiR	2.17	2.06	2.05	2.59	0.54	*i*
Model Complex		**Cu-SR**	**Cu-N_1**	**Cu-N_2**	**Cu-N_3**	**Cu-N_2S Plane**	**Ref.**
$Cu(SCPh_3)[HB(3,5\text{-}i\text{-}Pr_2pz_3)]$	$LCu(SCPh_3)$	2.12	1.97	2.03	2.05	0.20	*j*
$[(Cu\text{-tet } b)(o\text{-}SC_6H_4CO_2)]\cdot H_2O$	Cu-tet *b*	2.36	2.03	2.19	2.00	--	*k*

[a] All distances are given in Ångströms.
[b] Values given are the average for the two molecules in the asymmetric unit in the crystal structure.
[c] Guss, J. M.; Freeman, H. C. *J. Mol. Biol.* **1983**, *169*, 521-563.
[d] Adman, E. T.; Jensen, L. H. *Israel. J. Chem.* **1981**, *21*, 8-12.
[e] Ref. 34.
[f] Baker, E. N. *J. Mol. Biol.* **1988**, *203*, 1071-1095.
[g] Ref. 22.
[h] Feiters, M. C.; Dahlin, S.; Reinhammar, B. *Biochim. Biophys. Acta* **1988**, *955*, 250-260.
[i] Adman, E. private communication.
[j] Ref. 36.
[k] Ref. 38.

Table 4.2. Reduction Potentials and Spectroscopic Parameters for Blue Copper Proteins and Cu-thiolate Model Complexes.

Sample	Abbreviation	E_0 (mV)[a]	Blue Band[b] λ_{max}, nm (ε, $M^{-1}cm^{-1}$)	Green Band[b] λ_{max}, nm (ε, $M^{-1}cm^{-1}$)	EPR $A_{\parallel}$ (x 10^{-4} cm^{-1})	rRaman Cu-thiolate stretching frequency (cm^{-1})	Ref.
Spinach Plastocyanin	Pc	370	597 (4500)	467 (400)	63 (ax)	424 (poplar)	*h,i*
Pseudomonas aeruginosa Wild Type Azurin	*Pa*WT	308	631 (3800)	466 (200)	58 (ax)	408	*h.i*
Alcaligenes denitrificans Wild Type Azurin	*Ad*WT	276	619 (5100)	460 (580)	60 (ax)	413	*h*
His117Gly(Cu)	H117G(Cu)		628 (14%)	420 (19%)	-/139 (ax)[c]	317/399[c]	*j*
His117Gly(Hista)	H117G(Hista)		634 (10%)	402 (40%)	78/162 (ax)[c]	319/406[c]	*j*
His117Gly(Im)	H117G(Im)		626 (> 4500)	460 (200)	85 (ax)	408	*j*
Rhus vernicifera Stellacyanin (low pH)	Stella(LO)	184	609 (3400)	443 (1100)	37 (rh)	385	*h*
Stellacyanin (high pH)	Stella(HI)		~590[d]	~420[d]	<17 (rh)	similar to Stella(LO)	*k*
Alcaligenes denitrificans Met121Gln Azurin	M121Q	~250	610 (6000)	452 (1200)	35 (rh)	373	*l*
Achromobacter cycloclastes Nitrite Reductase	NiR		585 (1800)	458 (2200)	73 (ax)	361	*m*
Pseudomonas aeruginosa His35Gln Azurin	H35Q	268	628 (5500)[e]				*n*
Cu($SCPh_3$) - [$HB(3,5\text{-}i\text{-}Pr_2pz_3)$]	LCu($SCPh_3$)	-540[f]	608 (>3500)[f]	349 (1100)[f]	70[f]	422	*o*
[(Cu-tet *b*) - (*o*-$SC_6H_4CO_2$)]·H_2O	Cu-tet *b*		432 (~1000)	360 (~2200)	~125[g]		*p*

[a] E_0 has not been measured for those samples for which it is not reported. [b] Extinction coefficients reported as percentages refer to the intensity of the band as a percentage of the 280 nm absorption. [c] The first value reported is for the dominant T2 species in solution, the second value corresponds to the T1 species. [d] Intensities in Stella(HI) are similar to those in Stella(LO). [e] The UV/Vis absorption is very similar to that of *Pa*WT as measured by the same researchers (see Ref. 33). [f] E_0 measured *vs.* Ag wire in CH_2Cl_2; spectra data (except rR) given for t-butyl thiolate. [g] H. Schugar, private communication. [h] Ref. 5. [i] Ref. 8. [j] Refs. 13, 16. [k] Ref. 17. [l] Ref. 22. [m] Liu, M.-Y.; Liu, M.-C.; Payne, W.; LeGall, J. *J. Bacteriol.* **1986**, *166*, 604-608 and Ref. 10. [n] Ref. 33. [o] Refs. 37, 54. [p] Ref. 38.

absorption.[8] However, transitions in this region have not been definitively assigned. The S(Cys) pseudo-σ —> Cu CT transition[9] has been assigned to a feature at ~550 nm,[1] but has also been proposed to contribute to the intensity at ~450 nm.[10] N(His) —> Cu CT and/or S(Met) —> Cu CT transitions will also contribute intensity in the ~450 nm region.[1]

Another spectroscopic feature of perturbed blue copper is a rhombic, rather than axial EPR signal, as well as larger EPR A_x hyperfine splitting values. The electronic structural origin of this rhombic distortion has not been definitively established, but is associated with a lower site symmetry relative to those sites which display axial EPR spectra.[11]

As described in Chapter 1 (Section 1.2.4) and demonstrated in Chapter 3 for the blue copper protein plastocyanin (Section 3.3.2.2), the ligand K-edge X-ray absorption spectrum (XAS) of a ligand bound to an open-shell metal ion exhibits a well-resolved pre-edge feature which is assigned as a ligand 1s —> ψ^*, where ψ^* is an antibonding molecular orbital containing both ligand 3p and metal d-character. In the case of d^9 Cu(II), the intensity of this feature is directly proportional to the covalency of the absorbing ligand in the half-occupied molecular orbital (see equation 1.3c) and provides a direct probe of the covalency of the M-L bond.

Because the Cu-S(Cys) bonding interaction dominates the electronic structure (and therefore the spectroscopy), examination of the Cu-S bonding should provide valuable insight into variations in the electronic structure and reactivity of blue copper sites. To this end, the S K-edge XAS have been measured for a series of blue copper sites as well as sites created by site-directed mutagenesis which have been specifically designed to (i) examine various aspects of the native protein active sites and/or (ii) act as active site models for native proteins which have proved difficult to study by X-ray crystallography. This spectroscopic probe of Cu-S(Cys) covalency is especially important in the investigation of blue copper sites because it provides insight into the electronic structure of the half-occupied highest-occupied-molecular-orbital (HOMO) involved in the electron transfer reactivity of the site.

A brief description of each of the sites included in this study is provided here. A summary of the abbreviations used for the samples is provided in Table 4.2.

Plastocyanin (Pc) and azurin are among the most well-characterized of the blue copper proteins and therefore serve as a basis for comparison for all other systems. They will be referred to throughout this Chapter as the "classic" blue copper sites. Figure 4.1a shows a schematic of the blue copper active site, with the residues labeled according the peptide backbone of azurin. The EPR of both Pc and azurin is axial and the absorption

intensity at ~450 nm is small compared to that at ~600 nm. The rR Cu-S(Cys) stretch ranges from 408-424 cm^{-1}. The azurins have an additional glycine carbonyl oxygen residue in proximity to the Cu, but it is too distant (~3 Å) to be considered to have a bonding interaction.[12]

The His117 ligand of azurin (see Figure 4.1a) can be replaced by glycine using site-directed mutagenesis to create H117G azurin.[13] The replacement creates an open coordination site on the copper and allows exogenous ligands to bind at the active site.[14] Addition of a bidentate ligand like histamine produces a species with optical absorption, EPR and rR indicative of normal copper (see Table 4.2). This suggests that the equatorial plane of the Cu accommodates four ligands, generating a tetragonal site. In the absence of exogenous ligands, the site also exhibits normal copper spectroscopy. It is thus assumed that there are two water molecules bound in the Cu equatorial plane. Addition of a single monodentate ligand, such as imidazole, to the H117G protein generates spectral properties consistent with those of a blue copper site. Each of these H117G species actually exist as a mixture of blue and normal copper sites. However, addition of imidazole results in a solution dominated by blue sites,[15] while no ligand or addition of histamine produces mostly normal sites.[16]

Stellacyanin (Stella) exhibits a rhombic EPR pattern and its optical absorption at ~450 nm is significantly increased relative to Pc and azurin. The rR Cu-S(Cys) stretch is lower than for the classic blue copper centers. Stella differs from Pc and azurin in that the protein peptide chain lacks a methionine[17] to serve as the axial ligand (see Figure 4.1a). Stella has not been characterized by X-ray crystallography and it has been suggested[18-20] that the axial position in Stella is occupied by an oxygen-bound glutamine residue. While the origin of the rhombic distortion is not established, a rotation of the HOMO in Stella (relative to that in Pc), which would mix in ~5% d_{z2} character has been proposed to explain the splitting.[11]

Stella also exists in a high pH form (at pH ~11) (Stella(HI)) with spectral properties which differ slightly from the low pH form (Stella(LO)).[17] A pulsed ENDOR study has suggested that an amide nitrogen acts as the axial ligand at high pH.[21] Since the nitrogen is not indicated at low pH, the result is consistent with a linkage isomerization of the glutamine residue: carbonyl oxygen providing the ligation at lower pH and a deprotonated amide at higher pH.[21]

The axial methionine ligand of *A. denitrificans* azurin has been replaced, through site-directed mutagenesis, with glutamine, the purported fourth ligand in stellacyanin, to produce M121Q azurin.[22] M121Q azurin has been crystallographically characterized[22] and its structural parameters are summarized in Table 4.1. The spectroscopy of this

mutant is remarkably consistent with that of native stellacyanin.[22,23] The reduction potential of the site is lower than in the wild type (WT) azurin.[22]

Nitrite Reductase (NiR) from *Achromobacter cycloclastes* is involved in the denitrification process and is responsible for the sequential reduction of nitrite to nitric oxide and nitrous oxide (NO_2^- —> NO —> N_2O).[24] The protein contains one normal copper center (at which the reduction of NO_2^- is believed to occur[25,26]) as well as one blue copper center per subunit. It is the blue site which dominates the spectroscopy of the protein[27] and which exhibits features significantly perturbed from those of Pc and azurin. In the optical absorption spectrum of NiR the feature at ~450 nm is more intense than that at ~600 nm. The most intense frequency in the rR spectrum of NiR is at lower frequency than the classic blue copper centers. However, the EPR of NiR is typical of blue copper[27] (see Table 4.2).

The path of electron transfer for blue copper centers has been studied extensively.[28,29] One proposed pathway for electron transfer in azurin involves His35, which is bound to the ligating His46 residue.[30-32] To understand how a mutation at residue 35 would effect the redox and spectroscopic properties of the site, His35 was replaced with glutamine in *P.a.* azurin using site directed mutagenesis.[33] This H35Q azurin has been structurally characterized and has an active site very similar to that in the WT protein.[34] Further, the absorption and EPR spectra of the site are very similar to those of the WT protein.[33] However, the MCD spectrum of H35Q azurin does show small perturbations relative to the WT protein.[35]

It is often useful to compare proteins to model compounds which are designed to mimic the active site properties of a protein. A schematic of the structure of $LCu(SCPh_3)$, L=$(HB(3,5\text{-}i\text{-}Pr_2pz)_3)$, which has spectroscopic properties similar to blue copper (see Table 4.2), is shown in Figure 4.1b. The copper is bound in approximately T_d geometry by a tridentate tris-pyrazolylborate ligand providing three nitrogen ligands, with a fourth coordination site occupied by a thiolate having a short bond to the Cu (see Table 4.1).

To serve as a contrast to the blue copper sites, the Cu-thiolate complex, $[Cu(\text{tet } b)(o\text{-}SC_6H_4CO_2)]\cdot H_2O$ (Cu-tet *b*) has also been examined. Cu-tet *b* , shown schematically in Figure 4.1c, is ligated by a thiolate sulfur at 2.36 Å from the copper and four nitrogen ligands in a distorted 5-coordinate geometry. It exhibits spectroscopic features consistent with normal copper (see Table 4.2).

S K-edge XAS measurements on each of these proteins and model compounds should provide important insight into the electronic structure variations in blue copper sites.

4.2. Experimental

4.2.1. Sample Preparation

$Na_2S_2O_3 \cdot 5H_2O$ was purchased from J.T. Baker and used without further purification.

The model complex $LCu(SCPh_3)$, L=($HB(3,5\text{-}i\text{-}Pr_2pz)_3$), was a gift of Prof. Nobumasa Kitajima and was synthesized as described previously.[36,37] The sample of $[Cu(tet\ b)(o\text{-}SC_6H_4CO_2)] \cdot H_2O$ was provided by Prof. Harvey Schugar and was synthesized as described in the literature.[38]

Plastocyanin was isolated from spinach chloroplasts according to published methods.[39] *Rhus vernicifera* stellacyanin (low pH form) was prepared as described in the literature.[40] High pH (pH=10.25) stellacyanin was prepared by dialysis against 100 mM carbonate buffer overnight. This buffer system was chosen because it contains no sulfur which would interfere with the experiment.

Nitrite Reductase from *Achromobacter cycloclastes* was prepared according to literature methods[27] and was provided for these measurements by Prof. Bruce Averill.

Pseudomonas aeruginosa wild type azurin[33,41] and its mutants H117G(Cu), H117G(Hista), H117G(Im),[13,14] and H35Q[33] as well as *Alcaligenes denitrificans* wild type azurin[42] and its M121Q mutant[22] were gifts of Prof. Gerard Canters and were prepared according to published methods.

Table 4.3 summarizes the experimental conditions (buffer medium and pH) for each protein sample for which XAS data were measured.

All S K-edge measurements were made at ~4°C. The sample temperature was controlled with a cryostat which utilized liquid nitrogen-cooled gases. The solid $LCuSCPh_3$ sample, which was prepared in inert atmosphere, was ground to a fine powder which was thinly dispersed on mylar tape (containing an acrylic adhesive determined to be free of sulfur contaminants) and mounted on a cooled Al spacer sample holder. During measurement the sample space was purged with cold He gas. The protein solutions were pre-equilibrated in a buffer-saturated He atmosphere for ~1 hour to minimize bubble formation in the sample cell. Protein solutions were loaded via syringe into an Al block sample holder sealed in front by a 6.35 μm thick polypropylene window. UV/Vis spectroscopy was used to verify the integrity of the samples both before and after exposure to the X-ray beam.

The H35Q azurin mutant sample photoreduced in the X-ray beam. This was verified by UV/Vis spectra of the sample. Addition of an excess of potassium

Table 4.3. Summary of Experimental Conditions for Blue Copper Protein Samples

Sample	Experimental Conditions
Plastocyanin (Spinach)	50 mM phosphate buffer, pH = 7.6
Pseudomonas aeruginosa	
wild type azurin	20 mM phosphate buffer, pH = 6.9; 50% glycerol
His117Gly(Cu) azurin	20 mM phosphate buffer, pH = 6.95; 50% glycerol
His117Gly(Hista) azurin	20 mM phosphate buffer, pH = 6.92; 50% glycerol
His117Gly(Im) azurin	20 mM phosphate buffer, pH = 6.2; 50% glycerol
His35Gln azurin	20 mM phosphate buffer, pH = 7.0
Alcaligenes denitrificans	
wild type azurin	20 mM phosphate buffer, pH = 7.0; 50% glycerol
Met121Gln azurin	20 mM phosphate buffer, pH = 7.0; 50% glycerol
Rhus vernicifera	
Stellacyanin (low pH)	10 mM phosphate buffer, pH = 6.0
Stellacyanin (high pH)	100 mM carbonate buffer, pH = 10.25
Achromobacter cycloclastes	
Nitrite Reductase	0.1M Tris-HCl pH = 7

ferricyanide reoxidized the sample. Only scans in which a clear excess of K_3FeCl_6 was present were used to generate an average spectrum.

4.2.2. X-ray Absorption Measurements and Data Acquisition Parameters

All data were collected at the Stanford Synchrotron Radiation Laboratory under dedicated conditions (3.0 GeV, ~50 mA). Sulfur K-edge data for the model compounds included in the study and for plastocyanin and stellacyanin was measured using the 54-pole wiggler beam line 6-2 in low magnetic field mode (5 kG) with a Pt focusing mirror, and a Si(111) double crystal monochromator. The monochomator was detuned ~30% to eliminate higher harmonic components in the X-ray beam. All other sulfur K-edge data were measured using the 54-pole wiggler beam line 6-2 in low magnetic field mode (5 kG), a Ni-coated, flat harmonic rejection mirror, and a Si(111) double crystal monochromator. Details of the optimization of this line for low energy studies are described in Chapter 1 (Section 1.2.5) as well as in an earlier publication.[43]

The data were collected as fluorescence excitation spectra utilizing an ionization chamber as fluorescence detector.[44,45] The energy was calibrated from the S K-edge spectra of $Na_2S_2O_3 \cdot 5H_2O$, run at intervals between the samples. The maximum of the first pre-edge feature in the spectrum was assigned to 2472.02 eV. Data were collected from 2420 to 2740 eV, with a step size of 0.08 eV in the edge region. The spectrometer resolution was ~0.5 eV.[43] A reproducibility in edge position determination of ~0.1 eV for these experiments was obtained by calculating and comparing first and second derivatives for model compounds measured during different experimental sessions.

4.2.3. Data Reduction

A smooth pre-edge background was removed from all spectra by fitting a polynomial to the pre-edge region and subtracting this polynomial from the entire spectrum. Normalization of the data was accomplished by fitting a flat polynomial or straight line to the post-edge region and normalizing the edge jump to 1.0 at 2490 eV for the sulfur edges. Data represents an average of 2-3 scans for model complexes and ~25 scans for protein samples.

4.2.4. Fitting Procedures

The intensity of pre-edge features were quantitated by fits to the data. The fitting program EDG_FIT, which utilizes the double precision version of the public domain MINPAK fitting library[46] was used. EDG_FIT was written by Dr. Graham George of the

Stanford Synchrotron Radiation Laboratory. Pre-edge features were modeled by pseudo-Voight line shapes fixed to have a 1:1 Gaussian:Lorentzian mixture. This line shape is appropriate as the experimental features are expected to be a convolution of the Lorentzian transition envelope[47] and the Gaussian lineshape imposed by the spectrometer optics.[44,48,49] The 1:1 Gaussian:Lorentzian admixture was found empirically to reproduce the spectral data. The number of functions employed to fit the rising edge background was chosen on the basis of features clearly indicated by the second derivative of the data. These rising edge functions were pseudo-Voight line shapes for which the Gaussian:Lorentzian mixture was allowed to vary to give the best empirical fit. Fits used in the calculation of pre-edge peak intensity were required to reproduce both the data and the second derivative of the data. For each spectrum, a number of fits which met these criteria were obtained. In general, fits were performed over several energy ranges: from one including only the pre-edge to one including the white line maximum of the edge. For spectra with very low-intensity pre-edge features, however, it was not always possible to extend the fitting range more than ~1 eV higher in energy than the pre-edge feature. This was because the small intensity of the fitted feature became lost in the tail of the rising edge and these fits did not produce a reasonable background for the pre-edge feature. The fit intensities are reported as the area of each pre-edge feature, calculated as the full-width-at-half-maximum (FWHM) x height of the feature. The value given is the average of all the good fits and the error is the standard deviation of the set.

4.2.5. Calculation of Covalency

The Cu-S covalency of each sample was calculated from its pre-edge intensity using equation 1.3c, rewritten for sulfur. The results of such an analysis may depend on the procedures used to fit the data and to obtain an experimental intensity, as well as the criteria used to determine a set of good fits. In Chapter 3, the S K-edge spectra of the Cu-thiolate complex, Cu-tet *b*, and Pc were fit using the program FITCUR which employed only Gaussian line shapes in the fitting procedure. The covalency in Cu-tet *b* was quantitated from an Xα calculation to be ~15% S 3p character in the HOMO. This result was then used to quantitate the covalency of Pc to be (38 ± 3)%. The present analysis using EDG_FIT (see above Section 4.2.4.) should produce more reliable fits to the spectral data because of the ability to model features using pseudo-Voight line shapes. To test the precision of the fitting procedures, EDG_FIT analysis was performed on the S K-edge spectrum of Cu-tet *b*. The intensity ratio obtained from FITCUR fitting is Cu-tet *b*:Pc = 1.17 ± 0.05 (where the error is estimated from extensive FITCUR fitting of

similar spectra to be maximally ~3%). The intensity ratio obtained from EDG_FIT fits is Cu-tet *b*:Pc = 1.01 ± 0.01. If the fitted intensities from the EDG_FIT analysis are quantitated using the Xα calculated HOMO covalency of Cu-tet *b*, the covalency for the Pc HOMO is found to be ~(44 ± 2)% S(Cys) 3p character. This is in reasonable agreement with the results obtained using FITCUR (see Chapter 3). Thus, the value obtained for the covalency of a sample may vary by up to ~10% based on the procedures used to quantitate experimental intensity. However, as long as the covalencies are determined using the same fitting program and criteria, the only error which need be considered is that introduced by the given fitting method employed (see Section 4.2.6).

In order that the results from the analysis presented herein be easily comparable to and consistent with previous work, the covalency in the HOMO of Pc is scaled to 38% S(Cys) 3p character, *i.e.*, as determined by previous studies (see Chapter 3).

4.2.6. Error Analysis

There are several possible sources of systematic error in the analysis of these spectra. Normalization procedures can introduce a 1-3% difference in pre-edge peak heights, as determined by varying the parameters used to normalize a set of ligand K-edge spectra such that the final fits met requirements of consistency. This maximum of ~3% error and the error resulting from the fitting procedure discussed above (Section 4.2.4) were taken into account in the calculation of pre-edge intensities and subsequent determinations of covalency.

4.2.7. Analysis of Copper Content in M121Q Azurin

Protein and Cu analyses were conducted on M121Q azurin to determine the percentage of the M121Q azurin active sites occupied by copper, as zinc-containing sites are also generated during its preparation.[22]

Protein content was assayed according to the method of Goa.[50] An aliquot of protein was denatured using NaOH. Exposed amino acid nitrogens form a complex with Cu(II) upon addition of Benedict's reagent. The absorption of this complex at 330 nm was monitored and comparison to a standard curve allowed for the determination of protein concentration.

Cu content was first assayed chemically.[51] L-cysteine was added to an aliquot of the protein solution to reduce Cu(II) to Cu(I). Addition of 2,2'-biquinoline (in acetic acid) formed a complex with an absorption band at 546 nm. Comparison of the

absorption of the complex to a standard curve allowed the Cu concentration to be determined. Cu content was also determined by atomic absorption spectroscopy.

4.3. Results of X-ray Absorption Experiments

The S K-edge spectra of the classic blue copper proteins Pc, *Pa*WT azurin, and *Ad*WT azurin are shown in Figure 4.2. Each spectrum exhibits a well-resolved pre-edge feature at 2469.0 eV. Each spectrum has been normalized to an edge jump of one sulfur. Pc has a total of three sulfur-containing residues. *Pa*WT and *Ad*WT each have a total of nine sulfur-containing residues. In each system, only the cysteine sulfur ligand has overlap with the Cu $3d_{x^2-y^2}$ orbital and contributes to pre-edge intensity.[52] Thus, to compare intensities, each pre-edge must be re-normalized to account for the non-contributing sulfurs in the sample, *i.e.*, for Pc, this requires re-normalization by a factor of three. Figure 4.2, inset, shows the re-normalized pre-edge features for Pc, *Pa*WT azurin, and *Ad*WT azurin. The re-normalized intensity of these pre-edge features is similar for all three samples.

Table 4.4 summarizes the energies and intensities (both normalized and re-normalized) for each pre-edge feature in this study. The Table also provides references for the amino acid sequences which were used to determine the re-normalization factors of each sample.

The S K-edge spectra for the Cu-thiolate model complexes Cu-tet *b* and LCu($SCPh_3$) [L=(HB(3,5-*i*-$Pr_2pz)_3$)] are shown in Figure 4.3. The S K-edge of Cu-tet *b* exhibits a well-resolved pre-edge at 2470.3 eV, while that of the LCu($SCPh_3$) exhibits a pre-edge feature at 2468.8 eV with much greater intensity. Because each of these model compounds contains only one sulfur (which contributes to both the pre-edge and the edge jump), the observed intensities may be compared directly.

Figure 4.4 shows the S K-edge spectra for the H117G(Cu), H117G(Hista) and H117G(Im) mutants of *P.a.* azurin. Each spectrum exhibits a pre-edge feature: those of H117G(Cu) and H117G(Im) are at 2469.1 and 2469.0 eV, respectively, while that of H117G(Hista) appears at 2469.6 eV. The pre-edge intensity in these samples has been re-normalized by a factor of nine. The re-normalized pre-edge intensity (Figure 4.4, inset) varies in the order H117G(Cu) < H117G(Hista) < H117G(Im). Further, the H117G(Im) pre-edge intensity is less than that observed for the *Pa*WT sample (Figure 4.2) from which these mutants originate.

The S K-edge spectra of Stella(LO), Stella(HI), and M121Q are shown in Figure 4.5. Each spectrum exhibits a pre-edge feature at 2469.1 eV. The Stella samples

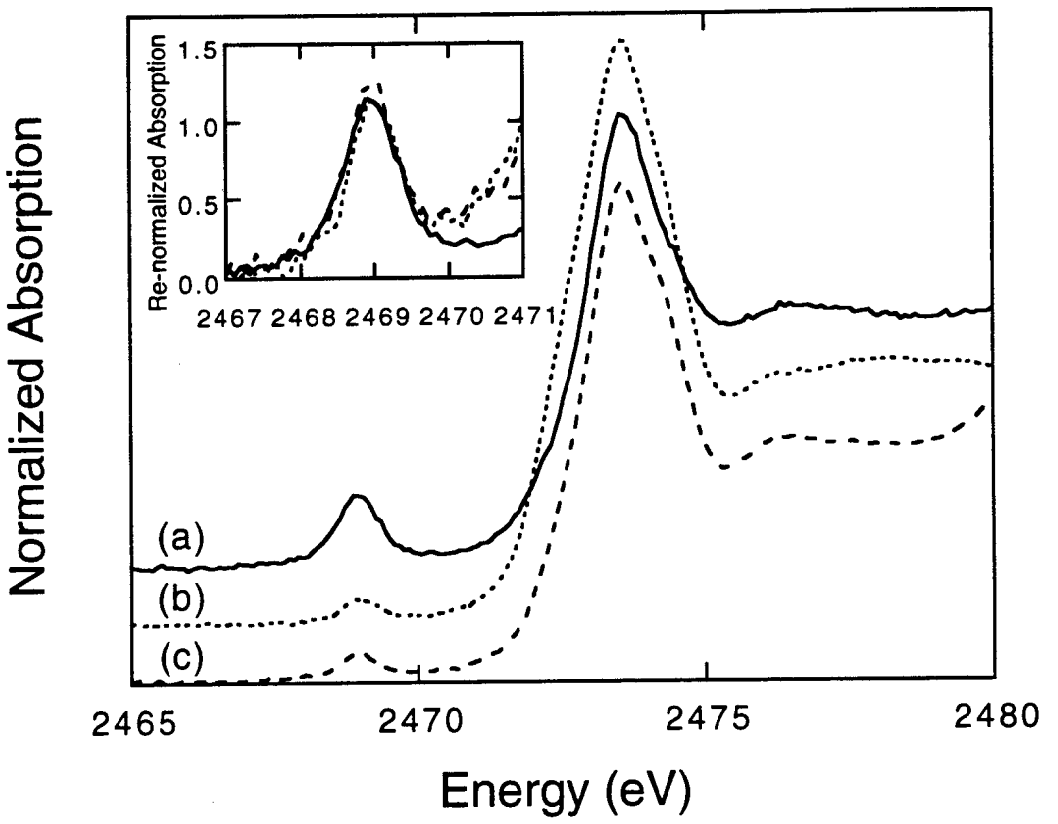

Figure 4.2. S K-edge X-ray absorption spectrum of (a) Pc [—] (b) *Pa*WT [·····] and (c) *Ad*WT [----]. Each spectrum exhibits a single pre-edge feature well separated from the rising edge. Inset shows the pre-edge transition intensity re-normalized to show only the contribution from the S(Cys) residue bound to Cu (see text).

Table 4.4. S K-edge Pre-edge Energies and Intensities for Blue Copper Sites and Cu-thiolate Model Complexes

Sample	Pre-edge Energy (eV)	Normalized Intensity[a]	Re-normalization Factor[b]	Ref.	Re-normalized Intensity
Pc	2469.0	0.341 ± 0.011	3	*d*	1.022 ± 0.032
*Pa*WT	2469.0	0.113 ± 0.004	9	*e*	1.014 ± 0.038
*Ad*WT	2469.0	0.101 ± 0.004	9	*f*	0.907 ± 0.033
Cu-tet *b*	2470.3	0.346 ± 0.010	1		0.346 ± 0.010
LCu($SCPh_3$)	2468.8	1.483 ± 0.051	1		1.483 ± 0.051
H117G(Cu)	2469.1	0.028 ± 0.002	9	*e*	0.255 ± 0.020
H117G(Hista)	2469.6	0.043 ± 0.003	9	*e*	0.383 ± 0.025
H117G(Im)	2469.0	0.072 ± 0.008	9	*e*	0.648 ± 0.068
Stella(LO)	2469.1	0.217 ± 0.009	3	*g*	0.652 ± 0.026
Stella(HI)	2469.1	0.189 ± 0.006	3	*g*	0.568 ± 0.020
M121Q	2469.1	0.016 ± 0.001	8 x 1.67[c]	*c*	0.217 ± 0.017
NiR	2469.0	0.105 ± 0.004	10	*h*	1.053 ± 0.038
H35Q	2469.0	0.093 ± 0.005	9	*h*	0.836 ± 0.047

[a] Determined from fits to the data. See Experimental (Section 4.2.4 and 4.2.6) for a discussion of fitting procedures and error determination

[b] For comparison, pre-edge intensities must be re-normalized to account for the sulfur-residues in the sample which do not contribute to pre-edge intensity (See text, Section 4.3). References given in this table are for the amino acid sequence or crystal structure for each protein which was used to determine the number of total sulfur containing residues in the sample.

[c] The M121Q is re-normalized by an additional factor to account for the fact that the sample contained ~40% Zn M121Q azurin (see text, Section 4.3)

[d] Boulter, D.; Haslett, B. G.; Peacock, D.; Ramshaw, J. A. M.; Scawen, M. D. In *International Review of Biochemistry*; Northcote, D. H., Ed.; University Park Press: Baltimore, 1977; Vol. 13; pp 1-40.

[e] Adman, E. T.; Jensen, L. H. *Israel. J. Chem.* **1981**, *21*, 8-12.

[f] Norris, G. E.; Anderson, B. F.; Baker, E. N. *J. Mol. Biol.* **1983**, *165*, 501-521.

[g] Bergman, C.; Gandvik, E.-K.; Nyman, P. O.; Strid, L. *Biochem. Biophys. Res. Commun.* **1977**, *77*, 1052-1059.

[h] Fenderson, F. F.; Kumar, S.; Adman, E. T.; Liu, M.-Y.; Payne, W. J.; LeGall, J. *Biochemistry* **1991**, *30*, 7180-7185.

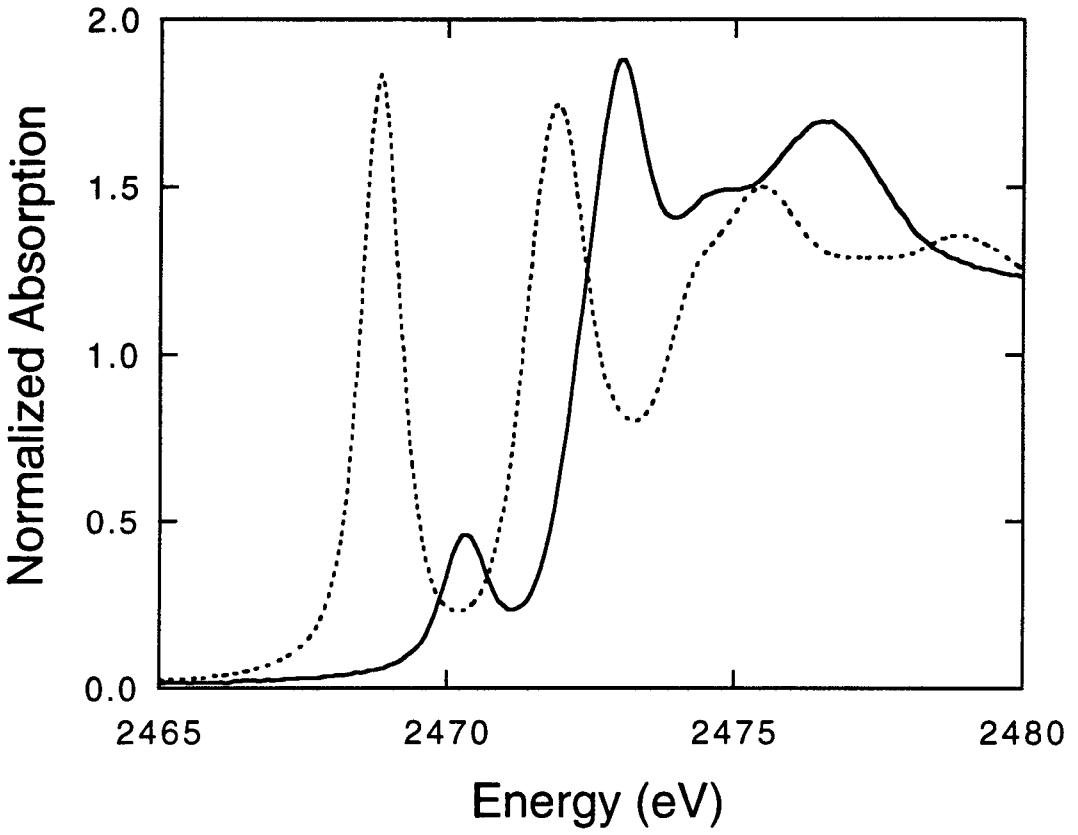

Figure 4.3. S K-edge X-ray absorption spectrum of Cu-tet *b* [—] and LCu($SCPh_3$) [·····]. Each spectrum exhibits a single pre-edge feature well separated from the rising edge. The intensity of the pre-edge in LCu($SCPh_3$) is significantly higher and the feature is at lower energy than in Cu-tet *b*.

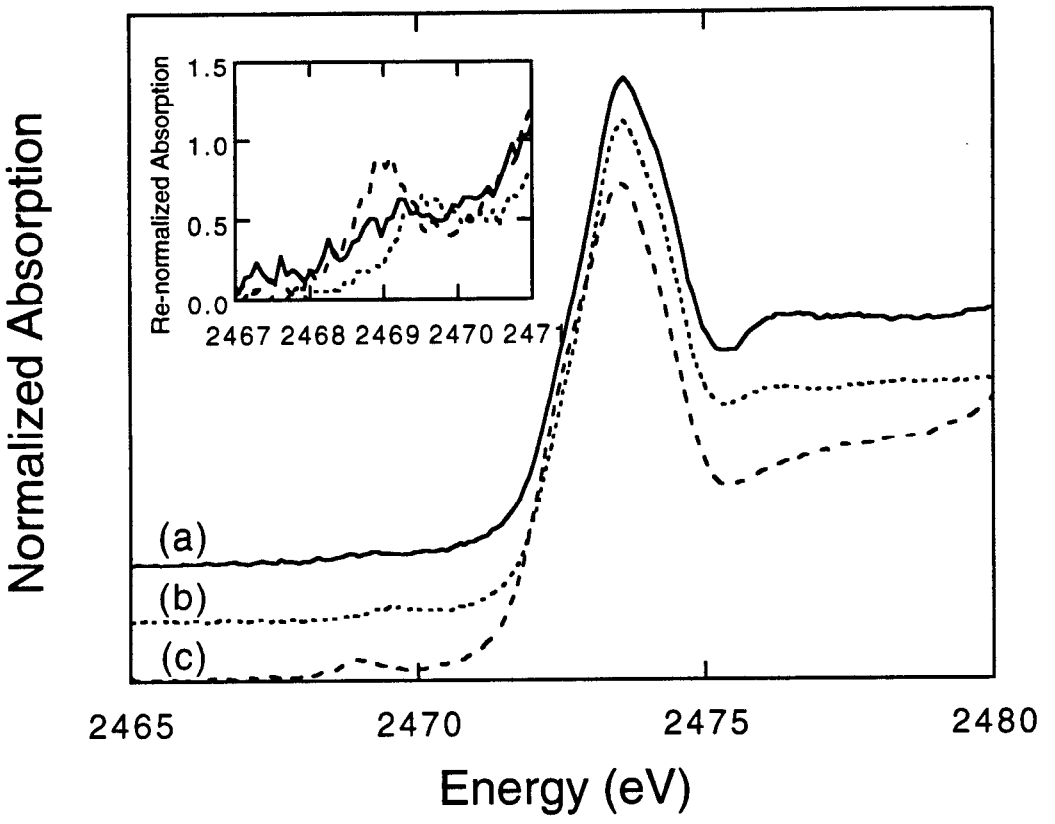

Figure 4.4. S K-edge X-ray absorption spectrum of (a) H117G(Cu) [—] (b) H117G(Hista) [·····] and (c) H117G(Im) [----] azurin. Each spectrum exhibits a single pre-edge feature well separated from the rising edge. Inset shows the pre-edge transition intensity re-normalized to show only the contribution from the S(Cys) residue bound to Cu (see text).

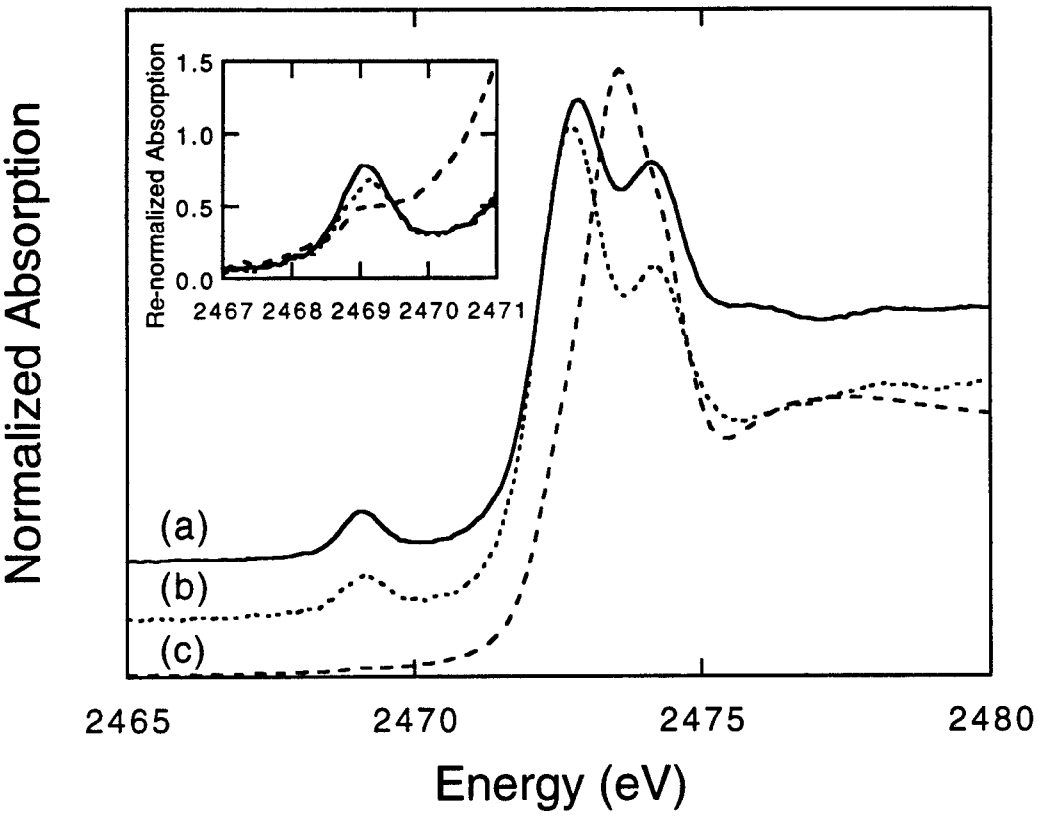

Figure 4.5. S K-edge X-ray absorption spectrum of (a) low pH Stellacyanin [—] (b) high pH Stellacyanin [·····] and (c) M121Q azurin [----]. Each spectrum exhibits a single pre-edge feature well separated from the rising edge. Inset shows the pre-edge transition intensity re-normalized to show only the contribution from the S(Cys) residue bound to Cu (see text).

have been re-normalized by a factor of three. The M121Q data is re-normalized by a factor of eight for the non-contributing sulfur containing residues, as well as by a factor of 1.67 because only ~60% of the sample contains Cu in the active site. (The remaining sample consists of Zn-containing active sites; S(Cys) bound to Zn will exhibit no pre-edge feature, but will contribute to the edge jump). The re-normalized intensity (Figure 4.5, inset) is less for Stella(HI) than for Stella(LO); both are significantly more intense than that in M121Q azurin, which is quite weak in comparison to other blue copper pre-edge features. Stella exhibits a different white line pattern than all other protein samples. While all the other samples have a single maximum at ~2473.5 eV, Stella has two maxima at ~2472.8 and ~2474.3 eV.

Figure 4.6 shows the S K-edge spectra of NiR and H35Q. Each spectrum exhibits a well-resolved pre-edge feature at 2469.0 eV. The NiR spectrum is re-normalized by a factor of ten and the H35Q by a factor of nine. The NiR re-normalized pre-edge intensity is similar to that observed in the classic blue copper sites (see Figure 4.2). The H35Q re-normalized pre-edge intensity is somewhat reduced relative to the *Pa*WT protein from which it originates.

4.4. Analysis of Results

4.4.1. Pre-edge Peak Intensities: Calculation of Covalency

The HOMO covalency of the Cu-S(Cys) interaction in Pc has been quantitatively determined to be 38% S(Cys) 3p character (see Chapter 3). Using this value as a calibration of the S K-edge pre-edge intensity, the covalency can be calculated from the re-normalized experimental intensity for each complex using equation 1.3c. The S(Cys) character in the HOMO orbital of the blue copper centers and Cu-thiolate model complexes ranges from ~55% in LCu($SCPh_3$) to ~8% in M121Q azurin. These results are summarized in Table 4.5.

Covalencies are calculated for the H117G series. However, the values should be used only for qualitative comparisons. Since each of these systems exists as a mixture of blue and normal copper, the values are not quantitatively reliable.

4.4.2. Pre-edge Peak Energies

The pre-edge energy for these proteins and model complexes (see Table 4.4) ranges from 2468.8 eV in LCu($SCPh_3$) to 2470.3 eV in Cu-tet *b*. The blue copper pre-edge features fall in between, at 2469.0-2469.1 eV.

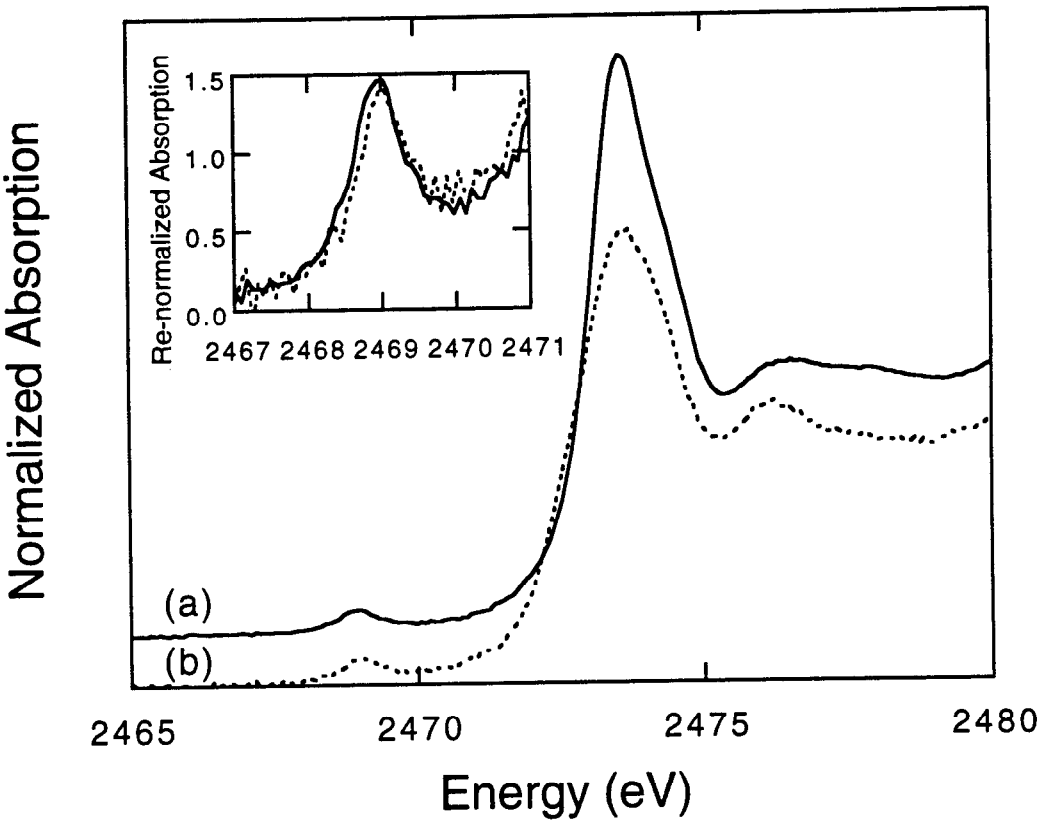

Figure 4.6. S K-edge X-ray absorption spectrum of (a) NiR [—] and (b) H35Q azurin [·····]. Each spectrum exhibits a single pre-edge feature well separated from the rising edge. Inset shows the pre-edge transition intensity re-normalized to show only the contribution from the S(Cys) residue bound to Cu (see text).

Table 4.5. Summary of Covalencies of Cu-thiolate Bonds in Blue Copper Sites and Model Compounds

Sample	% thiolate character in HOMO	Standard Deviation
Pc	**38.0**[a]	±1.2
*Pa*WT	37.7	±1.4
*Ad*WT	33.7	±1.2
Cu-tet [b]	12.8	±0.4
LCu($SCPh_3$)	55.1	±1.9
H117G(Cu)	(9.5)	(±0.8)
H117G(Hista)	(14.3)	(±1.0)
H117G(Im)	(24.1)	(±2.5)
Stella(LO)	24.2	±1.0
Stella(HI)	21.1	±0.7
M121Q	8.1	±0.6
NiR	39.1	±1.4
H35Q	31.1	±1.8

[a] Bolded value indicates that other covalencies are calculated relative to this value

[b] Parentheses indicate that these samples contained mixtures of copper sites and thus these values should not be taken as quantitatively correct.

The pre-edge transition energy is determined by both the energy of the S 1s core, which is related to the relative charge on the sulfur, and the HOMO energy, which has contributions from both the ligand field of the copper and the d-manifold energy. A complete quantitative analysis of the contributions to the pre-edge transition energies, as was presented in Chapter 2 for Cu-Cl model complexes, is not possible for these protein systems. In the proteins, the rising edge is a superposition of all sulfur residues in the sample and thus does not provide information about the core 1s energy of the ligating S(Cys).

Nevertheless, there are variations in pre-edge energies which can be understood qualitatively. The consistency of the pre-edge feature energy in the blue copper centers (especially the classic sites, all of which occur at 2469.0 eV) likely reflects the highly conserved ligand set and geometry, as well as a relatively consistent Cu-S(Cys) bonding interaction (resulting in a similar degree of charge donation from the S(Cys) to the copper and thus a similar S(Cys) 1s core energy in each site).

For centers in which the Cu-S(Cys) covalency is reduced relative to the classic sites (e.g., in Stella and H117G azurin), one can expect the S(Cys) 1s core to be at less deep binding energy because less charge will have been donated to the Cu. If the HOMO energy were not shifted, this would result in a pre-edge transition at lower energy. However, the pre-edge energy in these sites is higher than that in the classic blue sites, indicating that the HOMO has shifted up in energy in these systems. The sources of these energetic variations will be discussed in greater detail for each sample in the next section.

4.4.3. Correlations in Cu-S(Cys) Bonding

4.4.3.1. Classic Blue Copper Covalency. The Cu-S(Cys) covalency in Pc, *Pa*WT and *Ad*WT is (38.0±1.2)%, (37.7±1.4)% and (33.7±1.2)% S(Cys) 3p character in the HOMO, respectively. These results demonstrate the conservation of highly covalent Cu-S(Cys) interactions in these sites and underscore the importance of the Cu-S(Cys) bond for the determination of the electronic structure in blue copper proteins *(vide infra)*. The small decrease in covalency in *Ad*WT may be a reflection of a somewhat weaker Cu-S(Cys) bond. However, the bond length in *Ad*WT is similar to the other proteins and neither the rR Cu-S(Cys) stretching frequency nor the 600 nm absorption intensity indicate a weaker Cu-S(Cys) interaction.

4.4.3.2. Blue *vs.* Normal Copper Covalency: Model Complexes. The difference in covalency between the LCu($SCPh_3$) and Cu-tet *b* model complexes serves to define the difference in the electronic structure between blue Cu-cysteine and normal

Cu-thiolate interactions. The calculated covalency in $LCu(SCPh_3)$ is (55.1±1.9)% S 3p in the HOMO, while that in Cu-tet *b* is (12.8±0.4)%.

The increased coordination in Cu-tet *b* is accompanied by a longer, weaker, and thus less covalent, Cu-S bond than observed in blue copper centers. The S(thiolate) 1s core energy is likely at less deep binding energy in Cu-tet *b* because less charge would be donated to the Cu through this weaker interaction. If the HOMO energies were the same, this would result in a pre-edge transition at lower energy. Experimentally, however, the Cu-tet *b* transition occurs at much higher energy (~1.3 eV higher in energy than the classic blue copper sites), indicating the HOMO is shifted to higher energy in Cu-tet *b*. This is likely related to the increased coordination number in Cu-tet *b*, which would increase the energy of the d-manifold in the complex.

The $LCu(SCPh_3)$ Cu-thiolate covalency is very high, underscoring the necessity of a strong Cu-S bond for the unique spectral features of blue copper sites. The very high covalency of $LCu(SCPh_3)$ relative to the protein sites may have to do with nature of the thiolate. One might expect $-SCPh_3$ to be more electron donating than cysteine ($-SCH_2CH(NH_3^+)(COO^-)$).[53] Increased electron donating capability would allow for a stronger Cu-S(thiolate) interaction in $LCu(SCPh_3)$.

The high covalency of $LCu(SCPh_3)$ would indicate that the sulfur is an effective donor of charge to the copper, shifting its core to deeper binding energy relative to the classic blue sites. If the HOMO energies were the same, the pre-edge transition would appear at higher energy in $LCu(SCPh_3)$. The lower energy (2468.8 eV) of the pre-edge of $LCu(SCPh_3)$ then likely reflects a shift in the HOMO to deeper binding energy. Since the ligand field should be similar to blue copper proteins, this would indicate that the d-manifold is shifted to lower energy in the complex.

4.4.3.3. Blue *vs.* Normal Copper Covalency: Proteins. While the covalency of the H117G azurin mutants can not be compared quantitatively, the relative values of the intensities do reflect a trend in covalency in blue as compared to normal copper centers. In H117G(Im), the mixture is comprised of mostly blue copper centers and the total pre-edge intensity is higher, reflecting the higher covalency in blue relative to normal copper sites. Likewise, each mixture in both H117G(H_2O) and H117G(Hista) is comprised of mostly normal copper centers and the lower total pre-edge intensity reflects the decreased covalency in these sites.

The replacement of His117 with $(H_2O)_2$ or the bidentate histamine ligand results in a less covalent Cu-S(Cys) interaction than in the WT azurin. This indicates that the strong C_{3v} site symmetry (3 strong equatorial ligands) is a requirement for the blue

copper site. This coordination, which is restored upon the addition of imidazole, allows for a strong Cu-S(Cys) interaction which then dominates the electronic structure.

Like the pre-edge intensities, the pre-edge energies of the H117G sites reflect the contributions of a mixture of blue and normal copper, but the dominant species in each sample will be the primary determinant of pre-edge energy. In H117G(Cu) and H117G(Hista) the covalency of the dominant normal copper component is decreased and thus one would expect the S(Cys) 1s core energy to be at less deep binding energy (which would result in a pre-edge at lower energy if the HOMO were at the same energy as in the classic blue copper sites. Since the pre-edge energies of these samples is, however, higher than in classic blue copper, this would indicate that the HOMO in these sites is shifted to higher energy. This is consistent with the picture of these normal copper sites having an expanded coordination sphere in which two waters or a bidentate histamine is bound. The H117G(Hista) is, in fact, at significantly higher energy (2469.6 eV) which would indicate that the histamine provides a stronger ligand field than the bound waters, resulting in a larger repulsive interaction with the HOMO. The H117G(Im) pre-edge feature appears at 2469.0 eV, the same energy as the classic blue copper sites, providing further evidence that the binding of imidazole at the copper regenerates the electronic structure characteristic of blue copper sites.

4.4.3.4. Perturbed Blue Copper Centers: Stellacyanin and M121Q. The Cu-S(Cys) covalency in Stella(LO) is decreased (to (24.2±1.0%)) relative to the classic blue copper sites. It is proposed that the axial S(Met) found in the classic blue sites is replaced in Stella by an O(Glutamine).[18-20] The observed decrease in covalency would be consistent with this change in coordination. The putative axial O(Glutamine) would be stronger than the S(Met) in the other systems and would result in a weaker Cu-S(Cys) interaction. Specifically, a stronger axial ligand might cause a rotation in the half-occupied HOMO resulting in a decrease in overlap between the Cu and the S(Cys). Such a rotation has been suggested as an explanation for the rhombic EPR signal of Stella.[11] Decreased covalency is consistent with other spectroscopic differences observed in Stella. The rR Cu-S(Cys) stretching frequency indicates a somewhat weaker bond. Decrease in the intensity of the S(Cys)π —> Cu CT transition (~600 nm) might also suggest a weakening of the Cu-S(Cys) interaction. However, while the S(Cys)p_π —> Cu CT transition (~600 nm) intensity clearly decreases, the absorption intensity at ~450 nm increases. Based on the assignment of the ~450 nm intensity as a S(Cys) pseudo-σ —> Cu CT transition, the optical spectrum would indicate that while the π-interaction decreases, the σ-interaction increases. The S K-edge pre-edge intensity will reflect the sum of both σ- and π-bonding S(Cys) 3p orbital character in the HOMO.

Thus, based on this assignment of the optical spectrum, the increase in σ-bonding must be less than the decrease in π-bonding for the pre-edge intensity to indicate a net decrease in Cu-S(Cys) covalency. An alternative explanation may be that the increase in intensity ~450 nm is due to a N(His) —> Cu CT transition and that the optical spectrum and S K-edge pre-edge intensity reflect only a decrease in S(Cys) p_π-interaction.

Upon conversion of Stella to the high pH form, the covalency of the Cu-S(Cys) interaction is further reduced (to (21.1±0.7%)). This is consistent with the picture of the Stella active site which has emerged from pulsed ENDOR studies.[21] The putative axial ligand at higher pH is an amide nitrogen which is an even stronger axial ligand than the O(Glutamine) proposed at low pH. This would cause a further decrease in the strength of the Cu-S(Cys) interaction.

Because the Cu-S(Cys) interaction is weaker in Stella than in the classic blue sites, one would expect the S(Cys) to donate less total charge to Cu in Stella, resulting in a S(Cys) 1s core at higher energy. If the HOMO energies were the same, the Stella pre-edge would occur at lower energy than in the classic blue copper sites. Since the pre-edge energy in both low and high pH Stella appears at slightly higher energy than that in the classic blue sites, this must reflect an increased repulsion of the HOMO in Stella, due perhaps to the increased LF strength of the ligand donor set in Stella.

Finally, Stella has a split white line pattern different from all the other protein systems in this study. This pattern, which is also seen in the S K-edge of free cystine (data not shown), is indicative of the disulfide linkage in the protein backbone (not involved in bonding at the active site) of Stella. Stella is the only protein in this study with a disulfide moiety.

The calculated covalency in M121Q azurin is significantly lower than that in all other blue copper centers studied. The fact that other spectroscopies indicate that M121Q and Stella are very similar called into question the reliability of the S K-edge XAS data. There are two possible sources of anomolously low intensities in the S K-edge pre-edge feature. First, it is possible that more of the active sites are apo or Zn-containing than was originally thought (this would result in S(Cys) at these sites which contribute to the edge jump, but not to the pre-edge). Second, it is possible that the sample contains excess sulfur of some kind. To test the first possibility, Cu analysis was performed to determine the percentage of active sites occupied by copper. Table 4.6 shows the results of protein and copper analyses. These experiments indicate the sample contains ~50% Cu. While, this would increase the calculated covalency slightly (to ~10%) relative to that based on a ~60% Cu occupancy, the covalency of the site is still much lower than other blue copper sites, including Stella.

Table 4.6. Copper Content Analysis of M121Q Azurin

Aliquot	Protein[§] Conc. (μM)	Cu Conc. from Atomic Absorption (μM)	% Cu	Cu Conc. from Biquinoline Assay (μM)	% Cu
1	408	230	56	222	54
2	654	340	52	334	51
3	908	350	39	373	41
4	817	327	40	357	44
			47 (avg)		48 (avg)

§ Determined by biuret analysis.

The possibility of the sample containing excess sulfur must also be considered. The sample was remetallated with copper sulfate. It is, however, unlikely there is excess sulfate in the sample, as sulfate has a very intense white line at ~2483 eV and even small amounts of sulfate in the sample would contaminate the spectrum at this energy. No such contamination is evident. The other possible source of excess sulfur is the presence of "junk" protein. The M121Q sample was prepared originally for Cu spectroscopy and great care was taken to ensure there was no adventitious Cu. However, purification to remove excess sulfur-containing protein was not undertaken. This would seem the most reasonable explanation for the anomolously low results. If some of the protein content which was quantitated (see Table 4.6) was actually "junk", then the Cu content of actual M121Q sites would be different than the ~50% determined. There is, unfortunately, no way to know for certain. For reliable results, the sample would need to be more carefully prepared and the S K-edge remeasured.

While the M121Q S K-edge data can not be used to determine quantitative covalency of the site, the energy of the pre-edge transition at 2469.1 eV is reliable. This pre-edge energy is the same as that observed in stellacyanin. M121Q azurin is known to have a stronger axial ligand interaction than the *Ad*WT azurin from which it originates (see Table 4.1). Thus, the higher energy of the pre-edge feature in M121Q is likely related to the increased strength of the ligand field in the mutant active site. This is the same explanation proposed for the Stella pre-edge energy assuming an axial glutamine at the site. The similarity in pre-edge energy position, combined with the nearly identical spectroscopic features of M121Q and Stella support the use of M121Q as a structural model for Stella.

4.4.3.5. Perturbed Blue Copper Centers: Nitrite Reductase. The HOMO covalency obtained for NiR (39.1±1.4)% is very similar to that of the classic blue proteins. The differences in the absorption spectrum of NiR, however, clearly indicate that the electronic structure is different. As in Stella, the intensity of the S(Cys)p_π —> Cu CT transition (~600 nm) decreases, while the intensity of the ~450 nm band increases relative to the classic blue copper sites. In NiR, however, the change is even more dramatic. And, unlike in Stella, the total covalency of the Cu-S(Cys) bond is apparently not decreased in NiR.

The decrease in the intensity of the S(Cys)p_π —> Cu CT transition indicates a decrease in the S(Cys)p_π interaction in NiR relative to the classic blue sites. Since the S K-edge pre-edge intensity will reflect the sum of both σ- and π-bonding S(Cys) 3p orbital character in the HOMO, an increase in Cu-S(Cys) σ-bonding in NiR must accompany the decrease in π-bonding interaction such that the total covalency remains

about the same as in the classic blue copper sites. This increase in σ-bonding interaction would be consistent with an assignment of the ~450 nm intensity in NiR as a S(Cys) pseudo-σ —> Cu CT transition. Note that the rR Cu-S(Cys) stretch of NiR indicates a weaker Cu-S(Cys) bond and the crystal structure reflects a slightly longer Cu-S(Cys) bond (see Table 4.1) than for the classic sites.

An alternative explanation for the NiR S K-edge spectrum is that the observed pre-edge intensity reflects both S(Cys) and S(Met) contributions. The S(Met) may have some overlap with the HOMO in NiR. This would mean that the ~39% covalency reflects the total covalency in the HOMO of both ligating sulfurs. Xα calculations of this site will help to determine if overlap between the S(Met) and the half-occupied HOMO is possible.

4.4.3.6. Mutations Away From the Blue Copper Site. The observed covalency in H35Q azurin is slightly decreased relative to the *Pa*WT from which it comes. Despite the fact than in H35Q no mutations have been made to the immediate ligation of the Cu, the electronic structure of the site has been effected. This demonstrates that non-ligating residues in the protein backbone can influence the electronic structure of the active site.

4.5. Discussion

Sulfur K-edge XAS has been used to probe the Cu-thiolate covalency in a number of model complexes and blue copper proteins. The application of this technique has allowed the observation of some important trends in the covalency of these sites.

Classic blue copper sites such as Pc and azurin are characterized by a highly covalent Cu-S(Cys) bonding interaction. This property dominates many of the spectral features and much of the electronic structure of these sites.

Model complexes which contrast blue and normal copper further support that a highly covalent S(thiolate) interaction is necessary for the properties of a blue site as demonstrated by the $LCu(SCPh_3)$ complex. The spectral properties of a normal copper are observed in the Cu-tet *b* complex which exhibits much lower S(thiolate)-Cu covalency. The covalency also appears to be dependent on the nature of the thiolate in the complex, as $LCu(SCPh_3)$ is even more covalent than the blue copper protein centers. This theory can be tested by measurement of the S K-edge spectrum for the analogous model $LCu(SC_6F_5)$,[36] which also displays spectral features consistent with blue copper. However, the thiolate has been shown to be much more electron withdrawing in $LCu(SC_6F_5)$ than in the complex included in this study.[54]

For centers in which the C_{3v} effective symmetry of the blue copper active site is destroyed, such as H117G(Cu) or H117G(Hista), the spectral properties indicate a normal copper site and the S K-edge XAS reflect a significantly decreased Cu-S(Cys) covalency. The addition of imidazole to H117G reconstitutes the C_{3v} geometry and restores the blue copper electronic structure. Thus, the strong equatorial ligands in the blue copper site are necessary for the highly covalent Cu-S(Cys) bond and the resulting electronic structure of the blue copper site.

Decreased HOMO covalency, relative to Pc and azurin, is observed in the perturbed blue copper protein Stella. This is consistent with the suggestion that Stella has a stronger axial ligand (O(Glutamine)) than the classic blue sites, which may result in a rotation of the HOMO and less Cu-S(Cys) overlap. A further decrease in covalency is observed in the high pH form of the protein, which is consistent with the interpretation of pulsed ENDOR results on this site which suggest an amide nitrogen of glutamine acts as the axial ligand at high pH.[21] The S K-edge spectra reflect a decrease in total HOMO covalency but can not differentiate between a moderate decrease in Sp_π interactions and a larger decrease in Sp_π, accompanied by an increase in Sp_σ interactions. MCD and optical spectra, however, do reflect individual contributions from σ- and π- bonding interactions. Detailed SCF-Xα-SW calculations on M121Q, which serves as a structural model for the Stella site, are in progress. Combined with the interpretation of the MCD spectrum of stellacyanin, the Xα results should serve to define the electronic structural changes in Stella and to further correlate these changes with the variations seen in both the EPR and the optical absorption of this protein.

NiR exhibits total HOMO covalency which is similar to that observed in the classic blue copper centers. Variations observed in the optical spectrum, however, suggest that the covalency in NiR may be distributed differently. Specifically, a decrease in Cu-S(Cys) π-bonding is likely to be accompanied by an increase in Cu-S(Cys) σ-bonding such that the total covalency, as reflected in the S K-edge pre-edge intensity, remains about the same as in the classic blue copper sites. Distributions of this kind can not be determined from the S K-edge XAS. As for stellacyanin, Xα calculations in progress, in combination with MCD spectroscopy will help to differentiate σ- and π-interactions and to elucidate the sources of the electronic structural variations. These calculations will also define the possibility that the pre-edge intensity reflects S(Met) character in the NiR HOMO.

The source of increased intensity at ~450 nm may be different for NiR and Stella. The S K-edge XAS results, in combination with results from other techniques on these

perturbed sites, will address this possibility and provide insight into the source of the changes in absorption intensity at ~450 nm in these centers.

Finally, the S K-edge of H35Q provides evidence that a mutation away from the active site can have an effect upon the Cu-S(Cys) covalency at the active site of a blue copper protein. This result by itself does not allow conclusions to be drawn about the significance of such a change. It would perhaps be interesting to examine a number of similarly mutated sites and compare Cu-S(Cys) covalency to reduction potentials and electron transfer rates.

4.6. Acknowledgments

This research was supported by grants from NSF (CHE-9217628, E.I.S.) (CHE91-21576, K.O.H.), and NIH (RR-01209, K.O.H.). SSRL operations are funded by the Department of Energy, Office of Basic Energy Sciences. The Biotechnology Program is supported by the NIH, Biomedical Research Technology Program, National Center for Research Resources. Further support is provided by the Department of Energy, Office of Health and Environmental Research. We also thank Prof. Gerard Canters for providing the azurin and azurin mutant samples and Prof. Bruce Averill for providing the NiR sample for this study, as well as Dr. Michael Lowery for the preparation of stellacyanin. Acknowledgment is also extended to Mr. Lou LaCroix for many helpful discussions about the interpretation of these data.

4.7. References and Notes

(1) Gewirth, A. A.; Solomon, E. I. *J. Am. Chem. Soc.* **1988**, *110*, 3811-3819.

(2) Penfield, K. W.; Gewirth, A. A.; Solomon, E. I. *J. Am. Chem. Soc.* **1985**, *107*, 4519-4529.

(3) Blair, D. F.; Campbell, G. W.; Schoonover, J. R.; Chan, S. I.; Gray, H. B.; Malmström, B. G.; Pecht, I.; Swanson, B. I.; Woodruff, W. H.; Cho, W. K.; English, A. M.; Fry, H. A.; Lum, V.; Norton, K. A. *J. Am. Chem. Soc.* **1985**, *107*, 5755-5766.

(4) Nestor, L.; Larrabee, J. A.; Woolery, G.; Reinhammar, B.; Spiro, T. G. *Biochemistry* **1984**, *23*, 1084-1093.

(5) Solomon, E. I.; Baldwin, M. J.; Lowery, M. D. *Chem. Rev.* **1992**, *92*, 521-542.

(6) Adman, E. In *Advances in Protein Chemistry, Metalloproteins: Structural Aspects*; Anfinsen, C. B.; Edsall, J. T.; Richards, F. M.; Eisenberg, D. S., Ed.; Academic Press, Inc.: San Diego, 1991; Vol. 42; pp 145-198.

(7) Reinhammar, B. R. M. *Biochem. Biophys. Acta* **1972**, *275*, 245-259.

(8) Solomon, E. I.; Hare, J. W.; Dooley, D. M.; Dawson, J. H.; Stephens, P. J.; Gray, H. B. *J. Am. Chem. Soc.* **1980**, *102*, 168-178.

(9) The primary S σ-bonding interaction is thiolate based. Thus, the orbital which is involved in a σ-type bonding interaction with the Cu is referred to as pseudo-σ.

(10) Han, J.; Loehr, T. M.; Lu, Y.; Valentine, J. S.; Averill, B. A.; Sanders-Loehr, J. *J. Am. Chem. Soc.* **1993**, *115*, 4256-4263.

(11) Gewirth, A. A.; Cohen, S. L.; Schugar, H. L.; Solomon, E. I. *Inorg. Chem.* **1987**, *26*, 1133-1146.

(12) Lowery, M. D.; Solomon, E. I. *Inorg. Chim. Acta* **1992**, *198-200*, 233-243.

(13) den Blaauwen, T.; van de Kamp, M.; Canters, G. W. *J. Am. Chem. Soc.* **1991**, *113*, 5050-5052.

(14) den Blaauwen, T.; Canters, G. W. *J. Am. Chem. Soc.* **1993**, *115*, 1121-1129.

(15) The MCD spectrum of H117G(Im) shows some evidence that the sample contains a small amount of T2 copper. Lou LaCroix, personal communication.

(16) den Blaawen, T.; Hoitink, C. W. G.; Canters, G. W.; Han, J.; Loehr, T. M.; Sanders-Loehr, J. *Biochemistry* **1993**, *32*, 12455-12464.

(17) Peisach, J.; Levine, W. G.; Blumberg, W. E. *J. Biol. Chem.* **1967**, *242*, 2847-2858.

(18) Murata, M.; Beggs, G. S.; Lambrou, F.; Leslie, B.; Simpson, R. J.; Freeman, H. C.; Morgan, F. J. *Proc. Natl. Acad. Sci. (USA)* **1982**, *79*, 6434-6437.

(19) Guss, J. M.; Merritt, E. A.; Phizackerlay, R. P.; Hedman, B.; Murata, M.; Hodgson, K. O.; Freeman, H. C. *Science* **1988**, *241*, 806-811.

(20) Fields, B. A.; Guss, J. M.; Freeman, H. C. *J. Mol. Biol.* **1991**, *222*, 1053-1065.

(21) Thomann, H.; Bernardo, M.; Baldwin, M.; Lowery, M. D.; Solomon, E. I. *J. Am. Chem. Soc.* **1991**, *113*, 5911-5913.

(22) Romero, A.; Hoitink, C. W. G.; Nar, H.; Huber, R.; Messerschmidt, A.; Canters, G. W. *J. Mol. Biol.* **1993**, *229*, 1007-1021.

(23) The Cu MCD spectrum of the identical M121Q azurin sample is nearly superimposable on that of stellacyanin. Lou LaCroix, personal communication.

(24) Payne, W. In *Denitrification in the Nitrogen Cycle*; Golterman, H. L., Ed.; Plenum: New York, 1985; pp 47-65.

(25) Godden, J. W.; Turley, S.; Teller, D. C.; Adman, E. T.; Liu, M. Y.; Payne, W. J.; Legall, J. *Science* **1991**, *253*, 438-442.

(26) Hulse, C. L.; Tiedje, J. M.; Averill, B. A. *Anal. Biochem.* **1988**, *172*, 420-426.
(27) Libby, E.; Averill, B. A. *Biochem. Biophys. Res. Commun.* **1992**, *187*, 1529-1535.
(28) Sykes, A. G. In *Long-Range Electron Transfer in Biology*; Palmer, G. A., Ed.; Springer-Verlag: Berlin, 1991; pp 175-224.
(29) Sykes, A. G. *Adv. in Inorg. Chem.* **1991**, *36*, 377-408.
(30) Farver, O.; Pecht, I. In *Copper Proteins*; Spiro, T., Ed.; John Wiley & Sons, Inc.: New York, 1981; pp 153-192.
(31) Farver, O.; Pecht, I. In *Copper Proteins and Copper Enzymes*; Lontie, R., Ed.; CRC Press: Boca Raton, FL, 1984; Vol. I; pp 184-214.
(32) Farver, O.; Shakak, Y.; Pecht, I. *Biochemistry* **1982**, *21*, 1885-1890.
(33) van de Kamp, M.; Silverstrini, M. C.; Brunori, M.; Van Beeumen, J.; Hali, F. C.; Canters, G. W. *Eur. J. Biochem.* **1990**, *194*, 109-118.
(34) Nar, H.; Messerschmidt, A.; Huber, R.; van de Kamp, M.; Canters, G. W. *J. Mol. Biol.* **1991**, *218*, 427-447.
(35) LaCroix, L. , private communication.
(36) Kitajima, N.; Fujisawa, K.; Tanaka, M.; Moro-oka, Y. *J. Am. Chem. Soc.* **1992**, *114*, 9232-9233.
(37) Kitajima, N.; Fujisawa, K.; Moro-oka, Y. *J. Am. Chem. Soc.* **1990**, *112*, 3210-3212.
(38) Hughey, J. L., IV; Fawcett, T. G.; Rudich, S. M.; Lalancette, R. A.; Potenza, J. A.; Schugar, H. J. *J. Am. Chem. Soc.* **1979**, *101*, 2616-2623.
(39) Ellefson, W. L.; Ulrich, E. A.; Krogmann, D. W. In *Methods in Enzymology*; San Pietro, A., Ed.; McGraw-Hill: New York, 1980; Vol. 69; pp 223-228.
(40) Reinhammar, B. *Biochim. Biophys. Acta* **1970**, *205*, 35-47.
(41) Canters, G. W. *FEBS Lett.* **1987**, *212*, 168-172.
(42) Hoitink, C. W. G. *Gene* **1990**, *90*, 15-20.
(43) Hedman, B.; Frank, P.; Gheller, S. F.; Roe, A. L.; Newton, W. E.; Hodgson, K. O. *J. Am. Chem. Soc.* **1988**, *110*, 3798-3805.
(44) Lytle, F. W.; Greegor, R. B.; Sandstrom, D. R.; Marques, E. C.; Wong, J.; Spiro, C. L.; Huffman, G. P.; Huggins, F. E. *Nucl. Instr. Meth.* **1984**, *226*, 542-548.
(45) Stern, E. A.; Heald, S. M. *Rev. Sci. Instrum.* **1979**, *50*, 1579-1582.
(46) Argonne National Laboratory; B. S. Garbow, K. E. Hillstrom, J. J. More.
(47) Agarwal, B. K. *X-ray Spectroscopy*; Springer-Verlag: Berlin, 1979, pp 276ff.
(48) Lytle, F. W. In *Applications of Synchrotron Radiation*; Winick, H.; Xian, D.; Ye, M. H.; Huang, T., Ed.; Gordon & Breach: New York, 1989; pp 135.
(49) Tyson, T. A.; Roe, A. L.; Frank, P.; Hodgson, K. O.; Hedman, B. *Phys. Rev. B* **1989**, *39A*, 6305-6315.

(50) Goa, J. *Scand. J. Clin. Lab. Invest.* **1957**, *5*, 218-222.

(51) Felsenfeld, G. *Arch. Biochem. Biophys.* **1960**, *87*, 247-251.

(52) See Chapter 3, Section 3.3.2.2, for a discussion of why the axial S(Met) ligand does not contribute to pre-edge intensity in the S K-edge XAS of blue copper proteins.

(53) The Hammet parameters have been measured for $-CPh_3$ (σ_m=-0.01, σ_p=0.02) and $-CH_2CH_2NH_3^+$ (σ_m=0.23, σ_p=0.17). The carbon chain of cysteine should be similar to the latter substituent.

(54) Qui, D.; Kilpatrick, L.; Kitajima, N.; Spiro, T. G. *J. Am. Chem. Soc.* **1994**, *116*, 2585-2590.

Chapter 5

Chloride K-edge X-ray Absorption Spectroscopic Studies: Ligand-Metal Covalency in Transition Metal Tetrachlorides

5.1. Introduction

Analysis of ligand K-edge X-ray absorption spectra (XAS) can provide insight into the electronic structure of an absorbing atom. This technique has been applied to study the electronic structure of inorganic Cu(II) complexes[1-3] and cupric protein active sites[2] (see Chapters 2-4). The K-edge absorption of a ligand bound to a d^9 copper ion exhibits a well-resolved pre-edge feature which is assigned as a ligand 1s —> ψ^* transition, where ψ^* is the half-filled, highest-occupied molecular orbital (HOMO) in Cu(II). As described in Chapter 1, because of the localized nature of the Cl 1s orbital, this transition can have absorption intensity only if the half-occupied HOMO contains a significant component of Cl 3p character as a result of covalency. The observed pre-edge transition intensity is simply the intensity of the pure dipole-allowed Cl 1s —> 3p transition weighted by α'^2, the covalent contribution of the ligand to the HOMO (equation 1.3c). Thus, the pre-edge intensity provides a direct probe of the ligand contribution to the HOMO due to bonding.[1] (See Chapter 1, Section 1.2.4.)

The relationship between intensity and covalency described in Chapter 1 (equation 1.3c) for ligand-Cu(II) interactions is straightforward because copper(II) is d^9 and thus has a single half-occupied HOMO (ψ^*). Here we extend the technique of ligand K-edge XAS to other metal ions. As in Cu(II) systems, the pre-edge feature in other d^n metal centers corresponds to a transition (or several transitions) from a ligand 1s orbital to unoccupied or partially-occupied antibonding orbitals with both metal d- and ligand p-character. However, in systems with more than one d-manifold electron or hole, several many-electron excited states are possible and transitions to more than one partially-occupied metal d-derived orbital are possible. Further, multiplet effects in the d^{n+1} excited state can effect the observed intensity. The analysis of pre-edge intensity for the determination of HOMO covalency requires that all contributions to the intensity be taken into account.

This study examines the Cl K-edge XAS pre-edge features for the tetrahedral metal-tetrachloride series MCl_4^{n-}, where M = Cu(II), Ni(II), Co(II), Fe(II) and Fe(III). The antibonding metal-derived orbitals in T_d metal complexes are a t_2- and an e-set. The t_2-set has both Cl $3p_\sigma$ and Cl $3p_\pi$ interactions, while the e-set will have only Cl $3p_\pi$-character. In T_d Cu(II),[4] there is a single vacancy in the t_2-set, while Ni(II) and Co(II) are characterized by two and three t_2 holes, respectively. The T_d Fe(II) center has three t_2 holes and a single hole in the e-set. In the T_d Fe(III) complex, each of the d-type orbitals is half-occupied, with three t_2 holes and two e holes. Thus, in T_d Cu(II), Ni(II)

and Co(II), pre-edge transitions will correspond only to transitions to the t_2 set of antibonding orbitals, while in Fe(II) and Fe(III) transitions to the e-set are also possible.

A methodology for interpreting pre-edge intensities and energies is developed for these d^n hole systems ($n \geq 1$). The contribution to pre-edge intensity from multiplet effects is determined, and expressions which relate experimental intensity to covalency are derived. The effect on pre-edge intensity from the mixing of excited states in ligand fields of intermediate strength is defined and the ligand-metal covalency of each T_d site is quantitatively determined from the experimental pre-edge intensity. The experimental estimates of covalency are compared to SCF-Xα-SW (Xα) calculations on each complex. Finally, analysis of the pre-edge and edge energies provides quantitative information[3] about variation in chloride charge donation as well as relative shifts in the d-manifold energy of each metal center. These results are correlated with the experimentally determined covalency in each complex.

5.2. Experimental

5.2.1. Samples and Sample Preparation

A summary of the structural parameters for each of these complexes included in this study is provided in Table 5.1. Cs_2CuCl_4 was prepared according to published methods.[5,6] The remaining compounds: $(Ph_3MeAs)_2NiCl_4$, $(Ph_3MeAs)_2CoCl_4$, $(Et_4N)_2FeCl_4$, and $(Et_4N)FeCl_4$ were prepared according to procedures described in the literature.[7] The $(Et_4N)_2FeCl_4$ sample was prepared under anaerobic conditions.

For the X-ray absorption experiments, samples were ground into a fine powder (at least several minutes of grinding with mortar and pestle). The powder was dispersed as thinly as possible (to minimize the possibility of self-absorption) on mylar tape containing an acrylic adhesive determined to be free of chlorine contaminants. This procedure has been verified to minimize self-absorption effects in the data by systematically testing progressively thinner samples until the observed intensity no longer varies with the thickness of the sample. The powder on tape was mounted across the window of an aluminum plate. The $(Et_4N)_2FeCl_4$ sample was prepared in a dry, anaerobic atmosphere. A 6.35 μm polypropylene film window protected the sample from exposure to air.

Table 5.1. Structural Parameters for ~T_d MCl_4^{n-} Complexes

MCl_4^{n-} Complex[a]	Average Bond Length (Å)	Angles (°)	Related Complex	Average Bond Length (Å)	Angles (°)
Cs_2CuCl_4[b]	2.230	100-131			
$(Ph_3MeAs)_2NiCl_4$[c]	2.269	109.1-109.4	$(Et_4N)_2NiCl_4$[d]	2.245	107-111
			$(Me_4N)_2NiCl_4$[e]	2.234	108-111
$(Ph_3MeAs)_2CoCl_4$[c]	isomorphous w/ nickel complex	-	$(Me_4N)_2CoCl_4$[e]	2.254	108-111
$(Et_4N)_2FeCl_4$	-	-	$(Me_4N)_2FeCl_4$[f]	2.293	108-114
$(Et_4N)FeCl_4$	-	-	$(Ph_4As)FeCl_4$[g]	2.182	106-115

[a] Complexes for which Cl K-edge data were measured

[b] McGinnety, J. A. *J. Am. Chem. Soc.* **1972**, *94*, 8406-8412.

[c] Pauling, P. *Inorg. Chem.* **1966**, *5*, 1498-1505.

[d] Stucky, G. D.; Folkers, J. B.; Kistenmacher, T. J. *Acta Cryst.* **1967**, *23*, 1064-1070.

[e] Wiesner, J. R.; Srivastava, R. C.; Kennard, C. H. L.; DiViara, M.; Lingafelter, E. C. *Acta Cryst.* **1967**, *23*, 565-574.

[f] Lauher, J. W.; Ibers, J. A. *Inorg. Chem.* **1975**, *14*, 348-352.

[g] Cotton, F. A.; Murillo, C. A. *Inorg. Chem.* **1975**, *14*, 2467-2469.

5.2.2. X-ray Absorption Measurements

X-ray absorption data were measured at the Stanford Synchrotron Radiation Laboratory using the 54-pole wiggler beamline 6-2 in low magnetic field mode (5 kG) with a Pt-coated focusing mirror and a Si(111) double crystal monochromator, under dedicated conditions (3.0 GeV, ~50 mA). The monochromator was detuned ~30% to eliminate higher harmonic components in the X-ray beam. Details of the optimization of this set-up for low energy studies have been described in Chapter 1 (Section 1.2.5) as well as in an earlier publication.[8]

All Cl K-edge measurements were made at room temperature. The data were collected as fluorescence excitation spectra utilizing an ionization chamber as a fluorescence detector.[9,10] Several (2-3) scans were measured for each sample. The energy was calibrated from the Cl K-edge spectra of Cs_2CuCl_4, run at intervals between the samples. The maximum of the first edge-region feature in the spectrum was assigned to 2820.20 eV. Scans ranged from 2740 to 3100 eV, with a step size of 0.08 eV in the edge region. The spectrometer resolution was ~0.5 eV.[8] Calculating and comparing first and second derivatives for model compounds measured during different experimental sessions results in a reproducibility in edge position of ~0.1 eV for these experiments.

5.2.3. Data Reduction

Data were averaged and a smooth background was removed from all spectra by fitting a polynomial to the pre-edge region and subtracting this polynomial from the entire spectrum. Normalization of the data was accomplished by fitting a flat polynomial or straight line to the post-edge region and normalizing the edge jump to 1.0 at 2840 eV.

5.2.4. Fitting Procedures

The intensity of pre-edge features were quantitated by fits to the data. The fitting program EDG_FIT, which utilizes the double precision version of the public domain MINPAK fitting library[11] was used. EDG_FIT was written by Dr. Graham N. George of the Stanford Synchrotron Radiation Laboratory. Pre-edge features were modeled by pseudo-Voigt line shapes (simple sums of Lorentzian and Gaussian functions). This line shape is appropriate as the experimental features are expected to be a convolution of the Lorentzian transition envelope[12] and the Gaussian lineshape imposed by the spectrometer

optics.[9,13,14] A fixed 1:1 ratio of Lorentzian to Gaussian contribution for the pre-edge feature successfully reproduced these spectral features.

The number of functions employed to fit the rising edge background was chosen on the basis of features clearly indicated by the second derivative of the data. These rising edge functions were pseudo-Voight line shapes for which the Gaussian:Lorentzian mixture was allowed to vary to give the best empirical fit. In all cases the minimum number of functions required to successfully reproduce the data were utilized.

Fits used in the calculation of pre-edge peak intensity were optimized to reproduce both the data and the second derivative of the data. For each spectrum, a number of fits which reproduced both the data and the second derivative of the data were obtained. Fits were performed over several energy ranges: from one which included just the tail of the rising edge, to one which included the white line maximum of the edge. The value reported for the intensity of a pre-edge feature (where peak area was approximated by the height x full-width-at-half-maximum (FWHM)) is the average of all the pseudo-Voigts which successfully fit the feature. For each sample, the standard deviation of the average of the areas was calculated to quantitate the uncertainty of the fit.

5.2.5. Determination of Rising Edge Positions

The energies reported for the rising edge position were determined from the highest energy maximum in the first derivative of the data in the rising edge region. These measurements were performed independently of the above described fitting procedures.

5.2.6. Error Analysis

There are several possible sources of systematic error in the analysis of these spectra. Normalization procedures can introduce a 1-3% difference in pre-edge peak heights, as determined by varying the parameters used to normalize a set of Cl K-edge spectra such that the final fits met requirements of consistency. This maximum of ~3% error and the error resulting from the fitting procedure discussed above were taken into account in the calculation of pre-edge intensities and subsequent determinations of covalency. Experimental self-absorption could, in principle, result in an artificially low observed intensity. However, care was taken to avoid self-absorption in these experiments (*vide supra*), and this effect is assumed to be negligible.

The uncertainty in pre-edge and edge energies is limited by the reproducibility of the edge spectra (~0.1 eV). Thus, relative energies of features are reported with an error of ± 0.1 eV. For the purposes of the energy analyses herein, no error has been assumed for the 10Dq ligand field splittings used to quantitate energy shifts of HOMO orbitals.

5.2.7. SCF-Xα-SW Calculations

The calculation of D_{2d} $CuCl_4^{2-}$ has been described previously[15] and only the most salient details of the calculation are included here. Standard SCF-Xα-SW calculations[16] on T_d $[MCl_4]^{n-}$ molecules (M = Ni(II), Co(II), Fe(II), and Fe(III)) were performed on DEC station 3100 computers with ~300 iterations required for convergence. The calculations were considered to have converged when the largest relative change in the potential between subsequent iterations was less than 10^{-3}. Bond distances were averaged from crystal structure values: Cu-Cl = 2.230,[5] Ni-Cl = 2.270 Å,[17] Co-Cl = 2.280 Å,[18] Fe(II)-Cl = 2.291 Å,[19] and Fe(III)-Cl = 2.185 Å.[20] The α values of Schwarz[21] and maximum ℓ values of 4, 3, and 2 were used for the outer sphere, the metal, and the chloride, respectively. A Watson sphere coincident with the outer sphere radius was used in calculations of these charged species. Sphere radii for divalent metal calculations were chosen to be the same as those in the D_{2d} $CuCl_4^{2-}$ calculation which were optimized to match experimental g-values[15] (M = 3.11 Bohrs, Cl = 2.49 Bohrs). The sphere radii for the Fe(III)Cl_4^- calculation were chosen such that the metal sphere radius was slightly smaller (2.90 Bohrs) than in the divalent calculations, consistent with a contraction of the metal sphere and decrease in bond length upon increase in oxidation state. The chloride radii were the same (2.49 Bohrs) as in the other calculations.

5.3. Results

The Cl K-edge X-ray absorption spectra of the ~T_d complexes MCl_4^{n-} (M= Cu(II), Ni(II), Co(II), Fe(II) and Fe(III)) are shown in Figure 5.1a. Each spectrum exhibits a pre-edge feature in the 2819-2824 eV region which is shown in Figure 5.1b on an expanded scale. Over the divalent series, the energies of the pre-edge features vary in the order Cu(II) < Ni(II) < Co(II) < Fe(II). The $CuCl_4^{2-}$ pre-edge is lowest in energy at 2820.2 eV and the Fe(II)Cl_4^{2-} pre-edge is at highest energy, appearing as a shoulder on the rising edge at 2823.1 eV. The Fe(III)Cl_4^- pre-edge is at much lower energy than that of the ferrous complex, appearing as a well-resolved peak at 2820.8 eV. The rising edge

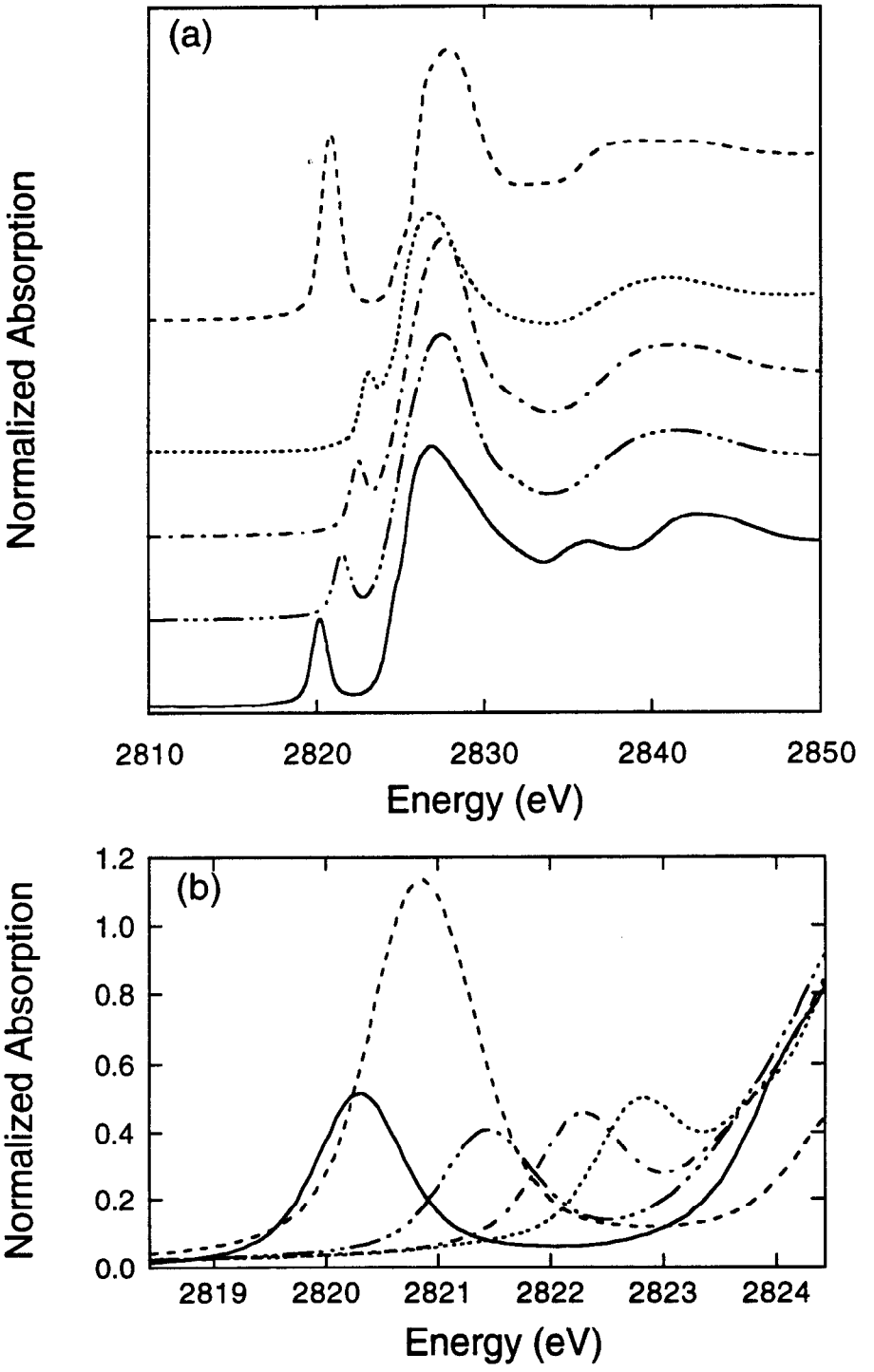

Figure 5.1. Cl K-edge XAS spectra of the T_d complexes $CuCl_4^{2-}$ (—), $NiCl_4^{2-}$ (—···), $CoCl_4^{2-}$ (-·-·), $Fe(II)Cl_4^{2-}$ (·····), and $Fe(III)Cl_4^{-}$ (---). The entire edge region of each spectrum is shown in (a). Each spectrum exhibits a pre-edge feature, which is shown on an expanded scale in (b).

energy positions in the spectra in Figure 5.1a are observed at 2825.0 eV for $Ni(II)Cl_4^{2-}$, $Co(II)Cl_4^{2-}$ and $Fe(II)Cl_4^{-}$ and at 2825.4 and 2826.0 eV for $Cu(II)Cl_4^{2-}$ and $Fe(III)Cl_4^{-}$, respectively.

The $CuCl_4^{2-}$ pre-edge is the most intense of those exhibited by the divalent centers, with the Ni(II), Co(II), and Fe(II) centers having approximately the same pre-edge intensity, within experimental error. The pre-edge of $Fe(III)Cl_4^{-}$ is more than three times as intense as that of the ferrous complex. Table 5.2 summarizes the quantitative energy and intensity of each pre-edge feature as well as the inflection point of the edge for each spectrum.

5.4. Analysis

5.4.1. Pre-edge Energies

Figure 5.2 shows an energy level diagram depicting a transition (in this case to the t_2-set) which gives rise to the pre-edge feature. As seen in Figure 5.2, a combination of factors affect the energy position of a pre-edge transition.[3] A shift in the core Cl 1s energy, which is related to the relative charge on the chloride, results in a change in the observed pre-edge energy. More charge donation to the metal results in a shift in the ligand core to deeper binding energy. In addition, the energy of the pre-edge transition depends on the metal d-derived orbital energy, which has two contributions. First, the strength of the ligand field of the complex determines the d-orbital energy splitting pattern (10Dq) and thus contributes to the metal d-derived orbital energy. Second, the overall d-manifold can shift in energy. This is related to the oxidation state and effective charge on the metal (which affects the energy of all the metal orbitals) and is also related to the coordination number of the metal (the total antibonding and repulsive interactions with the ligands), which is constant over the series examined herein. Quantitative estimates of the relative Cl 1s core energy and the ligand field contribution to the energy of a metal d-derived orbital can be obtained (*vide infra*), and, by correcting the observed pre-edge energy for these effects, the contribution to the pre-edge energy from energy shifts of the d-manifold can be determined.

The intense electric dipole-allowed transition observed at the onset of the edge jump is a Cl 1s —> 4p transition. The energy of this main edge transition is determined from the rising edge inflection point. As demonstrated in Chapter 2 (Section 2.4.1.) shifts in this energy directly reflect shifts in the Cl 1s core level in response to the relative charge on the atom.[3] Table 5.3 gives the positions of the rising edge inflection points of

Table 5.2. MCl_4^{n-} Cl K-edge Pre-edge Energies and Intensities and Rising Edge Inflection Points

Complex	Pre-edge energy[a] (eV)	Pre-edge intensity[b]	Rising edge inflection[c] (eV)
$CuCl_4^{2-}$	2820.2	0.526 ± 0.017	2825.4
$NiCl_4^{2-}$	2821.5	0.428 ± 0.017	2825.0
$CoCl_4^{2-}$	2822.5	0.419 ± 0.021	2825.0
$Fe(II)Cl_4^{2-}$	2823.1	0.427 ± 0.039	2825.0
$Fe(III)Cl_4^{-}$	2820.8	1.505 ± 0.064	2826.0

[a] The error in these energies, as determined from the standard deviation of fits to the data is ≤ ±0.009 eV.

[b] Reported error is the standard deviation of the area as determined from fits to the data and the ~3% error from normalization of the data

[c] Error in the inflection point is < ±0.1 eV; the inflection point reported is the highest energy feature in the first derivative in the rising edge region.

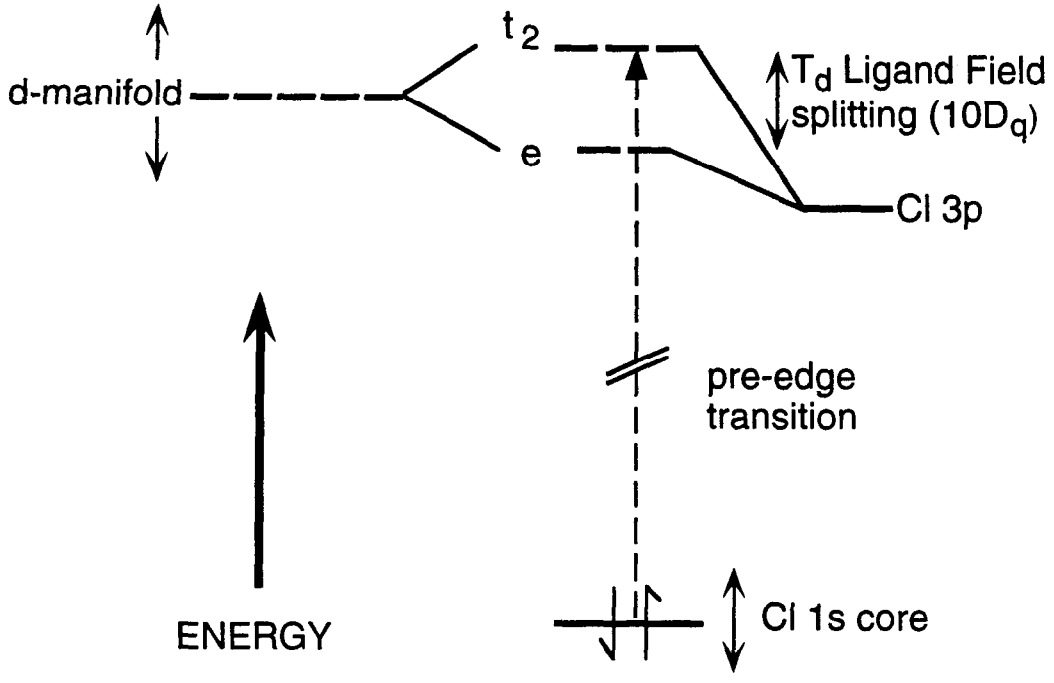

Figure 5.2. Schematic representation of the contributions to the energy of the pre-edge feature in T_d metal complexes. The pre-edge energy is determined by the Cl 1s core energy and the energy of the antibonding metal d-derived orbital. The metal d-derived orbital energy derives from the energy of the d-manifold and the ligand field splitting of the d-orbitals. The dashed arrow depicts a pre-edge transition to the t_2-set of orbitals.

Table 5.3. Cl K-edge Energy Analysis Parameters

Complex	Calc. charge	Cl 1s core energy shift relative to $CuCl_4^{2-}$ (eV)[a]	Ground State 10Dq (cm^{-1})	Excited State 10Dq (cm^{-1})[g]	Ligand Field Induced HOMO Shift (eV)[h]		Corrected pre-edge energy (eV)[i]	Relative d-manifold energy shift (eV)
					Absolute	Relative to $CuCl_4^{2-}$		
$CuCl_4^{2-}$	-0.54	0	4160/4436[b]	2496/2662[b]	0.34	0	2820.2	0
$NiCl_4^{2-}$	-0.65	+0.4	3600[c]	2160	0.10	0.24	2821.7	1.5
$CoCl_4^{2-}$	-0.65	+0.4	3000[d]	1800	0.09	0.25	2822.6	2.4
$Fe(II)Cl_4^{2-}$	-0.65	+0.4	4100[e]	2460	0.10	0.24	2823.3	3.1
$Fe(III)Cl_4^{-}$	-0.33	-0.6	6500[f]	3900	~0	0.34	2819.9	-0.3

[a] Determined from experimental rising edge inflection points. Error for these energy differences is estimated to be ±0.1 eV.

[b] Gewirth, A. A.; Cohen, S. L.; Schugar, H. J.; Solomon, E. I. *Inorg. Chem.* **1987**, *26*, 1133-1146. Values reported for $CuCl_4^{2-}$ are the 10Dq splitting and the D_{2d} splitting of the b_2 and e orbitals (see also supplementary Table 5.S1).

[c] Goodgame, D. M. L.; Goodgame, M.; Cotton, F. A. *J. Am. Chem. Soc.* **1961**, *83*, 4161-4167.

[d] Cotton, F. A.; Goodgame, D. M. L.; Goodgame, M. *J. Am. Chem. Soc.* **1961**, *83*, 4690-4699.

[e] Furlani, C.; Cervone, E.; Valenti, V. *J. Inorg. Nucl. Chem.* **1963**, *25*, 159-163.

[f] Deaton, J. C.; Gebhard, M. S.; Solomon, E. I. *Inorg. Chem.* **1989**, *28*, 877-889.

[g] The excited state 10Dq will be approximately 60% of the ground state value.[22]

[h] The shift to higher energy of the pre-edge energy due to ligand field effects is equal to 2/5(10Dq)+2/3(b_2-e splitting) for Cu(II) and 2/5(10Dq) for Ni(II) and Co(II). For Fe(II) and Fe(III) the displacement can be estimated from the energy of the transition to the e-set (*vide infra* and see Figures 5.4d-e)

[i] The corrected pre-edge energy is obtained by subtracting the relative LF shift and adding the relative Cl 1s core shift (see text).

each Cl K-edge spectrum relative to that of $CuCl_4^{2-}$. The relationship between rising edge position and chloride charge has been derived[3] (see Chapter 2, Section 2.4.1) and can be applied to these data to obtain an estimate of the charge on the chloride ligand in each complex. The charge calculated for the chloride in $CuCl_4^{2-}$ is -0.54 and in $Fe(III)Cl_4^-$ is -0.33, with the chloride in Ni(II), Co(II), and Fe(II) complexes having a charge of -0.65 (see Table 5.3).

In Cu(II), Ni(II), and Co(II) there are only vacancies in the t_2-set of T_d HOMO orbitals and thus only transitions to the t_2-set contribute to pre-edge intensity. The ligand field (LF) contribution to the pre-edge energy can be estimated from $\frac{2}{5}$ the value of 10Dq (the LF splitting of the t_2 orbitals relative to the d-manifold energy, see Figure 5.2). The value of 10Dq has been determined from analysis of the LF spectrum of each complex. The 10Dq value used in this analysis is that of the one-electron reduced (d^{n+1}) metal ion excited state, which is expected to be ~60% of the splitting in the ground state.[22] The ground state and excited state 10Dq splittings are given in Table 5.3. For $CuCl_4^{2-}$, the distortion from T_d to D_{2d} has a non-negligible effect on the HOMO energy, splitting the t_2-set into e + b_2, where b_2 is the higher-lying, half-occupied orbital to which the pre-edge transition occurs. The additional b_2 - e splitting is estimated from $X\alpha$ calculations of the site (see Supplementary Table S5.1) and is given in Table 5.3.

For Fe(III) and Fe(II) tetrachlorides, transitions to both the e-set and t_2-set of T_d orbitals contribute to the pre-edge intensity. The shift of the pre-edge energy due to LF effects must be calculated from theoretical energy and intensity ratios. In Section 5.4.2.3. we find for $Fe(III)Cl_4^-$ that the pre-edge transition to the e-set is at 2820.5 eV while the transition to the t_2-set is at 2821.0 eV. The splitting between them corresponds to the excited state d^{n+1} 10Dq. Since the e-set is at lower energy than the d-manifold by - $\frac{3}{5}$ 10Dq (see Figure 5.2), the d-manifold energy is at 2820.8 eV. The center of the observed pre-edge feature (which contains contributions from both types of transitions) is also at 2820.8 eV (Table 5.3). Thus, the effect of the ligand field on the observed pre-edge energy is negligible. For $Fe(II)Cl_4^{2-}$, the pre-edge transition to the e-set is found to be at 2822.8 eV (see Section 5.4.2.3.). Using excited state 10Dq values, the d-manifold energy is calculated as in $Fe(III)Cl_4^-$ to be 2823.0 eV, indicating that the ligand field contribution to the pre-edge feature energy is 0.10 eV. The ground state and excited state 10Dq splittings for $Fe(III)Cl_4^-$ and $Fe(II)Cl_4^{2-}$ are given in Table 5.3, in addition to the magnitude of the LF contribution to the pre-edge energy relative to $CuCl_4^{2-}$ for each MCl_4^{n-} complex.

The relative energy shifts in the Cl 1s core and the HOMO can now be used to obtain pre-edge energies which have been LF and core shift corrected. Shifts in the

HOMO energy due to LF effects are subtracted from, and the core 1s energy are added to, the observed pre-edge transition energy (see Figure 5.2).[3] These corrected pre-edge energies are given in Table 5.3. If these were the only contributions to the pre-edge energy, the corrected energy would be 2820.2 eV, the pre-edge energy for $CuCl_4^{2-}$, which has been used as the reference compound. Deviations from this value indicate that an additional effect, the overall energy of the d-manifold, must be taken into account. Table 5.3 (last column) gives the relative deviation in the corrected pre-edge energy (from 2820.2 eV), which is attributable to a d-manifold energy shift. The d-manifold energies vary in the order Fe(III) < Cu(II) < Ni(II) < Co(II) < Fe(II).

These d-manifold shifts are consistent with the periodic trend in the effective nuclear charge (Z_{eff}) on each metal. As the metal Z_{eff} increases across the first row of the periodic table for the divalent series (from Fe(II) to Cu(II)), there is a shift in the d-manifold to deeper binding energy. The d-manifold in $Fe(III)Cl_4^-$ is also significantly deeper in energy than in $Fe(II)Cl_4^{2-}$, due to oxidation of the iron. Note that over the series in Figure 5.1, the contribution to the pre-edge energy from the shift in d-manifold energy is much larger in each case than the contributions from the LF repulsion and the shift in the Cl 1s core energy.

5.4.2. Pre-edge Intensities

In this section the methodology is developed for relating pre-edge intensity to HOMO covalency in metal systems with more than one hole. The theory is developed first and then applied to experimental data, each part proceeding in several steps. In Section 5.4.2.1., strong field group theoretical predictions of possible one-electron pre-edge transitions are made. In Section 5.4.2.2.(parts *i-iv*), the irreducible tensor method is used to derive dipole strength expressions which describe the intensity of the transitions in the strong field limit. This involves writing the transitions in terms of reduced matrix elements (*i-ii*) which are then substituted with matrix elements involving one-electron molecular orbitals (*iii*). Finally, the dipole strength for each complex is calculated (*iv*). Mixing of excited states in intermediate-strength ligand fields can redistribute pre-edge intensity to higher energy. In Section 5.4.2.3., the degree of this mixing is calculated for each complex, along with the ligand field energy splittings and intensity ratios for each contributing pre-edge transition. In Section 5.4.2.4., these energy splittings and intensity ratios are applied to the experimental spectra to determine the total pre-edge transition intensity for each complex. The theoretical dipole strength expressions from Section 5.4.2.2. (part *iv*) are then applied to these data to obtain an

estimate of ligand-metal covalency. Finally, Xα calculations of these complexes are presented in Section 5.4.2.5. and compared to the experimental results.

5.4.2.1. Pre-edge Transitions in the Strong Field Limit. In order to extract information from the pre-edge transition intensity, the transitions must first be assigned. In systems with more than one d-hole, multiplet effects require a description of pre-edge transitions in terms of many-electron states. Table 5.4 gives the many-electron (d^n) ground configuration and ground state for each molecule. The one-electron excited states are derived from the d^{n+1} metal ion *parent,* which has the electron excited into the t_2 or e orbital. The ligand 1s orbitals on the four chloride ligands form an $a_1 + t_2$-set with respect to the T_d molecular symmetry. The complete final excited state then involves coupling the ligand hole (a_1 or t_2) with the d^{n+1} parent excited state. Only parent states which, after coupling in the ligand hole, result in spin- and electric dipole-allowed final states are considered. Table 5.4 gives these parent excited states and the electric dipole-allowed total final states (including the ligand core hole) in the strong field limit. $CuCl_4^{2-}$, $NiCl_4^{2-}$ and $CoCl_4^{2-}$ each have only one parent excited state ($^1A_1$, $^2T_2$, and $^3T_1$, respectively). $Fe(III)Cl_4^-$ has two excited parents states, ^5E and $^5T_2$, corresponding to transitions to the e and t_2-set, respectively. $Fe(II)Cl_4^{2-}$ has one excited parent state ($^4A_2$) arising from a transition to the e-set as well as two excited parent states arising from a transition to the t_2-set ($^4T_1 + {}^4T_2$).

5.4.2.2. Multiplet Contributions to Intensity in the Strong Field Limit. To extract ligand-metal covalency information from spectra of complexes with more than one d-manifold hole the intensity of allowed pre-edge transitions (see Table 5.4) must be related to the amount of Cl 3p character in the one-electron t_2 and e orbitals. This relationship can be derived by describing the pre-edge intensity in terms of the dipole strength (D_o), given in equation 5.1, and evaluating the dipole strength in a form which includes the one-electron orbitals.

$$D_o = \frac{1}{3|A|}\sum_{\alpha i\beta}\left|\langle A\alpha|\underline{\varrho}_i|B\beta\rangle\right|^2 \qquad (5.1)$$

A and *B* are the many-electron ground and excited states, respectively, |*A*| is the degeneracy of the ground state, $\underline{\varrho}$ is the electric dipole operator, and α, i, β are components of the ground state, operator, and excited state, respectively.

Equation 5.1 can be evaluated by construction of all the ground and excited state wavefunctions for each metal center. This is an involved and lengthy procedure. An alternative to this approach is employed herein. The irreducible tensor method[23] uses the

Table 5.4. Ground States and Group Theoretically-Allowed Excited States for MCl_4^{n-} Pre-edge Transitions

Complex	Ground d^n	Ground Configuration (holes)	Ground State	Excited Configuration (holes)§	Parent d^{n+1} Excited State	Allowed Excited State (from ligand a_1)	Allowed Excited State (from ligand t_2)
$CuCl_4^{2-}$	d^9	t_2	$^2T_2$	t_2^0	$^1A_1$	$^2A_1$	$^2T_2$
$NiCl_4^{2-}$	d^8	t_2^2	$^3T_1$	t_2^1	$^2T_2$	$^3T_2$	$^3E+^3T_1+^3T_2$
$CoCl_4^{2-}$	d^7	t_2^3	$^4A_2$	t_2^2	$^3T_1$†	$^4T_1$	$^4T_1$
$Fe(II)Cl_4^{2-}$	d^6	et_2^3	^5E	t_2^3	$^4A_2$	-	$^5T_1$
				et_2^2	$^4T_2$	$^5T_2$	$^5T_1+^5T_2$
					$^4T_1$†	$^5T_1$	$^5T_1+^5T_2$
$Fe(III)Cl_4^-$	d^5	$e^2t_2^3$	$^6A_1$	et_2^3	^5E	-	$^6T_2$
				$e^2t_2^2$	$^5T_2$	$^6T_2$	$^6T_2$

§ Excited state configurations are given in the strong field limit.

† States for which intermediate ligand field mixing with higher lying states of the same symmetry is possible.

Wigner-Eckart theorem, thereby taking advantage of symmetry to simplify the problem. For this analysis, the notation and tables of Piepho and Schatz will be used throughout.[24] The first step of this procedure involves the construction of reduced matrix elements.

(*i*) Construction of Reduced Matrix Elements. Using the irreducible tensor method, each matrix element which may contribute to pre-edge intensity is rewritten, according to equation 5.2, as a 2j phase factor and a 3j symbol times a many-electron reduced matrix element, $\langle A\|\underline{o}\|B\rangle$, which is independent of the components of the states.

$$\langle A\alpha|\underline{o}_i|B\beta\rangle = \begin{pmatrix} A \\ \alpha \end{pmatrix}\begin{pmatrix} A & \underline{o} & B \\ \alpha & i & \beta \end{pmatrix}\langle A\|\underline{o}\|B\rangle \tag{5.2}$$

The many-electron reduced matrix element is then further reduced to a one-electron reduced matrix element using equation 5.3 in which $\langle A\|\underline{o}\|B\rangle$ is rewritten and expanded as

$$\begin{aligned}\left\langle \mathcal{A}\left(a^m(S_1h_1),b^{n-1}(S_2h_2)\right) ShM \,\|\, \underline{o} \,\|\, \mathcal{A}\left(a^{m-1}(S_1'h_1'),b^n(S_2'h_2')\right)S'h'M'\right\rangle \\ = (b,b^{n-1}\,S_2h_2|b^n\,Sh')\sqrt{n}(|h'\|h|)^{\frac{1}{2}}\{h_1h_2h\}\begin{Bmatrix} h' & b & h_2 \\ h_1 & h & T_2 \end{Bmatrix}\langle a\|\underline{o}\|b\rangle\end{aligned} \tag{5.3}$$

where S' is the total spin of the ground state, h' is the many-electron ground state, and M' is the m_s of the ground state. The notation for the excited state is identical, but without the prime designator. The ground state configuration is given as $a^{m-1}b^n$ and the excited state is a^mb^{n-1} (for transitions in terms of holes); a is the ligand core orbital and b is the HOMO orbital in each case. S_1' is the total spin and h_1' is the many-electron state arising from the a^{m-1} configuration. $S_2'h_2'$, S_1h_1, S_2h_2 are analogously defined for the b^n, a^m, and b^{n-1}configurations, respectively. $\left|\mathcal{A}\left(a^{m-1}(S_1'h_1'),b^n(S_2'h_2')\right)S'h'M'\right\rangle$ denotes the antisymmetrized wavefunction ($\mathcal{A}$) which couples the $S_1'h_1'$ and $S_2'h_2'$ states to make the total $S'h'M'$ ground state. The excited state is similarly defined.

Equation 5.3 is a modification of Piepho and Schatz[24] equation 20.1.10, which can be simplified for these examples because $m = 1$, $S_1' = 0$, $S' = S$, $h_1' = A_1$, $a = h_1$, $S_1 = \frac{1}{2}$, the T_d electric dipole operator ($\underline{o}$) is t_2, and the coefficient of fractional parentage for the core hole state is always 1. Because these substitutions are applicable to all b^n configurations, equation 5.3 can be applied to any T_d hole configuration.

Electrons which are in a partially-occupied level which is not involved in a particular transition are called passive electrons. For example, the electrons in the e-set

are passive for the following transition written in terms of holes: $a_1^0e^1t_2^3 \longrightarrow a_1^1e^1t_2^2$. For cases with passive electrons (Fe(II) and Fe(III)), an additional step, using equation 5.4, must be taken (before application of equation 5.3) to decouple the passive electrons from the problem.

$$\left\langle \mathcal{A}\left\{\left[\left(a^m(S_1h_1),b^{n-1}(S_2h_2)\right)S_{12}h_{12}\right],c^l(S_3h_3)\right\}ShM \,\|\, \underline{o} \,\|\, \mathcal{A}\left\{\left[\left(a^{m-1}(S_1'h_1'),b^n(S_2'h_2')\right)S_{12}'h_{12}'\right],c^l(S_3'h_3')\right\}S'h'M'\right\rangle$$
$$= \delta_{spin}\left[\delta_{h_3h_3'}|h|^{1/2}|h'|^{1/2}\{h_{12}h_3h\}\{h_{12}T_2h_{12}'\}\begin{Bmatrix} T_2 & h' & h \\ h_3 & h_{12} & h_{12}' \end{Bmatrix} \times\left\langle \mathcal{A}\left(a^m(S_1h_1),b^{n-1}(S_2h_2)\right)S_{12}h_{12}M_{12} \,\|\, \underline{o} \,\|\, \mathcal{A}\left(a^{m-1}(S_1'h_1'),b^n(S_2'h_2')\right)S_{12}'h_{12}'M_{12}\right\rangle\right] \tag{5.4}$$

with $\delta_{spin} = \delta_{S_{12}S_{12}'}\delta_{S_3S_3'}\delta_{SS'}\delta_{MM'}$. The notation is analogous to that in equation 5.3, with c^l referring to the passive electrons and $S_{12}h_{12}$ and $S_{12}'h_{12}'$ being subsequently substituted for Sh and $S'h'$ in equation 5.3.

(ii) **Calculation of Reduced Matrix Elements for T_d MCl_4^{n-}.** Tables 5.5a-e give the steps in the reduction of the matrix elements for each pre-edge transition in each T_d MCl_4^{n-} (M = Cu(II), Ni(II), Co(II), Fe(II), and Fe(III)). Each pre-edge transition is designated by its total excited state (which includes the ligand core hole), by its excited state d^{n+1} parent state (given in parentheses),[25] and by its one-electron orbital transition. The results are given in terms of the squares of each matrix element for summation in the dipole strength expression (equation 5.1). The necessary 3j and 6j symbols were obtained from Piepho and Schatz, Tables C.12.1. and C.13.1.[24] Note from Table 5.5 that the many-electron reduced matrix elements for all MCl_4^{n-} reduce to three one-electron reduced matrix elements: $< a_1 \| t_2 \| t_2 >$, $< t_2 \| t_2 \| t_2 >$, and $< t_2 \| t_2 \| e >$.

(iii) **Evaluation of Reduced Matrix Elements in Terms of Molecular Orbitals.** The one-electron reduced matrix elements, $< a_1 \| t_2 \| t_2 >$, $< t_2 \| t_2 \| t_2 >$, and $< t_2 \| t_2 \| e >$, can be evaluated using equation 5.2, rewritten below (equation 5.2') for the application to orbitals instead of states.

$$\langle a\alpha|\underline{o}_i|b\beta\rangle = \begin{pmatrix} a \\ \alpha \end{pmatrix}\begin{pmatrix} a & \underline{o} & b \\ \alpha & i & \beta \end{pmatrix}\langle a\|\underline{o}\|b\rangle \tag{5.2'}$$

Table 5.5. Irreducible Tensor Method Applied to Pre-edge Transition Matrix Elements

Table 5.5a. T_d d^1 hole[a]

Transition[b] $^2T_2$ (GS)	Square of Matrix Elements	Square of Many-Electron State Reduced Matrix Elements	Square of One-Electron Reduced Matrix Elements
$\longrightarrow (^1A_1)\ ^2A_1$	$\langle A_1 \mid T_2(x) \mid T_2(x) \rangle^2$	$\frac{1}{3}\langle A_1 \parallel T_2 \parallel T_2 \rangle^2$	$\frac{1}{3}\langle a_1 \parallel t_2 \parallel t_2 \rangle^2$
$(a_1 \longrightarrow t_2)$	$\langle A_1 \mid T_2(y) \mid T_2(y) \rangle^2$	$\frac{1}{3}\langle A_1 \parallel T_2 \parallel T_2 \rangle^2$	$\frac{1}{3}\langle a_1 \parallel t_2 \parallel t_2 \rangle^2$
	$\langle A_1 \mid T_2(z) \mid T_2(z) \rangle^2$	$\frac{1}{3}\langle A_1 \parallel T_2 \parallel T_2 \rangle^2$	$\frac{1}{3}\langle a_1 \parallel t_2 \parallel t_2 \rangle^2$
$\longrightarrow (^1A_1)\ ^2T_2$	$\langle T_2(z) \mid T_2(y) \mid T_2(x) \rangle^2$	$\frac{1}{6}\langle T_2 \parallel T_2 \parallel T_2 \rangle^2$	$\frac{1}{6}\langle t_2 \parallel t_2 \parallel t_2 \rangle^2$
$(t_2 \longrightarrow t_2)$	$\langle T_2(y) \mid T_2(z) \mid T_2(x) \rangle^2$	$\frac{1}{6}\langle T_2 \parallel T_2 \parallel T_2 \rangle^2$	$\frac{1}{6}\langle t_2 \parallel t_2 \parallel t_2 \rangle^2$
	$\langle T_2(z) \mid T_2(x) \mid T_2(y) \rangle^2$	$\frac{1}{6}\langle T_2 \parallel T_2 \parallel T_2 \rangle^2$	$\frac{1}{6}\langle t_2 \parallel t_2 \parallel t_2 \rangle^2$
	$\langle T_2(x) \mid T_2(z) \mid T_2(y) \rangle^2$	$\frac{1}{6}\langle T_2 \parallel T_2 \parallel T_2 \rangle^2$	$\frac{1}{6}\langle t_2 \parallel t_2 \parallel t_2 \rangle^2$
	$\langle T_2(x) \mid T_2(y) \mid T_2(z) \rangle^2$	$\frac{1}{6}\langle T_2 \parallel T_2 \parallel T_2 \rangle^2$	$\frac{1}{6}\langle t_2 \parallel t_2 \parallel t_2 \rangle^2$
	$\langle T_2(y) \mid T_2(x) \mid T_2(z) \rangle^2$	$\frac{1}{6}\langle T_2 \parallel T_2 \parallel T_2 \rangle^2$	$\frac{1}{6}\langle t_2 \parallel t_2 \parallel t_2 \rangle^2$

[a] Each column of the table can be directly equated to the one to its left.

[b] Excited states are written with their parent d^{n+1} states in parentheses.

Table 5.5b. T_d d^2 holes[a]

Transition[b] $^3T_1$ (GS)	Square of Matrix Elements	Square of Many-Electron State Reduced Matrix Elements	Square of One-Electron Reduced Matrix Elements
$\longrightarrow (^2T_2)\ ^3T_2$	$\langle T_2(z) \mid T_2(y) \mid T_1(x) \rangle^2$	$\frac{1}{6}\langle T_2 \Vert T_2 \Vert T_1 \rangle^2$	$\frac{1}{3}\langle a_1 \Vert t_2 \Vert t_2 \rangle^2$
$(a_1 \longrightarrow t_2)$	$\langle T_2(y) \mid T_2(z) \mid T_1(x) \rangle^2$	$\frac{1}{6}\langle T_2 \Vert T_2 \Vert T_1 \rangle^2$	$\frac{1}{3}\langle a_1 \Vert t_2 \Vert t_2 \rangle^2$
	$\langle T_2(z) \mid T_2(x) \mid T_1(y) \rangle^2$	$\frac{1}{6}\langle T_2 \Vert T_2 \Vert T_1 \rangle^2$	$\frac{1}{3}\langle a_1 \Vert t_2 \Vert t_2 \rangle^2$
	$\langle T_2(x) \mid T_2(z) \mid T_1(y) \rangle^2$	$\frac{1}{6}\langle T_2 \Vert T_2 \Vert T_1 \rangle^2$	$\frac{1}{3}\langle a_1 \Vert t_2 \Vert t_2 \rangle^2$
	$\langle T_2(x) \mid T_2(y) \mid T_1(z) \rangle^2$	$\frac{1}{6}\langle T_2 \Vert T_2 \Vert T_1 \rangle^2$	$\frac{1}{3}\langle a_1 \Vert t_2 \Vert t_2 \rangle^2$
	$\langle T_2(y) \mid T_2(x) \mid T_1(z) \rangle^2$	$\frac{1}{6}\langle T_2 \Vert T_2 \Vert T_1 \rangle^2$	$\frac{1}{3}\langle a_1 \Vert t_2 \Vert t_2 \rangle^2$
$\longrightarrow (^2T_2)\ ^3E$	$\langle E(\theta) \mid T_2(x) \mid T_1(x) \rangle^2$	$\frac{1}{4}\langle E \Vert T_2 \Vert T_1 \rangle^2$	$\frac{1}{4}\langle t_2 \Vert t_2 \Vert t_2 \rangle^2$
$(t_2 \longrightarrow t_2)$	$\langle E(\varepsilon) \mid T_2(x) \mid T_1(x) \rangle^2$	$\frac{1}{12}\langle E \Vert T_2 \Vert T_1 \rangle^2$	$\frac{1}{12}\langle t_2 \Vert t_2 \Vert t_2 \rangle^2$
	$\langle E(\theta) \mid T_2(y) \mid T_1(y) \rangle^2$	$\frac{1}{4}\langle E \Vert T_2 \Vert T_1 \rangle^2$	$\frac{1}{4}\langle t_2 \Vert t_2 \Vert t_2 \rangle^2$
	$\langle E(\varepsilon) \mid T_2(y) \mid T_1(y) \rangle^2$	$\frac{1}{12}\langle E \Vert T_2 \Vert T_1 \rangle^2$	$\frac{1}{12}\langle t_2 \Vert t_2 \Vert t_2 \rangle^2$
	$\langle E(\varepsilon) \mid T_2(z) \mid T_1(z) \rangle^2$	$\frac{1}{3}\langle E \Vert T_2 \Vert T_1 \rangle^2$	$\frac{1}{3}\langle t_2 \Vert t_2 \Vert t_2 \rangle^2$
$\longrightarrow (^2T_2)\ ^3T_1$	$\langle T_1(z) \mid T_2(y) \mid T_1(x) \rangle^2$	$\frac{1}{6}\langle T_1 \Vert T_2 \Vert T_1 \rangle^2$	$\frac{1}{12}\langle t_2 \Vert t_2 \Vert t_2 \rangle^2$
$(t_2 \longrightarrow t_2)$	$\langle T_1(y) \mid T_2(z) \mid T_1(x) \rangle^2$	$\frac{1}{6}\langle T_1 \Vert T_2 \Vert T_1 \rangle^2$	$\frac{1}{12}\langle t_2 \Vert t_2 \Vert t_2 \rangle^2$
	$\langle T_1(z) \mid T_2(x) \mid T_1(y) \rangle^2$	$\frac{1}{6}\langle T_1 \Vert T_2 \Vert T_1 \rangle^2$	$\frac{1}{12}\langle t_2 \Vert t_2 \Vert t_2 \rangle^2$
	$\langle T_1(x) \mid T_2(z) \mid T_1(y) \rangle^2$	$\frac{1}{6}\langle T_1 \Vert T_2 \Vert T_1 \rangle^2$	$\frac{1}{12}\langle t_2 \Vert t_2 \Vert t_2 \rangle^2$
	$\langle T_1(x) \mid T_2(y) \mid T_1(z) \rangle^2$	$\frac{1}{6}\langle T_1 \Vert T_2 \Vert T_1 \rangle^2$	$\frac{1}{12}\langle t_2 \Vert t_2 \Vert t_2 \rangle^2$
	$\langle T_1(y) \mid T_2(x) \mid T_1(z) \rangle^2$	$\frac{1}{6}\langle T_1 \Vert T_2 \Vert T_1 \rangle^2$	$\frac{1}{12}\langle t_2 \Vert t_2 \Vert t_2 \rangle^2$

[a] Each column of the table can be directly equated to the one to its left.

[b] Excited states are written with their parent d^{n+1} states in parentheses.

Table 5.5b. T_d d^2 holes[a] (continued)

Transition[b] $^3T_1$ (GS)	Square of Matrix Elements	Square of Many-Electron State Reduced Matrix Elements	Square of One-Electron Reduced Matrix Elements
$\longrightarrow (^2T_2)\ ^3T_2$	$\langle T_2(z) \mid T_2(y) \mid T_1(x) \rangle^2$	$\frac{1}{6}\langle T_2 \parallel T_2 \parallel T_1 \rangle^2$	$\frac{1}{12}\langle t_2 \parallel t_2 \parallel t_2 \rangle^2$
$(t_2 \longrightarrow t_2)$	$\langle T_2(y) \mid T_2(z) \mid T_1(x) \rangle^2$	$\frac{1}{6}\langle T_2 \parallel T_2 \parallel T_1 \rangle^2$	$\frac{1}{12}\langle t_2 \parallel t_2 \parallel t_2 \rangle^2$
	$\langle T_2(z) \mid T_2(x) \mid T_1(y) \rangle^2$	$\frac{1}{6}\langle T_2 \parallel T_2 \parallel T_1 \rangle^2$	$\frac{1}{12}\langle t_2 \parallel t_2 \parallel t_2 \rangle^2$
	$\langle T_2(x) \mid T_2(z) \mid T_1(y) \rangle^2$	$\frac{1}{6}\langle T_2 \parallel T_2 \parallel T_1 \rangle^2$	$\frac{1}{12}\langle t_2 \parallel t_2 \parallel t_2 \rangle^2$
	$\langle T_2(x) \mid T_2(y) \mid T_1(z) \rangle^2$	$\frac{1}{6}\langle T_2 \parallel T_2 \parallel T_1 \rangle^2$	$\frac{1}{12}\langle t_2 \parallel t_2 \parallel t_2 \rangle^2$
	$\langle T_2(y) \mid T_2(x) \mid T_1(z) \rangle^2$	$\frac{1}{6}\langle T_2 \parallel T_2 \parallel T_1 \rangle^2$	$\frac{1}{12}\langle t_2 \parallel t_2 \parallel t_2 \rangle^2$

[a] Each column of the table can be directly equated to the one to its left.
[b] Excited states are written with their parent d^{n+1} states in parentheses.

Table 5.5c. T_d d^3 holes[a]

Transition[b] $^4A_2$ (GS)	Square of Matrix Elements	Square of Many-Electron State Reduced Matrix Elements	Square of One-Electron Reduced Matrix Elements
$\longrightarrow (^3T_1)\ ^4T_1$	$\langle T_1(x) \mid T_2(x) \mid A_2 \rangle^2$	$\frac{1}{3}\langle T_1 \parallel T_2 \parallel A_2 \rangle^2$	$\frac{1}{3}\langle a_1 \parallel t_2 \parallel t_2 \rangle^2$
$(a_1 \longrightarrow t_2)$	$\langle T_1(y) \mid T_2(y) \mid A_2 \rangle^2$	$\frac{1}{3}\langle T_1 \parallel T_2 \parallel A_2 \rangle^2$	$\frac{1}{3}\langle a_1 \parallel t_2 \parallel t_2 \rangle^2$
	$\langle T_1(z) \mid T_2(z) \mid A_2 \rangle^2$	$\frac{1}{3}\langle T_1 \parallel T_2 \parallel A_2 \rangle^2$	$\frac{1}{3}\langle a_1 \parallel t_2 \parallel t_2 \rangle^2$
$\longrightarrow (^3T_1)\ ^4T_1$	$\langle T_1(x) \mid T_2(x) \mid A_2 \rangle^2$	$\frac{1}{3}\langle T_1 \parallel T_2 \parallel A_2 \rangle^2$	$\frac{1}{3}\langle t_2 \parallel t_2 \parallel t_2 \rangle^2$
$(t_2 \longrightarrow t_2)$	$\langle T_1(y) \mid T_2(y) \mid A_2 \rangle^2$	$\frac{1}{3}\langle T_1 \parallel T_2 \parallel A_2 \rangle^2$	$\frac{1}{3}\langle t_2 \parallel t_2 \parallel t_2 \rangle^2$
	$\langle T_1(z) \mid T_2(z) \mid A_2 \rangle^2$	$\frac{1}{3}\langle T_1 \parallel T_2 \parallel A_2 \rangle^2$	$\frac{1}{3}\langle t_2 \parallel t_2 \parallel t_2 \rangle^2$

[a] Each column of the table can be directly equated to the one to its left.
[b] Excited states are written with their parent d^{n+1} states in parentheses.

Table 5.5d. T_d d^4 holes[a]

Transition[b] ^5E (GS)	Square of Matrix Elements	Square of Many-Electron State Reduced Matrix Elements	Square of One-Electron Reduced Matrix Elements
$\longrightarrow (^4A_2)\ ^5T_1$	$\langle T_1(x) \mid T_2(x) \mid E(\theta)\rangle^2$	$\frac{1}{4}\langle T_1 \Vert T_2 \Vert E\rangle^2$	$\frac{1}{4}\langle t_2 \Vert t_2 \Vert e\rangle^2$
$(t_2 \longrightarrow e)$	$\langle T_1(x) \mid T_2(x) \mid E(\varepsilon)\rangle^2$	$\frac{1}{12}\langle T_1 \Vert T_2 \Vert E\rangle^2$	$\frac{1}{12}\langle t_2 \Vert t_2 \Vert e\rangle^2$
	$\langle T_1(y) \mid T_2(y) \mid E(\theta)\rangle^2$	$\frac{1}{4}\langle T_1 \Vert T_2 \Vert E\rangle^2$	$\frac{1}{4}\langle t_2 \Vert t_2 \Vert e\rangle^2$
	$\langle T_1(y) \mid T_2(y) \mid E(\varepsilon)\rangle^2$	$\frac{1}{12}\langle T_1 \Vert T_2 \Vert E\rangle^2$	$\frac{1}{12}\langle t_2 \Vert t_2 \Vert e\rangle^2$
	$\langle T_1(z) \mid T_2(z) \mid E(\varepsilon)\rangle^2$	$\frac{1}{3}\langle T_1 \Vert T_2 \Vert E\rangle^2$	$\frac{1}{3}\langle t_2 \Vert t_2 \Vert e\rangle^2$
$\longrightarrow (^4T_2)\ ^5T_2$	$\langle T_2(x) \mid T_2(x) \mid E(\theta)\rangle^2$	$\frac{1}{12}\langle T_2 \Vert T_2 \Vert E\rangle^2$	$\frac{1}{12}\langle a_1 \Vert t_2 \Vert t_2\rangle^2$
$(a_1 \longrightarrow t_2)$	$\langle T_2(x) \mid T_2(x) \mid E(\varepsilon)\rangle^2$	$\frac{1}{4}\langle T_2 \Vert T_2 \Vert E\rangle^2$	$\frac{1}{4}\langle a_1 \Vert t_2 \Vert t_2\rangle^2$
	$\langle T_2(y) \mid T_2(y) \mid E(\theta)\rangle^2$	$\frac{1}{12}\langle T_2 \Vert T_2 \Vert E\rangle^2$	$\frac{1}{12}\langle a_1 \Vert t_2 \Vert t_2\rangle^2$
	$\langle T_2(y) \mid T_2(y) \mid E(\varepsilon)\rangle^2$	$\frac{1}{4}\langle T_2 \Vert T_2 \Vert E\rangle^2$	$\frac{1}{4}\langle a_1 \Vert t_2 \Vert t_2\rangle^2$
	$\langle T_2(z) \mid T_2(z) \mid E(\theta)\rangle^2$	$\frac{1}{3}\langle T_2 \Vert T_2 \Vert E\rangle^2$	$\frac{1}{3}\langle a_1 \Vert t_2 \Vert t_2\rangle^2$
$\longrightarrow (^4T_2)\ ^5T_1$	$\langle T_1(x) \mid T_2(x) \mid E(\theta)\rangle^2$	$\frac{1}{4}\langle T_1 \Vert T_2 \Vert E\rangle^2$	$\frac{1}{4}\langle t_2 \Vert t_2 \Vert t_2\rangle^2$
$(t_2 \longrightarrow t_2)$	$\langle T_1(x) \mid T_2(x) \mid E(\varepsilon)\rangle^2$	$\frac{1}{12}\langle T_1 \Vert T_2 \Vert E\rangle^2$	$\frac{1}{12}\langle t_2 \Vert t_2 \Vert t_2\rangle^2$
	$\langle T_1(y) \mid T_2(y) \mid E(\theta)\rangle^2$	$\frac{1}{4}\langle T_1 \Vert T_2 \Vert E\rangle^2$	$\frac{1}{4}\langle t_2 \Vert t_2 \Vert t_2\rangle^2$
	$\langle T_1(y) \mid T_2(y) \mid E(\varepsilon)\rangle^2$	$\frac{1}{12}\langle T_1 \Vert T_2 \Vert E\rangle^2$	$\frac{1}{12}\langle t_2 \Vert t_2 \Vert t_2\rangle^2$
	$\langle T_1(z) \mid T_2(z) \mid E(\varepsilon)\rangle^2$	$\frac{1}{3}\langle T_1 \Vert T_2 \Vert E\rangle^2$	$\frac{1}{3}\langle t_2 \Vert t_2 \Vert t_2\rangle^2$
$\longrightarrow (^4T_2)\ ^5T_2$	$\langle T_2(x) \mid T_2(x) \mid E(\theta)\rangle^2$	$\frac{1}{12}\langle T_2 \Vert T_2 \Vert E\rangle^2$	0
$(t_2 \longrightarrow t_2)$	$\langle T_2(x) \mid T_2(x) \mid E(\varepsilon)\rangle^2$	$\frac{1}{4}\langle T_2 \Vert T_2 \Vert E\rangle^2$	0
	$\langle T_2(y) \mid T_2(y) \mid E(\theta)\rangle^2$	$\frac{1}{12}\langle T_2 \Vert T_2 \Vert E\rangle^2$	0
	$\langle T_2(y) \mid T_2(y) \mid E(\varepsilon)\rangle^2$	$\frac{1}{4}\langle T_2 \Vert T_2 \Vert E\rangle^2$	0
	$\langle T_2(z) \mid T_2(z) \mid E(\theta)\rangle^2$	$\frac{1}{3}\langle T_2 \Vert T_2 \Vert E\rangle^2$	0

[a] Each column of the table can be directly equated to the one to its left.
[b] Excited states are written with their parent d^{n+1} states in parentheses.

Table 5.5d. T_d d^4 holes[a] (continued)

Transition[b] ^5E (GS)	Square of Matrix Elements	Square of Many-Electron State Reduced Matrix Elements	Square of One-Electron Reduced Matrix Elements
$\longrightarrow (^4T_1)\ ^5T_1$	$\langle T_1(x) \mid T_2(x) \mid E(\theta)\rangle^2$	$\frac{1}{4}\langle T_1 \Vert T_2 \Vert E\rangle^2$	$\frac{1}{4}\langle a_1 \Vert t_2 \Vert t_2\rangle^2$
$(a_1 \longrightarrow t_2)$	$\langle T_1(x) \mid T_2(x) \mid E(\varepsilon)\rangle^2$	$\frac{1}{12}\langle T_1 \Vert T_2 \Vert E\rangle^2$	$\frac{1}{12}\langle a_1 \Vert t_2 \Vert t_2\rangle^2$
	$\langle T_1(y) \mid T_2(y) \mid E(\theta)\rangle^2$	$\frac{1}{4}\langle T_1 \Vert T_2 \Vert E\rangle^2$	$\frac{1}{4}\langle a_1 \Vert t_2 \Vert t_2\rangle^2$
	$\langle T_1(y) \mid T_2(y) \mid E(\varepsilon)\rangle^2$	$\frac{1}{12}\langle T_1 \Vert T_2 \Vert E\rangle^2$	$\frac{1}{12}\langle a_1 \Vert t_2 \Vert t_2\rangle^2$
	$\langle T_1(z) \mid T_2(z) \mid E(\varepsilon)\rangle^2$	$\frac{1}{3}\langle T_1 \Vert T_2 \Vert E\rangle^2$	$\frac{1}{3}\langle a_1 \Vert t_2 \Vert t_2\rangle^2$
$\longrightarrow (^4T_1)\ ^5T_1$	$\langle T_1(x) \mid T_2(x) \mid E(\theta)\rangle^2$	$\frac{1}{4}\langle T_1 \Vert T_2 \Vert E\rangle^2$	0
$(t_2 \longrightarrow t_2)$	$\langle T_1(x) \mid T_2(x) \mid E(\varepsilon)\rangle^2$	$\frac{1}{12}\langle T_1 \Vert T_2 \Vert E\rangle^2$	0
	$\langle T_1(y) \mid T_2(y) \mid E(\theta)\rangle^2$	$\frac{1}{4}\langle T_1 \Vert T_2 \Vert E\rangle^2$	0
	$\langle T_1(y) \mid T_2(y) \mid E(\varepsilon)\rangle^2$	$\frac{1}{12}\langle T_1 \Vert T_2 \Vert E\rangle^2$	0
	$\langle T_1(z) \mid T_2(z) \mid E(\varepsilon)\rangle^2$	$\frac{1}{3}\langle T_1 \Vert T_2 \Vert E\rangle^2$	0
$\longrightarrow (^4T_1)\ ^5T_2$	$\langle T_2(x) \mid T_2(x) \mid E(\theta)\rangle^2$	$\frac{1}{12}\langle T_2 \Vert T_2 \Vert E\rangle^2$	$\frac{1}{12}\langle t_2 \Vert t_2 \Vert t_2\rangle^2$
$(t_2 \longrightarrow t_2)$	$\langle T_2(x) \mid T_2(x) \mid E(\varepsilon)\rangle^2$	$\frac{1}{4}\langle T_2 \Vert T_2 \Vert E\rangle^2$	$\frac{1}{4}\langle t_2 \Vert t_2 \Vert t_2\rangle^2$
	$\langle T_2(y) \mid T_2(y) \mid E(\theta)\rangle^2$	$\frac{1}{12}\langle T_2 \Vert T_2 \Vert E\rangle^2$	$\frac{1}{12}\langle t_2 \Vert t_2 \Vert t_2\rangle^2$
	$\langle T_2(y) \mid T_2(y) \mid E(\varepsilon)\rangle^2$	$\frac{1}{4}\langle T_2 \Vert T_2 \Vert E\rangle^2$	$\frac{1}{4}\langle t_2 \Vert t_2 \Vert t_2\rangle^2$
	$\langle T_2(z) \mid T_2(z) \mid E(\theta)\rangle^2$	$\frac{1}{3}\langle T_2 \Vert T_2 \Vert E\rangle^2$	$\frac{1}{3}\langle t_2 \Vert t_2 \Vert t_2\rangle^2$

[a] Each column of the table can be directly equated to the one to its left.
[b] Excited states are written with their parent d^{n+1} states in parentheses.

Table 5.5e. T_d d^5 holes[a]

Transition[b] $^6A_1$ (GS)	Square of Matrix Elements	Square of Many-Electron State Reduced Matrix Elements	Square of One-Electron Reduced Matrix Elements
—> (^{5}E) $^6T_2$	$<T_2(x) \mid T_2(x) \mid A_1>^2$	$\frac{1}{3}<T_2 \parallel T_2 \parallel A_1>^2$	$\frac{1}{3}<t_2 \parallel t_2 \parallel e>^2$
(t_2 —> e)	$<T_2(y) \mid T_2(y) \mid A_1>^2$	$\frac{1}{3}<T_2 \parallel T_2 \parallel A_1>^2$	$\frac{1}{3}<t_2 \parallel t_2 \parallel e>^2$
	$<T_2(z) \mid T_2(z) \mid A_1>^2$	$\frac{1}{3}<T_2 \parallel T_2 \parallel A_1>^2$	$\frac{1}{3}<t_2 \parallel t_2 \parallel e>^2$
—> ($^5T_2$) $^6T_2$	$<T_2(x) \mid T_2(x) \mid A_1>^2$	$\frac{1}{3}<T_2 \parallel T_2 \parallel A_1>^2$	$\frac{1}{3}<a_1 \parallel t_2 \parallel t_2>^2$
(a_1 —> t_2)	$<T_2(y) \mid T_2(y) \mid A_1>^2$	$\frac{1}{3}<T_2 \parallel T_2 \parallel A_1>^2$	$\frac{1}{3}<a_1 \parallel t_2 \parallel t_2>^2$
	$<T_2(z) \mid T_2(z) \mid A_1>^2$	$\frac{1}{3}<T_2 \parallel T_2 \parallel A_1>^2$	$\frac{1}{3}<a_1 \parallel t_2 \parallel t_2>^2$
—> ($^5T_2$) $^6T_2$	$<T_2(x) \mid T_2(x) \mid A_1>^2$	$\frac{1}{3}<T_2 \parallel T_2 \parallel A_1>^2$	$\frac{1}{3}<t_2 \parallel t_2 \parallel t_2>^2$
(t_2 —> t_2)	$<T_2(y) \mid T_2(y) \mid A_1>^2$	$\frac{1}{3}<T_2 \parallel T_2 \parallel A_1>^2$	$\frac{1}{3}<t_2 \parallel t_2 \parallel t_2>^2$
	$<T_2(z) \mid T_2(z) \mid A_1>^2$	$\frac{1}{3}<T_2 \parallel T_2 \parallel A_1>^2$	$\frac{1}{3}<t_2 \parallel t_2 \parallel t_2>^2$

[a] Each column of the table can be directly equated to the one to its left.

[b] Excited states are written with their parent d^{n+1} states in parentheses.

The solution of equation 5.2' requires the evaluation of a single one-electron matrix element $< a\alpha \mid \varrho_i \mid b\beta >$ using symmetry-adapted linear combinations (SALC's) of atomic orbitals for the one-electron orbital wavefunctions. The linear combinations of Cl 1s orbitals, as well as the t_2 and e one-electron HOMO orbitals (which contain both metal 3d- and ligand 3p-character) are given in Table 5.6. The coefficients c_1 and c_2 describe the ligand 3p-σ and 3p-π contributions to the t_2-set, respectively; and the c_3 coefficient reflects the ligand 3p π-component in the e-set. The wavefunctions in Table 5.6 are those of Ballhausen and Gray[26] for the T_d geometry and ligand 3p-vectors as defined in Figure 5.3. The molecular axis system is designated x, y, z, and the local axis system of each ligand is designated x', y', z'.

For molecular orbitals, $a\alpha$ and $b\beta$, written as $a\alpha = C_M\chi_M + C_L\chi_L$, where χ_M and χ_L are symmetry-adapted metal and ligand combinations, the expansion of the one-electron matrix element $\langle a\alpha|\mathbf{r}|b\beta\rangle$ is given by equation 5.5 and includes metal-metal, metal-ligand, and ligand-ligand terms.

$$\langle a\alpha|\mathbf{r}|b\beta\rangle = C_M C_M' \langle \chi_M|\mathbf{r}|\chi_M'\rangle + C_M C_L' \langle \chi_M|\mathbf{r}|\chi_L'\rangle + C_L C_L' \langle \chi_L|\mathbf{r}|\chi_L'\rangle \quad (5.5)$$

It has been demonstrated for ligand-to-metal charge transfer (LMCT) transitions that the ligand-ligand term gives the dominant contribution to $\langle a\alpha|\mathbf{r}|b\beta\rangle$.[27-29] The approximation, which neglects the other integrals, should be even more valid for ligand pre-edge transitions than for LMCT transitions due to the localized nature of the ligand 1s orbital involved in the transition. Including only integrals which involve atomic orbitals on the same ligand center, the ligand-ligand integral can be approximated using equation 5.6.

$$\langle \chi_L|\mathbf{r}(x,y,z)|\chi_L'\rangle = pR\langle s|\mathbf{r}(x',y',z')|p\rangle \quad (5.6)$$

where pR is the projection of the electric dipole vector in the molecular axis system (x, y, z) onto the ligand axis frame (x', y', z') (R is the metal-ligand bond length), χ_L is a symmetry-adapted linear combination of ligand 1s core orbitals, and χ_L' is a symmetry-adapted linear combination of ligand 3p orbitals. The projections, pR, have been determined for this T_d system using the vectors in Figure 5.3 and are given in Table 5.7. Using equations 5.5 and 5.6 and Table 5.7, the solution for each non-zero one-electron matrix element on the left in equation 5.2' is obtained and is given in Table 5.8.

Having obtained the one-electron matrix elements, the value of the one-electron reduced matrix elements ($< a_1 \| t_2 \| t_2 >$, $< t_2 \| t_2 \| t_2 >$, and $< t_2 \| t_2 \| e >$) can be

Table 5.6. Symmetry-adapted One-electron Wavefunctions for a T_d Molecule[a]

Ligand Core 1s Orbitals	SALC's	
a_1	$\frac{1}{2}(s_1 + s_2 + s_3 + s_4)$	
$t_2(x)$	$\frac{1}{2}(s_1 - s_2 + s_3 - s_4)$	
$t_2(y)$	$\frac{1}{2}(s_1 + s_2 - s_3 - s_4)$	
$t_2(z)$	$\frac{1}{2}(s_1 - s_2 - s_3 + s_4)$	
Metal d-type Orbitals	**SALC's**	
	metal component	**ligand component**
$e(\theta)$	$\sqrt{[1 - c_3^2]}\, d_{z^2}$	$+ c_3 [\frac{1}{2}(p_{x'1} - p_{x'2} - p_{x'3} + p_{x'4})]$
$e(\varepsilon)$	$\sqrt{[1 - c_3^2]}\, d_{x^2-y^2}$	$+ c_3 [\frac{1}{2}(p_{y'1} - p_{y'2} - p_{y'3} + p_{y'4})]$
$t_2(x)$	$\sqrt{[1 - (c_1^2 + c_2^2)]}\, d_{yz}$	$+ c_1 [\frac{1}{2}(p_{z'1} - p_{z'2} + p_{z'3} - p_{z'4})] + c_2 [\frac{1}{4}[(p_{x'1} + p_{x'2} - p_{x'3} - p_{x'4}) + \sqrt{3}\,(-p_{y'1} - p_{y'2} + p_{y'3} + p_{y'4})]]$
$t_2(y)$	$\sqrt{[1 - (c_1^2 + c_2^2)]}\, d_{xz}$	$+ c_1 [\frac{1}{2}(p_{z'1} + p_{z'2} - p_{z'3} - p_{z'4})] + c_2 [\frac{1}{4}[(p_{x'1} - p_{x'2} + p_{x'3} - p_{x'4}) + \sqrt{3}\,(p_{y'1} - p_{y'2} + p_{y'3} - p_{y'4})]]$
$t_2(z)$	$\sqrt{[1 - (c_1^2 + c_2^2)]}\, d_{xy}$	$+ c_1 [\frac{1}{2}(p_{z'1} - p_{z'2} - p_{z'3} + p_{z'4})] - c_2 [\frac{1}{2}(p_{x'1} + p_{x'2} + p_{x'3} + p_{x'4})]$

[a] Taken from Ballhausen, C. J.; Gray, H. B. *Molecular Orbital Theory*; Benjamin Press: New York, 1964, pp 108-109.

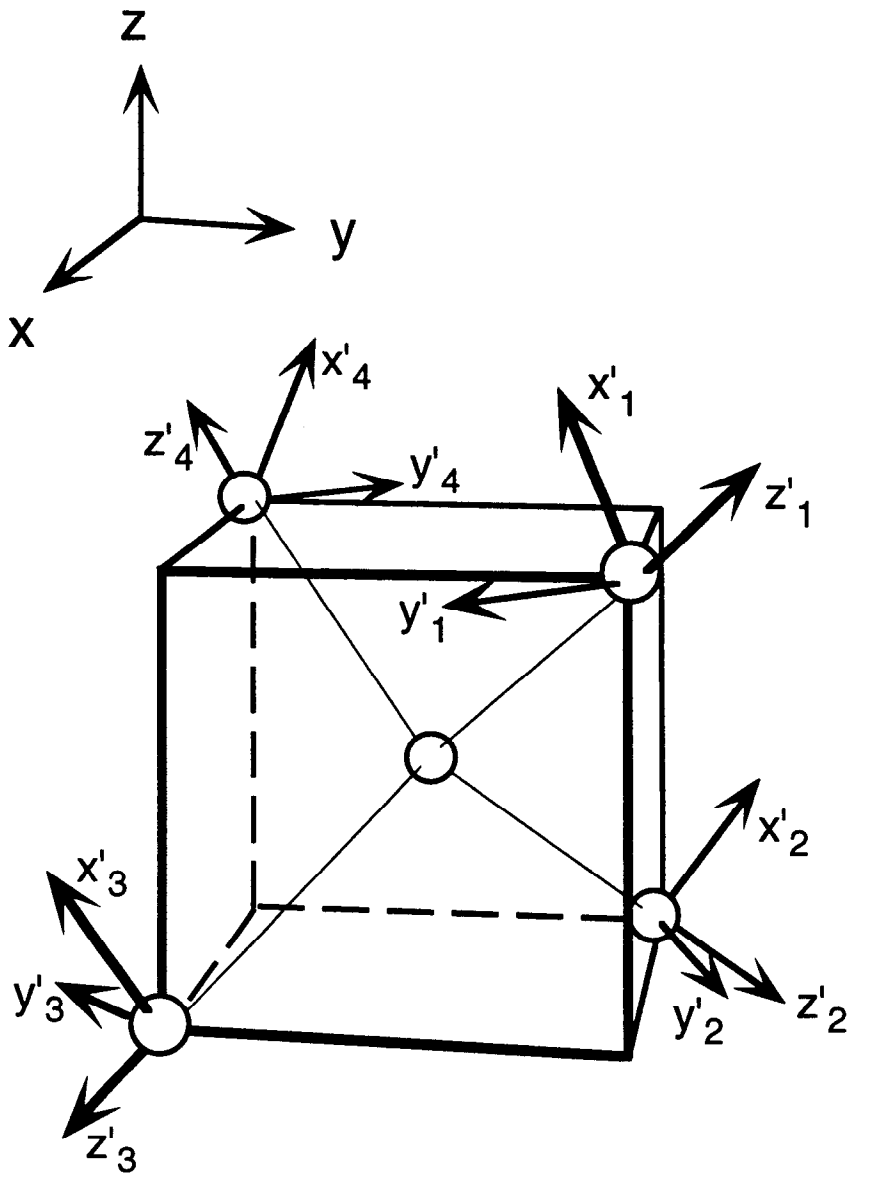

Figure 5.3. The T_d molecular axis system and ligand p-orbital vectors used for molecular orbital construction.[26] The molecular axes are x, y, z, and the local axis system of each ligand is designated with x', y', z'. For each ligand, the z' (σ-bonding) p orbital is along the ligand-metal bond. The π-bonding orbitals are perpendicular to the bond with each y' being 90° to the molecular z-axis. Note that the x' and y' vectors of ligand centers 1 and 4 are related by symmetry as are centers 2 and 3, but the two sets of vectors do not directly transform into one another with point group operations.

Table 5.7. Projections of Molecular Axes onto Cl p-Orbitals in a T_d Molecule[a]

Cl p-orbital	Molecular x	Molecular y	Molecular z
$p_{x'1}$	$-\frac{R}{\sqrt{6}}$	$-\frac{R}{\sqrt{6}}$	$+\frac{R\sqrt{2}}{\sqrt{3}}$
$p_{y'1}$	$+\frac{R}{\sqrt{2}}$	$-\frac{R}{\sqrt{2}}$	0
$p_{z'1}$	$+\frac{R}{\sqrt{3}}$	$+\frac{R}{\sqrt{3}}$	$+\frac{R}{\sqrt{3}}$
$p_{x'2}$	$-\frac{R}{\sqrt{6}}$	$+\frac{R}{\sqrt{6}}$	$+\frac{R\sqrt{2}}{\sqrt{3}}$
$p_{y'2}$	$+\frac{R}{\sqrt{2}}$	$+\frac{R}{\sqrt{2}}$	0
$p_{z'2}$	$-\frac{R}{\sqrt{3}}$	$+\frac{R}{\sqrt{3}}$	$-\frac{R}{\sqrt{3}}$
$p_{x'3}$	$+\frac{R}{\sqrt{6}}$	$-\frac{R}{\sqrt{6}}$	$+\frac{R\sqrt{2}}{\sqrt{3}}$
$p_{y'3}$	$-\frac{R}{\sqrt{2}}$	$-\frac{R}{\sqrt{2}}$	0
$p_{z'3}$	$+\frac{R}{\sqrt{3}}$	$-\frac{R}{\sqrt{3}}$	$-\frac{R}{\sqrt{3}}$
$p_{x'4}$	$+\frac{R}{\sqrt{6}}$	$+\frac{R}{\sqrt{6}}$	$+\frac{R\sqrt{2}}{\sqrt{3}}$
$p_{y'4}$	$-\frac{R}{\sqrt{2}}$	$+\frac{R}{\sqrt{2}}$	0
$p_{z'4}$	$-\frac{R}{\sqrt{3}}$	$-\frac{R}{\sqrt{3}}$	$+\frac{R}{\sqrt{3}}$

[a] Determined using vectors defined in Ballhausen, C. J.; Gray, H. B. *Molecular Orbital Theory*; Benjamin Press: New York, 1964, pp 108-109; see also Figure 5.3.

Table 5.8. Evaluation of One-electron Matrix Elements With Molecular Orbital Expressions

One-electron Matrix Element	Molecular Orbital Substitution[a]
$\langle a_1 \mid t_2(x) \mid t_2(x) \rangle$	$c_1 R \frac{1}{\sqrt{3}} \langle s \mid r(z') \mid p_{z'} \rangle - c_2 R \frac{1}{2\sqrt{6}} \langle s \mid r(x') \mid p_{x'} \rangle - c_2 R \frac{\sqrt{3}}{2\sqrt{2}} \langle s \mid r(y') \mid p_{y'} \rangle$
$\langle a_1 \mid t_2(y) \mid t_2(y) \rangle$	$c_1 R \frac{1}{\sqrt{3}} \langle s \mid r(z') \mid p_{z'} \rangle - c_2 R \frac{1}{2\sqrt{6}} \langle s \mid r(x') \mid p_{x'} \rangle - c_2 R \frac{\sqrt{3}}{2\sqrt{2}} \langle s \mid r(y') \mid p_{y'} \rangle$
$\langle a_1 \mid t_2(z) \mid t_2(z) \rangle$	$c_1 \frac{R}{\sqrt{3}} \langle s \mid r(z') \mid p_{z'} \rangle - c_2 R \frac{\sqrt{2}}{\sqrt{3}} \langle s \mid r(x') \mid p_{x'} \rangle$
$\langle t_2(x) \mid t_2(x) \mid e(\theta) \rangle$	$- c_3 R \frac{1}{\sqrt{6}} \langle s \mid r(x') \mid p_{x'} \rangle$
$\langle t_2(x) \mid t_2(x) \mid e(\varepsilon) \rangle$	$c_3 R \frac{1}{\sqrt{2}} \langle s \mid r(y') \mid p_{y'} \rangle$
$\langle t_2(x) \mid t_2(z) \mid t_2(y) \rangle$	$c_1 \frac{R}{\sqrt{3}} \langle s \mid r(z') \mid p_{z'} \rangle + c_2 R \frac{\sqrt{2}}{2\sqrt{3}} \langle s \mid r(x') \mid p_{x'} \rangle$
$\langle t_2(x) \mid t_2(y) \mid t_2(z) \rangle$	$c_1 \frac{R}{\sqrt{3}} \langle s \mid r(z') \mid p_{z'} \rangle + c_2 R \frac{1}{\sqrt{6}} \langle s \mid r(x') \mid p_{x'} \rangle$
$\langle t_2(y) \mid t_2(y) \mid e(\theta) \rangle$	$- c_3 R \frac{1}{\sqrt{6}} \langle s \mid r(x') \mid p_{x'} \rangle$
$\langle t_2(y) \mid t_2(y) \mid e(\varepsilon) \rangle$	$- c_3 R \frac{1}{\sqrt{2}} \langle s \mid r(y') \mid p_{y'} \rangle$
$\langle t_2(y) \mid t_2(z) \mid t_2(x) \rangle$	$c_1 \frac{R}{\sqrt{3}} \langle s \mid r(z') \mid p_{z'} \rangle + c_2 R \frac{\sqrt{2}}{2\sqrt{3}} \langle s \mid r(x') \mid p_{x'} \rangle$
$\langle t_2(y) \mid t_2(x) \mid t_2(z) \rangle$	$c_2 \frac{R}{\sqrt{3}} \langle s \mid r(z') \mid p_{z'} \rangle + c_2 R \frac{1}{\sqrt{6}} \langle s \mid r(x') \mid p_{x'} \rangle$
$\langle t_2(z) \mid t_2(z) \mid e(\theta) \rangle$	$c_3 R \frac{\sqrt{2}}{\sqrt{3}} \langle s \mid r(x') \mid p_{x'} \rangle$
$\langle t_2(z) \mid t_2(y) \mid t_2(x) \rangle$	$c_1 \frac{R}{\sqrt{3}} \langle s \mid r(z') \mid p_{z'} \rangle - c_2 R \frac{1}{2\sqrt{6}} \langle s \mid r(x') \mid p_{x'} \rangle + c_2 R \frac{\sqrt{3}}{2\sqrt{2}} \langle s \mid r(y') \mid p_{y'} \rangle$
$\langle t_2(z) \mid t_2(x) \mid t_2(y) \rangle$	$c_1 \frac{R}{\sqrt{3}} \langle s \mid r(z') \mid p_{z'} \rangle - c_2 R \frac{1}{2\sqrt{6}} \langle s \mid r(x') \mid p_{x'} \rangle + c_2 R \frac{\sqrt{3}}{2\sqrt{2}} \langle s \mid r(y') \mid p_{y'} \rangle$

[a] Using symmetry-adapted one-electron wavefunctions given in Table 5.6.

determined using equation 5.2' and are given in Table 5.9.[30] Reduced matrix elements involving the t_2-set of orbitals are a sum of $3p_\sigma(p_{z'})$- and $3p_\pi(p_{x'})$-based integrals, while integrals involving the e-set have only $3p_\pi(p_{x'})$-based integrals. Table 5.9 also gives the square of each one-electron reduced matrix element. For transitions to the t_2-set, the square includes cross terms due to the contributions from both σ- and π-based intensity mechanisms.

***(iv)* Calculation of Dipole Strength in the Strong Field Limit.** The dipole strength (equation 5.1) is now evaluated for each pre-edge transition by summing the squares of each matrix element contributing to the transition (see Table 5.5, last column). Table 5.10 gives the dipole strength for each pre-edge transition (with its parent excited state designated in parentheses) in terms of one-electron reduced matrix elements. Also given in Table 5.10 are the equivalent dipole strength expressions derived from substitution of the molecular orbital wavefunctions in Table 5.9.

The electron repulsion between a localized ligand core (1s) hole and electrons in the valence d-manifold should be minimal. Thus, transitions which are related to the same d^{n+1} parent, differing only in the ligand core orbital of origin (a_1 or t_2) are assumed to be degenerate, and contributions from their dipole strengths will be additive. For example, the $^2A_1$ and $^2T_2$ excited states of T_d $CuCl_4^{2-}$ arise from the same parent excited state ($^1A_1$) and thus contribute to pre-edge intensity at the same energy. The expressions for the total sum dipole strength for each d^{n+1} parent excited state are given in Table 5.11. Since the intensity of the pure Cl 1s —> 3p transition to the $3p_{z'}$ orbital is equal in magnitude to those to the $3p_{x'}$ and $3p_{y'}$ orbitals, the following substitutions are made, $\langle s \mid \mathbf{r} \mid p \rangle^2 = \langle s \mid \mathbf{r}(z') \mid p_{z'} \rangle^2 = \langle s \mid \mathbf{r}(x') \mid p_{x'} \rangle^2 = \langle s \mid \mathbf{r}(y') \mid p_{y'} \rangle^2$. Note that when the dipole strengths for each parent excited state are calculated, the σ-π cross terms cancel. Thus, cross terms do not contribute to observed transition intensity. For each Cu(II), Ni(II), and Co(II), in which there is only one parent excited state, the intensity of the transition to each state is proportional to the sum of the σ and π 3p-covalency in the t_2-set $[c_1^2 + c_2^2]$, a constant related to the number of ground state t_2-set holes, the square of the bond length, and the intensity of a pure Cl 1s —> 3p transition ($\langle s \mid \mathbf{r} \mid p \rangle^2$). It should be noted that the result obtained for T_d $CuCl_4^{2-}$ holds even if the symmetry is lowered to D_{2d}.[31] Further, the expression derived for the Cu(II) complex by this methodology is exactly analogous to that given in Chapter 1 (equation 1.3c) for the simple 1s —> ψ^* transition.

For Fe(III)Cl_4^-, there is one parent excited state arising from a transition to the e-set (^5E) and one parent excited state derived from a transition to the t_2-set ($^5T_2$). The dipole strength expression for the transition to the $^5T_2$ parent is identical to that for the

Table 5.9. Conversion from One-electron Reduced Matrix Elements to One-electron Matrix Elements

	Substitution for One-electron Reduced Matrix Elements	Substitution for the Square of One-electron Reduced Matrix Elements
$\langle a_1 \parallel t_2 \parallel t_2 \rangle$	$-c_1R\langle s \mid \mathbf{r}(z') \mid p_{z'} \rangle + \sqrt{2}\, c_2R \langle s \mid \mathbf{r}(x') \mid p_{x'} \rangle$	
$\langle a_1 \parallel t_2 \parallel t_2 \rangle^2$		$c_1^2R^2 \langle s \mid \mathbf{r}(z') \mid p_{z'} \rangle^2 + 2c_2^2R^2 \langle s \mid \mathbf{r}(x') \mid p_{x'} \rangle^2$ $- 2\sqrt{2}c_1c_2R^2 \langle s \mid \mathbf{r}(z') \mid p_{z'} \rangle\langle s \mid \mathbf{r}(x') \mid p_{x'} \rangle$
$\langle t_2 \parallel t_2 \parallel t_2 \rangle$	$-\sqrt{2}\, c_1R \langle s \mid \mathbf{r}(z') \mid p_{z'} \rangle - c_2R \langle s \mid \mathbf{r}(x') \mid p_{x'} \rangle$	
$\langle t_2 \parallel t_2 \parallel t_2 \rangle^2$		$2c_1^2R^2 \langle s \mid \mathbf{r}(z') \mid p_{z'} \rangle^2 + c_2^2R^2 \langle s \mid \mathbf{r}(x') \mid p_{x'} \rangle^2$ $+ 2\sqrt{2}c_1c_2R^2 \langle s \mid \mathbf{r}(z') \mid p_{z'} \rangle\langle s \mid \mathbf{r}(x') \mid p_{x'} \rangle$
$\langle t_2 \parallel t_2 \parallel e \rangle$	$\sqrt{2}\, c_3R \langle s \mid \mathbf{r}(x') \mid p_{x'} \rangle$	
$\langle t_2 \parallel t_2 \parallel e \rangle^2$		$2c_3^2R^2 \langle s \mid \mathbf{r}(x') \mid p_{x'} \rangle^2$

Table 5.10. Dipole Strength for Each Contributing Pre-edge Transition for MCl_4^{n-} (d^1-d^5 holes)

	Dipole Strength in Terms of	
Transition	one-electron reduced matrix elements	molecular orbital expressions
$CuCl_4^{2-}$ $^2T_2$ (GS)		
$\longrightarrow (^1A_1)\ ^2A_1$ ($a_1 \longrightarrow t_2$)	$\frac{1}{9} < a_1 \parallel t_2 \parallel t_2 >^2$	$\frac{1}{9}[c_1^2R^2 <s \mid \mathbf{r}(z') \mid p_{z'}>^2 + 2c_2^2R^2 <s \mid \mathbf{r}(x') \mid p_{x'}>^2 - 2\sqrt{2}c_1c_2R^2 <s \mid \mathbf{r}(z') \mid p_{z'}><s \mid \mathbf{r}(x') \mid p_{x'}>]$
$\longrightarrow (^1A_1)\ ^2T_2$ ($t_2 \longrightarrow t_2$)	$\frac{1}{9} < t_2 \parallel t_2 \parallel t_2 >^2$	$\frac{1}{9}[2c_1^2R^2 <s \mid \mathbf{r}(z') \mid p_{z'}>^2 + c_2^2R^2 <s \mid \mathbf{r}(x') \mid p_{x'}>^2 + 2\sqrt{2}c_1c_2R^2 <s \mid \mathbf{r}(z') \mid p_{z'}><s \mid \mathbf{r}(x') \mid p_{x'}>]$
$NiCl_4^{2-}$ $^3T_1$ (GS)		
$\longrightarrow (^2T_2)\ ^3T_2$ ($a_1 \longrightarrow t_2$)	$\frac{2}{9} < a_1 \parallel t_2 \parallel t_2 >^2$	$\frac{2}{9}[c_1^2R^2 <s \mid \mathbf{r}(z') \mid p_{z'}>^2 + 2c_2^2R^2 <s \mid \mathbf{r}(x') \mid p_{x'}>^2 - 2\sqrt{2}c_1c_2R^2 <s \mid \mathbf{r}(z') \mid p_{z'}><s \mid \mathbf{r}(x') \mid p_{x'}>]$
$\longrightarrow (^2T_2)\ ^3E$ ($t_2 \longrightarrow t_2$)	$\frac{1}{9} < t_2 \parallel t_2 \parallel t_2 >^2$	$\frac{1}{9}[2c_1^2R^2 <s \mid \mathbf{r}(z') \mid p_{z'}>^2 + c_2^2R^2 <s \mid \mathbf{r}(x') \mid p_{x'}>^2 + 2\sqrt{2}c_1c_2R^2 <s \mid \mathbf{r}(z') \mid p_{z'}><s \mid \mathbf{r}(x') \mid p_{x'}>]$
$\longrightarrow (^2T_2)\ ^3T_1$ ($t_2 \longrightarrow t_2$)	$\frac{1}{18} < t_2 \parallel t_2 \parallel t_2 >^2$	$\frac{1}{18}[2c_1^2R^2 <s \mid \mathbf{r}(z') \mid p_{z'}>^2 + c_2^2R^2 <s \mid \mathbf{r}(x') \mid p_{x'}>^2 + 2\sqrt{2}c_1c_2R^2 <s \mid \mathbf{r}(z') \mid p_{z'}><s \mid \mathbf{r}(x') \mid p_{x'}>]$
$\longrightarrow (^2T_2)\ ^3T_2$ ($t_2 \longrightarrow t_2$)	$\frac{1}{18} < t_2 \parallel t_2 \parallel t_2 >^2$	$\frac{1}{18}[2c_1^2R^2 <s \mid \mathbf{r}(z') \mid p_{z'}>^2 + c_2^2R^2 <s \mid \mathbf{r}(x') \mid p_{x'}>^2 + 2\sqrt{2}c_1c_2R^2 <s \mid \mathbf{r}(z') \mid p_{z'}><s \mid \mathbf{r}(x') \mid p_{x'}>]$
$CoCl_4^{2-}$ $^4A_2$ (GS)		
$\longrightarrow (^3T_1)\ ^4T_1$ ($a_1 \longrightarrow t_2$)	$\frac{1}{3} < a_1 \parallel t_2 \parallel t_2 >^2$	$\frac{1}{3}[c_1^2R^2 <s \mid \mathbf{r}(z') \mid p_{z'}>^2 + 2c_2^2R^2 <s \mid \mathbf{r}(x') \mid p_{x'}>^2 - 2\sqrt{2}c_1c_2R^2 <s \mid \mathbf{r}(z') \mid p_{z'}><s \mid \mathbf{r}(x') \mid p_{x'}>]$
$\longrightarrow (^3T_1)\ ^4T_1$ ($t_2 \longrightarrow t_2$)	$\frac{1}{3} < t_2 \parallel t_2 \parallel t_2 >^2$	$\frac{1}{3}[2c_1^2R^2 <s \mid \mathbf{r}(z') \mid p_{z'}>^2 + c_2^2R^2 <s \mid \mathbf{r}(x') \mid p_{x'}>^2 + 2\sqrt{2}c_1c_2R^2 <s \mid \mathbf{r}(z') \mid p_{z'}><s \mid \mathbf{r}(x') \mid p_{x'}>]$

Table 10. Dipole Strength (Continued)

Transition	Dipole Strength in Terms of one-electron reduced matrix elements	molecular orbital expressions
$Fe(II)Cl_4^{2-}$ ^5E (GS)		
$\longrightarrow (^4A_2)\ ^5T_1$ $(t_2 \longrightarrow e)$	$\frac{1}{6} < t_2 \| t_2 \| e >^2$	$\frac{1}{6}[2c_3^2R^2 <s \mid \mathbf{r}(x') \mid p_{x'}>^2]$
$\longrightarrow (^4T_2)\ ^5T_2$ $(a_1 \longrightarrow t_2)$	$\frac{1}{6} < a_1 \| t_2 \| t_2 >^2$	$\frac{1}{6}[c_1^2R^2 <s \mid \mathbf{r}(z') \mid p_{z'}>^2 + 2c_2^2R^2 <s \mid \mathbf{r}(x') \mid p_{x'}>^2 - 2\sqrt{2}c_1c_2R^2 <s \mid \mathbf{r}(z') \mid p_{z'}><s \mid \mathbf{r}(x') \mid p_{x'}>]$
$\longrightarrow (^4T_2)\ ^5T_1$ $(t_2 \longrightarrow t_2)$	0	
$\longrightarrow (^4T_2)\ ^5T_2$ $(t_2 \longrightarrow t_2)$	$\frac{1}{6} < t_2 \| t_2 \| t_2 >^2$	$\frac{1}{6}[2c_1^2R^2 <s \mid \mathbf{r}(z') \mid p_{z'}>^2 + c_2^2R^2 <s \mid \mathbf{r}(x') \mid p_{x'}>^2 + 2\sqrt{2}c_1c_2R^2 <s \mid \mathbf{r}(z') \mid p_{z'}><s \mid \mathbf{r}(x') \mid p_{x'}>]$
$\longrightarrow (^4T_1)\ ^5T_1$ $(a_1 \longrightarrow t_2)$	$\frac{1}{6} < a_1 \| t_2 \| t_2 >^2$	$\frac{1}{6}[c_1^2R^2 <s \mid \mathbf{r}(z') \mid p_{z'}>^2 + 2c_2^2R^2 <s \mid \mathbf{r}(x') \mid p_{x'}>^2 - 2\sqrt{2}c_1c_2R^2 <s \mid \mathbf{r}(z') \mid p_{z'}><s \mid \mathbf{r}(x') \mid p_{x'}>]$
$\longrightarrow (^4T_1)\ ^5T_1$ $(t_2 \longrightarrow t_2)$	$\frac{1}{6} < t_2 \| t_2 \| t_2 >^2$	$\frac{1}{6}[2c_1^2R^2 <s \mid \mathbf{r}(z') \mid p_{z'}>^2 + c_2^2R^2 <s \mid \mathbf{r}(x') \mid p_{x'}>^2 + 2\sqrt{2}c_1c_2R^2 <s \mid \mathbf{r}(z') \mid p_{z'}><s \mid \mathbf{r}(x') \mid p_{x'}>]$
$\longrightarrow (^4T_1)\ ^5T_2$ $(t_2 \longrightarrow t_2)$	0	
$Fe(III)Cl_4^-$ $^6A_1$ (GS)		
$\longrightarrow (^5E)\ ^6T_2$ $(t_2 \longrightarrow e)$	$\frac{1}{3} < t_2 \| t_2 \| e >^2$	$\frac{1}{3}[2c_3^2R^2 <s \mid \mathbf{r}(x') \mid p_{x'}>^2]$
$\longrightarrow (^5T_2)\ ^6T_2$ $(a_1 \longrightarrow t_2)$	$\frac{1}{3} < a_1 \| t_2 \| t_2 >^2$	$\frac{1}{3}[c_1^2R^2 <s \mid \mathbf{r}(z') \mid p_{z'}>^2 + 2c_2^2R^2 <s \mid \mathbf{r}(x') \mid p_{x'}>^2 - 2\sqrt{2}c_1c_2R^2 <s \mid \mathbf{r}(z') \mid p_{z'}><s \mid \mathbf{r}(x') \mid p_{x'}>]$
$\longrightarrow (^5T_2)\ ^6T_2$ $(t_2 \longrightarrow t_2)$	$\frac{1}{3} < t_2 \| t_2 \| t_2 >^2$	$\frac{1}{3}[2c_1^2R^2 <s \mid \mathbf{r}(z') \mid p_{z'}>^2 + c_2^2R^2 <s \mid \mathbf{r}(x') \mid p_{x'}>^2 + 2\sqrt{2}c_1c_2R^2 <s \mid \mathbf{r}(z') \mid p_{z'}><s \mid \mathbf{r}(x') \mid p_{x'}>]$

Table 5.11. Strong Field Dipole Strength Expressions for MCl_4^{n-} Pre-edge Transition Intensities

Complex	Parent d^{n+1} Excited State	Dipole Strength for Transition to Parent Excited State
$CuCl_4^{2-}$	$^1A_1$	$\frac{1}{3}(c_1^2 + c_2^2) R^2 \langle s \mid \mathbf{r} \mid p \rangle^2$
$NiCl_4^{2-}$	$^2T_2$	$\frac{2}{3}(c_1^2 + c_2^2) R^2 \langle s \mid \mathbf{r} \mid p \rangle^2$
$CoCl_4^{2-}$	$^3T_1$	$(c_1^2 + c_2^2) R^2 \langle s \mid \mathbf{r} \mid p \rangle^2$
$Fe(II)Cl_4^{2-}$	$^4A_2$	$\frac{1}{3} c_3^2 R^2 \langle s \mid \mathbf{r} \mid p \rangle^2$
	$^4T_2$	$\frac{1}{2}(c_1^2 + c_2^2) R^2 \langle s \mid \mathbf{r} \mid p \rangle^2$
	$^4T_1$	$\frac{1}{2}(c_1^2 + c_2^2) R^2 \langle s \mid \mathbf{r} \mid p \rangle^2$
$Fe(III)Cl_4^-$	^5E	$\frac{2}{3} c_3^2 R^2 \langle s \mid \mathbf{r} \mid p \rangle^2$
	$^5T_2$	$(c_1^2 + c_2^2) R^2 \langle s \mid \mathbf{r} \mid p \rangle^2$

single Co(II) excited state parent because both metal sites have the same ground state t_2 configurations. The intensity of the transition to the ^5E parent excited state is proportional to the π 3p-covalency $[c_3^2]$ in the e-set, a constant related to the number of ground state e-set holes, R^2 and $<s|r|p>^2$.

For $Fe(II)Cl_4^{2-}$, there is one parent excited state arising from a transition to the e-set ($^4A_2$) and two parent excited states derived from a transition to the t_2-set ($^4T_2$ + $^4T_1$). The dipole strengths of the pre-edge transitions to the $^4T_2$ and $^4T_1$ parents are equal and each is half the value calculated for $CoCl_4^{2-}$. Thus, for transitions to the t_2-set, $Fe(II)Cl_4^{2-}$ has the same total dipole strength as $CoCl_4^{2-}$ because Co(II) and Fe(II) have the same t_2 ground configuration. However, the intensity in $Fe(II)Cl_4^{2-}$ is distributed equally over two excited states. The intensity of the transition to the $^4A_2$ parent in $Fe(II)Cl_4^{2-}$ is related to that for the ^5E parent in Fe(III), with the difference reflecting the fact that Fe(II) has one less e-hole in the ground state.

5.4.2.3. Higher State Mixing and Excited State Energies in Intermediate-Strength Ligand Fields. The analysis of pre-edge intensities has up to this point treated the transitions in the strong field limit. For a T_d complex with chloride ligands, however, the treatment must be extended to account for the fact these complexes are closer to the weak field limit. In intermediate-strength ligand fields, mixing between states of appropriate symmetry is non-negligible. Mixing of a pre-edge transition parent excited state with a higher lying d^{n+1} excited state will result in the redistribution of pre-edge intensity to higher energy. The consequence of this mixing would then be a reduction in the experimentally observed pre-edge intensity.

Both Co(II) and Fe(II) have d^{n+1} parent excited states which can mix with higher lying states of appropriate symmetry. These higher lying excited states derive from formally forbidden two electron excitations. This mixing will redistribute some of the intensity predicted by the strong field dipole strength for the transition to the allowed d^{n+1} parent (Table 5.11) to higher energy (relative to the pre-edge transition in Figure 5.1). The magnitude of this mixing is determined from the d^{n+1} Tanabe-Sugano matrices[32] for Co(II) and Fe(II), assuming reasonable values of Dq and B for the d^{n+1} excited states. As described in Section 5.4.1., the excited state Dq is expected to be approximately 60% of the ground state value. Appropriate values of B are obtained from values for F_2 determined for the d^{n+1} free ions Co(I) and Fe(I)[33] and using $F_4 = 0.07F_2$ and $B = F_2 - 5F_4$. Table 5.12 gives excited state values of Dq and B, as well as the coefficients of mixing calculated from the Tanabe-Sugano matrices, and the absolute and relative energy splittings of excited states for T_d $Co(II)Cl_4^{2-}$ and $Fe(II)Cl_4^{2-}$. Because the magnitude of B might be expected to be further reduced due to covalency, the B values in

Table 5.12. Distribution of Energies and Intensities for Final States of MCl_4^{n-} Pre-edge Transitions

T_d Metal Ion[a]	Parent d^{n+1} Excited State	Higher State of Appropriate Symmetry for Mixing	Excited State D_q (cm^{-1})	Excited State B (cm^{-1})	Calculated Energy Value[b] (cm^{-1})	Relative Energy Value (eV)	Coeff. of Mixing[b]	Ratios from Strong Field D_o[c]	Theoretical Intensity Ratios[d]
Co(II)	$^3T_1$[a]		186	812	-6165.5	0	0.84	1	1
		$^3T_1$[b]			+7213.5	1.66	0.16	1	0.19
Fe(II)	$^4A_2$	-	250	722	-13830.0	-0.31	-	$\frac{1}{3}c_3^2$	0.42
	$^4T_2$	-			-11330.0	0	-	$\frac{1}{2}(c_1^2 + c_2^2)$	1
	$^4T_1$[a]				-9436.0	0.23	0.29	$\frac{1}{2}(c_1^2 + c_2^2)$	0.29
		$^4T_1$[b]			+106.0	1.42	0.71		0.71
Fe(III)	^5E	-	393			0	-	$\frac{2}{3}c_3^2$	0.58
	$^5T_2$	-				0.49	-	$(c_1^2 + c_2^2)$	1

[a] Cu and Ni are not included here because there is only one parent excited state in each case and thus there is no splitting to be calculated.

[b] Calculated using Tanabe-Sugano matrices.[32]

[c] See Table 5.11.

[d] The ratios between transitions to t_2 orbitals are completely determined from the calculated D_o expressions and the calculated coefficients of mixing. The ratios between transitions to t_2 and e orbitals have been estimated using c_3^2 and $(c_1^2 + c_2^2)$ from Xα calculations (see text).

Table 5.12 should be taken as an upper limit. For smaller B, there would be less mixing between the two states and a smaller energy splitting.

For $Co(II)Cl_4^{2-}$, the pre-edge intensity for the transition to the allowed $^3T_1{}^a$ parent excited state will contain ~84% of the predicted strong field intensity. The remaining ~16% is predicted to be redistributed to ~1.66 eV higher energy (for the formally forbidden transition to $^3T_1{}^b$).

There are three allowed excited state parents in T_d Fe(II), only one of which ($^4T_1$) experiences higher state mixing. The allowed parent excited state is denoted $^4T_1{}^a$, and the higher lying forbidden state is $^4T_1{}^b$. Evaluation of the Tanabe-Sugano matrices indicates that the majority (~71%) of the intensity predicted for the $^4T_1{}^a$ parent final state (see Table 5.11) is actually redistributed to ~1.19 eV higher energy (relative to the allowed $^4T_1{}^a$ state). To define the distribution of intensity for all T_d Fe(II) pre-edge transitions, the ratios between the dipole strengths of each transition can be employed (see Table 5.11). These ratios (given in Table 5.12), combined with the coefficients of excited state mixing, can be used to calculate the pre-edge transition intensity ratios. For transitions to the excited state parents $^4T_2$ and $^4T_1{}^a$, the $^4T_2$:$^4T_1{}^a$ intensity ratio is 1:0.29 and the excited states are separated by 0.23 eV. The higher lying (forbidden) $^4T_1{}^b$ state has an intensity of 0.71 relative to $^4T_2$. The relative contribution of the transition to the e-set of Fe(II) (the $^4A_2$ parent) requires an estimate of the ratio between the π-covalency [c_3^2] in the e-set and the total ($\sigma + \pi = [c_1^2 + c_2^2]$) covalency of the t_2-set. This ratio can be estimated from an Xα calculation of $Fe(II)Cl_4^{2-}$ (*vide infra*) which indicates that c_3^2:$[c_1^2 + c_2^2] \sim 0.64:1$. The total intensity ratio between transitions to $^4A_2$ and $^4T_2$ is then predicted to be 0.42:1, with an energy splitting of 0.31 eV. These results are summarized in Table 5.12.

While T_d $Fe(III)Cl_4^-$ has no intermediate-strength ligand field mixing, the transition intensity ratio between transitions to the e- and t_2-sets (^5E and $^5T_2$ parents, respectively) can be similarly determined. The ratio between the e-set π-covalency [c_3^2] and the t_2-set covalency [$c_1^2 + c_2^2$] is determined from an Xα calculation (*vide infra*) to be c_3^2:$[c_1^2 + c_2^2] \sim 0.86:1$. The combination of this ratio and the intensity ratios predicted by the dipole strength expressions (Table 5.11) give the pre-edge transition intensity ratio for $Fe(III)Cl_4^-$ to be ^5E:$^5T_2 \sim 0.58:1$. The energy splitting between these two parent states is equal to the excited state 10Dq and is determined to be 0.49 eV.

5.4.2.4. Determination of Total Experimental Pre-edge Intensity and Calculation of Covalency. Based on the intensity ratios and energy splittings derived in the previous section (see Table 5.12), each pre-edge feature has been broken down into its contributing transitions. Figures 5.4a-e show the experimental data with the contributing

pre-edge transitions and their assignments. The transitions are fixed to have the appropriate theoretical intensity ratios and energy splittings.

The strong field dipole strength expressions derived above and given in Table 5.11 describe the *total* multiplet transition intensity. For $CuCl_4^{2-}$ (Figure 5.4a) and $NiCl_4^{2-}$ (Figure 5.4b) a single transition contributes to the pre-edge, and the total pre-edge transition intensity is that observed in the Results (Section 5.3) and given in Table 5.2. For $CoCl_4^{2-}$ (Figure 5.4c), the intensity under the pre-edge feature is *not* the total multiplet transition intensity. Rather, the total intensity includes the contribution which has been redistributed to higher energy due to mixing in an intermediate-strength ligand field. Thus, the pre-edge feature reflects ~84% of the total (see Table 5.12) and the total experimental estimate of multiplet intensity is obtained by multiplying the observed pre-edge intensity by $\frac{1}{0.84}$.

The two transitions which contribute to the pre-edge feature in $Fe(III)Cl_4^-$ are unresolved but the feature is broadened[34] (Figure 5.4e). The intensities of the two transitions (with fixed energy splittings and intensity ratios) were modeled with a number of different rising edge backgrounds. In each case the sum of the intensities of the two transitions was within the error reported for the intensity of the feature obtained from a one-function fit which was reported in the Results (Section 5.3) and given in Table 5.2.

For $Fe(II)Cl_4^{2-}$ (Figure 5.4d), the observed pre-edge intensity is the sum of transitions to the $^4A_2$, $^4T_2$, and $^4T_1$ parents. The total multiplet intensity must also include the contribution which has been redistributed to higher energy ($^4T_1{}^b$) due to mixing in an intermediate-strength ligand field. The sum of the $^4A_2$, $^4T_2$, and $^4T_1{}^a$ transitions (i.e., the pre-edge peak intensity), compared to the intensity redistributed to the higher lying $^5E \longrightarrow {}^4T_1{}^b$ transition, gives a theoretical ratio of 1:0.415. The observed pre-edge feature intensity, then, reflects only 70.7% of the total multiplet intensity. As for $Fe(III)Cl_4^-$, the sum of the intensities from the transitions which contribute to the pre-edge feature is adequately described by the intensity of the pre-edge feature obtained from a one-function fit (Table 5.2). Thus, the total multiplet intensity is determined by multiplying the observed pre-edge intensity (Table 5.2) by $\frac{1}{0.707}$. The total multiplet intensity (the sum of all contributing transitions) for each complex is given in Table 5.13.

The dipole strength expressions in Table 5.11 can now be applied to the total multiplet intensity to obtain a quantitative estimate of the covalency in each system. Dipole strength is usually equated with absolute, rather than normalized, intensity. To verify that the dipole strength can be applied directly to the data normalized to the edge jump intensity, we have calculated the dipole strength for the edge jump, modeled as a Cl 1s —> 4p transition. The dipole strength was determined to be the same for each

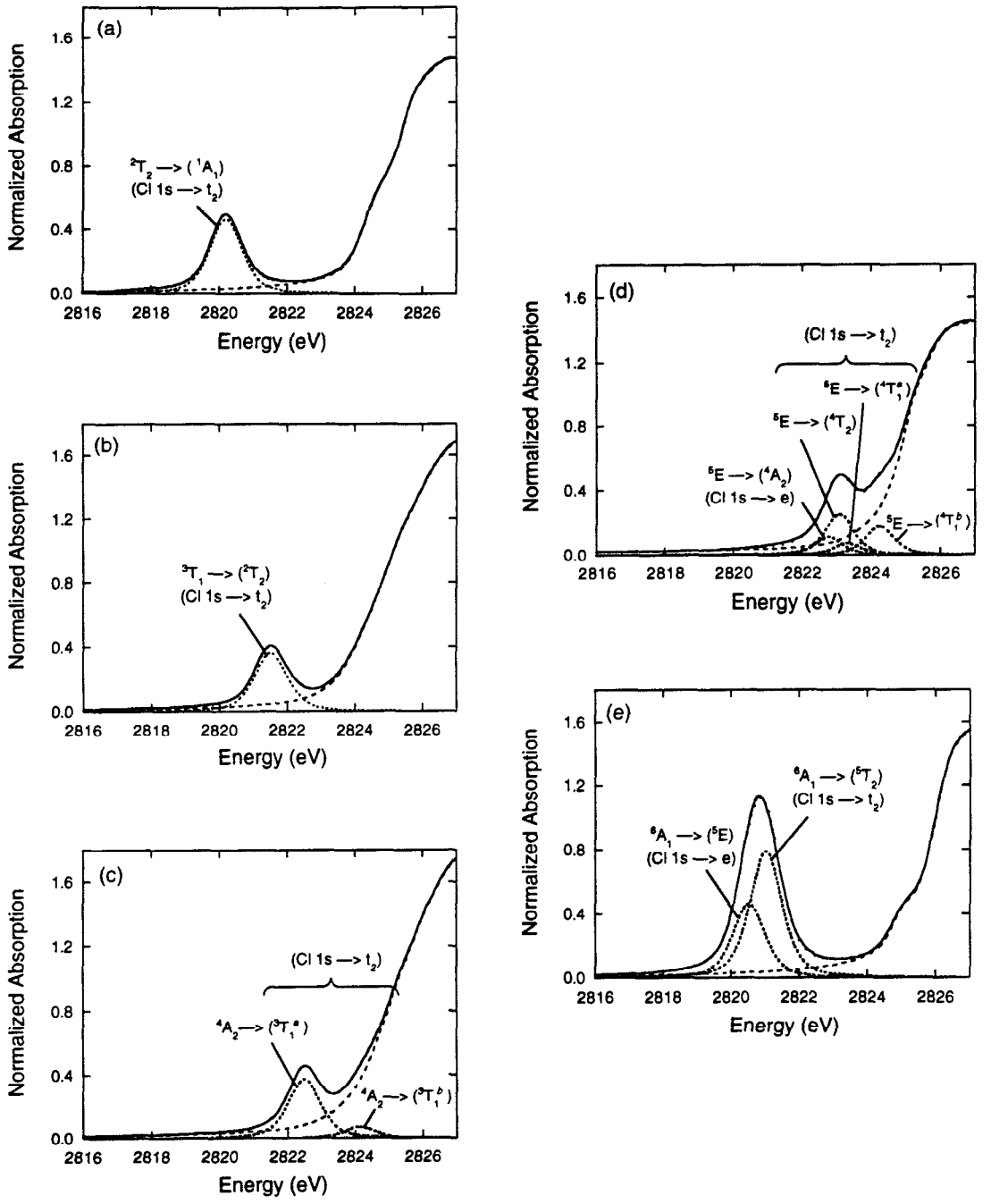

Figure 5.4. Pre-edge transition assignments for (a) $CuCl_4^{2-}$, (b) $NiCl_4^{2-}$, (c) $CoCl_4^{2-}$, (d) $Fe(II)Cl_4^{2-}$, and (e) $Fe(III)Cl_4^{-}$. Transitions are fixed to theoretical intensity ratios and energy splittings (Table 5.12) and are designated by the ground state of each system and the parent d^{n+1} metal excited state to which the transition occurs. States designated with a "*b*" derive intensity from intermediate-strength ligand field mixing.

Table 5.13. Covalency Analysis of Pre-edge Intensities in MCl_4^{n-} Cl K-edges

Complex	Observed Pre-edge Intensity	Factor for Intensity Distributed to Higher Energy	Total Multiplet Intensity	Covalency Reflected in Dipole Strength (%)
$CuCl_4^{2-}$	0.526±0.017		0.526±0.017	$c_1^2 + c_2^2 =$ 30.0±1.4
$NiCl_4^{2-}$	0.428±0.018		0.428±0.018	$c_1^2 + c_2^2 =$ 11.8±0.6
$CoCl_4^{2-}$	0.419±0.021	$\frac{1}{0.84}$	0.497±0.025	$c_1^2 + c_2^2 =$ 9.0±0.5
$Fe(II)Cl_4^{2-}$	0.427±0.039	$\frac{1}{0.707}$	0.662±0.061	$c_1^2 + c_2^2 + \frac{1}{3}c_3^2 =$ 11.9±1.2
$Fe(III)Cl_4^-$	1.505±0.064		1.505±0.064	$c_1^2 + c_2^2 + \frac{2}{3}c_3^2 =$ 29.8±1.6

molecule.[35] Since each normalized edge jump has an intensity of 1.0, the pre-edge intensity dipole strength expressions (Table 5.11) can reliably be applied to the normalized data.

It is well-established that the Cl contribution to the HOMO in D_{2d} $CuCl_4^{2-}$ is ~30%.[36] By equating the dipole strength expression for $CuCl_4^{2-}$ in Table 5.11 to the total pre-edge intensity of the complex in Figure 5.1b and letting the total ($\sigma + \pi$) chloride character be 30% ($[c_1^2 + c_2^2] = 0.30$), the value of the Cl 1s —> 3p transition intensity ($< s \mid \mathbf{r} \mid p >^2$) can be estimated. This value of $< s \mid \mathbf{r} \mid p >^2$ can be substituted into the dipole strength expressions for the remaining complexes and the covalency of each can be obtained from the pre-edge intensity. Because the transitions to the parent excited states in $Fe(II)Cl_4^{2-}$ and $Fe(III)Cl_4^-$ are not experimentally resolved, the total pre-edge intensity must be equated with the sum of the dipole strength for all contributing transitions (Table 5.11). For $Fe(II)Cl_4^{2-}$, $D_o(\text{total}) = (c_1^2 + c_2^2 + \frac{1}{3} c_3^2)\, R^2 < s \mid \mathbf{r} \mid p >^2$ and for $Fe(III)Cl_4^-$, $D_o(\text{total}) = (c_1^2 + c_2^2 + \frac{2}{3} c_3^2)\, R^2 < s \mid \mathbf{r} \mid p >^2$.

The Cl $\pi + \sigma$ covalency $[c_1^2 + c_2^2]$ in the t_2-set in $NiCl_4^{2-}$ and $CoCl_4^{2-}$ is calculated to be (11.8±0.6)% and (9.0±0.5)%, respectively, indicating a reduction in covalency relative to $CuCl_4^{2-}$.

For $Fe(II)Cl_4^{2-}$, the covalency derived from the pre-edge intensity is the total Cl 3p character ($\pi + \sigma$) in the t_2-set plus one-third of the 3p (π) character in the e-set $[c_1^2 + c_2^2 + \frac{1}{3} c_3^2]$ and is determined to be (11.9±1.2)%.

The covalency determined for $Fe(III)Cl_4^-$ is (29.8±1.6)% which corresponds to the total Cl 3p character ($\pi + \sigma$) in the t_2 set plus two-thirds of the 3p (π) character in the e-set $[c_1^2 + c_2^2 + \frac{2}{3} c_3^2]$. These results are summarized in Table 5.13.

In this analysis the value of the Cl 1s —> 3p transition intensity ($< s \mid \mathbf{r} \mid p >^2$) has been assumed to be constant over the MCl_4^{n-} complexes. In fact, this intensity should be somewhat dependent on the charge on the chloride. As was shown in the Section 5.4.1. (Table 5.3), the charge on the chloride varies in these complexes by as much as one-third of a charge unit. To ascertain the relationship between the Cl 1s —> 3p transition intensity and the Cl charge, the relative oscillator strength of the transitions has been estimated using hydrogenic wavefunctions. The result is proportional to the effective charge (Z_{eff}) in both the Cl 1s and Cl 3p orbitals. The proportionality relationship is given in equation 5.7.

$$\langle s \mid \mathbf{r} \mid p \rangle^2 \;\alpha\; \frac{\left(Z_{eff}(s)\right)^{3/2}\left(Z_{eff}(p)\right)^{5/2}\left(Z_{eff}(p) + 2Z_{eff}(s)\right)}{\left(Z_{eff}(p) + Z_{eff}(s)\right)^6} \qquad (5.7)$$

The values of $Z_{eff}(s)$ and $Z_{eff}(p)$ can be estimated using Slater's rules[37] and are calculated using the experimentally determined charges (Table 3) to be $Z_{eff}(s)$ = 16.7 and $Z_{eff}(p)$ = 5.56, 5.52, and 5.63 for Cl bound to Cu(II), Ni(II), and Fe(III), respectively; the $Z_{eff}(p)$ for Cl bound to Co(II) and Fe(II) are equal to that of Cl bound to Ni(II). Figure 5.5 shows the relationship between the Cl 1s —> 3p oscillator strength and $Z_{eff}(p)$, with $Z_{eff}(s)$ fixed at 16.7. In the range of $Z_{eff}(p)$ for these complexes, the relationship is nearly linear. While there is clearly an increase in Cl 1s —> 3p intensity with increasing $Z_{eff}(p)$ due to the 3p orbital contraction, the absolute change is not very large. These results predict that Cl bound to Ni(II) should be characterized by a $< s \mid \mathbf{r} \mid p >^2$ value ~2% less intense than that for Cl bound to Cu(II). Between Fe(II)Cl_4^{2-} and Fe(III)Cl_4^-, an increase in Cl 1s —> 3p intensity of ~5% is predicted. Since the effect is small, it is reasonable to assume an approximately constant value of $< s \mid \mathbf{r} \mid p >^2$ as in the above analysis.

5.4.2.5. MCl_4^{n-} Xα Calculations: Comparison to Experimental Results. Xα calculations have been performed on D_{2d} $CuCl_4^{2-}$ and T_d MCl_4^{n-} (M = Ni(II), Co(II), Fe(II) and Fe(III)) for comparison to the results of the experimental covalency analysis. The results of these calculations are summarized in Table 5.14. Tables which detail orbital energies as well as the calculated valence orbital components for these complexes are provided as supplementary material in the appendix to this chapter.

The total Cl-character in the t_2-set of orbitals varies from 30% in $CuCl_4^{2-}$ to 15% in Fe(II)Cl_4^{2-}; in Fe(III)Cl_4^- it is 26%. Further, the Cl 3p component of this covalency, which contributes to the electric dipole intensity of Cl K-edge transitions, varies across the series from 95% in $CuCl_4^{2-}$ to 68% in Fe(II)Cl_4^{2-}; for Fe(III)Cl_4^- the Cl 3p component is 86%. Thus, the Cl 3p character in each t_2-set (corresponding to $[c_1^2 + c_2^2]$ in the above analysis) varies from ~28% in $CuCl_4^{2-}$ to ~10% in Fe(II)Cl_4^{2-} and is ~22% in Fe(III)Cl_4^-. The results indicate a trend in Cl 3p-covalency over the divalent metal series which is correlated with decreasing effective charge on the metal in going from Cu(II) to Fe(II).

The Cl-character in the e-set of Fe(II)Cl_4^{2-} and Fe(III)Cl_4^- can be similarly examined. The total e-set Cl-character is 10% in Fe(II)Cl_4^{2-} and 23% in Fe(III)Cl_4^-. Of the total Cl character in the e-set of Fe(II)Cl_4^{2-}, 65% is Cl 3p (π). Thus, the total Cl 3p (π) contribution (corresponding to c_3^2) is found to be ~6%. In Fe(III)Cl_4^- 84% of the total Cl-character in the e-set is Cl 3p (π). Thus, the total Cl 3p (π) contribution is ~19% (see Table 5.14). The increase in both t_2 and e covalency in Fe(III)Cl_4^- relative to Fe(II)Cl_4^{2-} is related to the change in oxidation state as well as the concomitant shorter ligand-metal bond length (see Table 5.1).

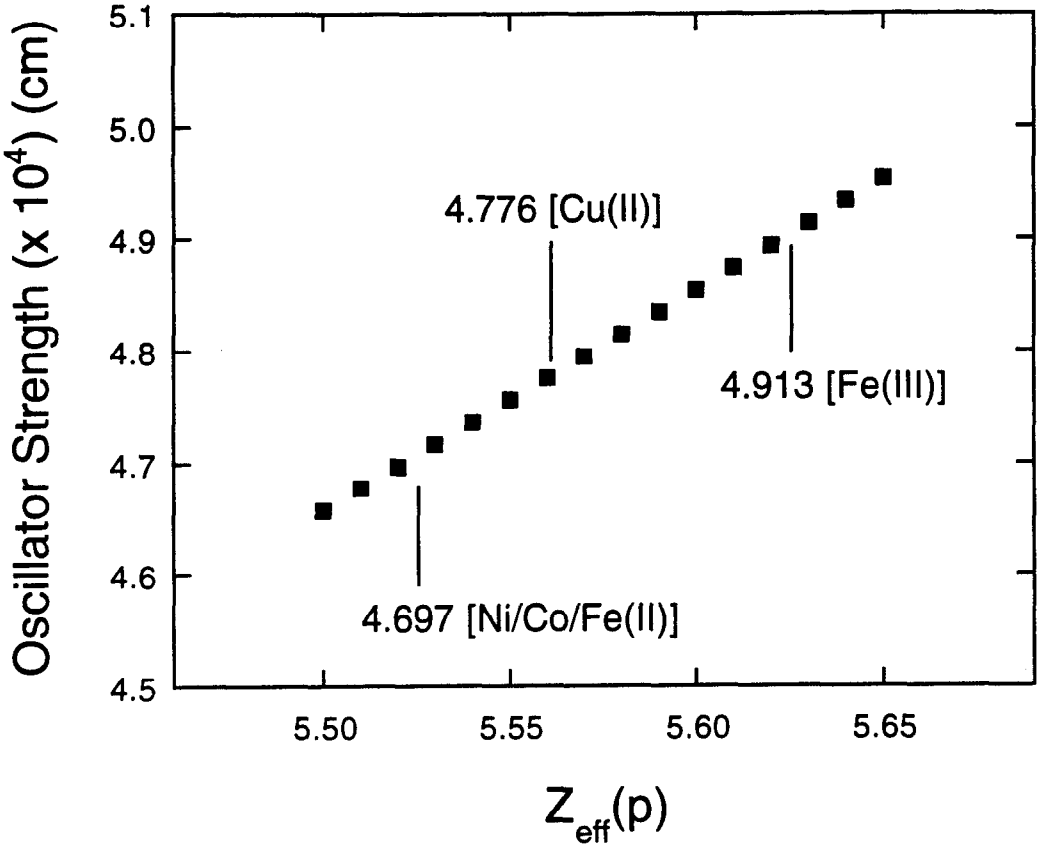

Figure 5.5. The oscillator strength of the Cl 1s —> 3p transition intensity *vs.* $Z_{eff}(p)$, the effective charge of the Cl 3p orbital. In this range of $Z_{eff}(p)$, the relationship is nearly linear. The value of $Z_{eff}(s)$, the effective charge of the Cl 1s orbital, is fixed at 16.7 as calculated by Slater's rules. The $Z_{eff}(p)$ are calculated from Slater's rules and the experimentally determined charge (Table 5.3). The oscillator strength is 4.697 for Cl bound to Ni, Co, and Fe(II), 4.776 for Cl in $Cu(II)Cl_4^{2-}$ and 4.913 (x 10^4 cm) for Cl in $Fe(III)Cl_4^-$.

Table 5.14. Summary of SCF-Xα-SW Calculations of MCl_4^{n-} Complexes

T_d Complex	Total % Cl-character in Metal d-derived Orbitals	Cl 3p Character as a Fraction of Total Cl	% Cl 3p-character in Metal d-derived Orbitals	Cl 3p-covalency Observed in Total Multiplet Intensity (%)
$CuCl_4^{2-}$ (D_{2d})	30	0.95	28.2 $(= c_1^2 + c_2^2)$	28.2
$NiCl_4^{2-}$	19	0.88	16.7 $(= c_1^2 + c_2^2)$	16.7
$CoCl_4^{2-}$	16	0.77	12.3 $(= c_1^2 + c_2^2)$	12.3
$Fe(II)Cl_4^{2-}$ (t_2)	15	0.68	10.2 $(= c_1^2 + c_2^2)$	12.4 $(= c_1^2 + c_2^2 + \frac{1}{3} c_3^2)$
(e)	10	0.65	6.5 $(= c_3^2)$	
$Fe(III)Cl_4^-$ (t_2)	26	0.86	22.4 $(= c_1^2 + c_2^2)$	35.3 $(= c_1^2 + c_2^2 + \frac{2}{3} c_3^2)$
(e)	23	0.84	19.3 $(= c_3^2)$	

In these calculations the remainder of the total Cl character in the t_2 and e-sets (that which is not 3p) is delocalized into diffuse, $\ell = 2$ orbitals. If the calculations are repeated with $\ell_{max} = 1$ for the Cl ligands, this $\ell = 2$ electron density is shifted onto the metal.

For comparison with the experimental covalency analysis, the covalencies from the Xα calculations must be correlated to that which is reflected in the multiplet intensity: $[c_1^2 + c_2^2]$ for Cu(II), Ni(II), and Co(II), $[c_1^2 + c_2^2 + \frac{1}{3} c_3^2]$ for Fe(II), and $[c_1^2 + c_2^2 + \frac{2}{3} c_3^2]$ for Fe(III). These sums are included in Table 5.14. Comparison of the calculated covalency values (Table 5.14, last column) to the experimentally determined covalencies (Table 5.13, last column) shows the results to be in agreement within ~5%.

5.5. Discussion

5.5.1. Factors Which Determine Pre-edge Intensity

From analysis of ligand K-edge XAS of a series of first row transition metal MCl_4^{n-} complexes, three factors which contribute to pre-edge transition intensity have been defined: the statistical probability of the occurrence of a pre-edge transition, the degree of excited state mixing in intermediate-strength ligand fields, and the HOMO covalency of the site. Each of these contributions is discussed below in greater detail.

Pre-edge intensity is related to the statistical probability of an allowed pre-edge transition. This is reflected in the dipole strength expressions derived for the complexes in these studies. The dipole strength expressions in Table 5.11 for T_d Cu(II), Ni(II) and Co(II) predict an intensity ratio of 1:2:3 (everything else being equal), in proportion to the number of t_2 holes in the ground state of each metal. The dipole strength of T_d Fe(II) and Fe(III) centers follow a similar trend for ground state holes in the t_2 and e-set. Thus, the more orbital vacancies to which spin-allowed transitions are possible, the more intense the pre-edge feature. Figure 5.6a shows theoretical Cl K-edge spectra for each of the complexes in this study as they would appear in the strong field limit (*e.g.*, no mixing) if the covalency were constant over the series. The covalency of each site is fixed at 0.30 for the t_2-set, with the e-set covalency in $Fe(II)Cl_4^{2-}$ and $Fe(III)Cl_4^{-}$ fixed at the ratios obtained from Xα calculations. The total intensity predicted by the dipole strength is modeled by the FWHM x Ht of each the features, using the same FWHM for all transitions. The pre-edge transition intensity increases by 1:2:3 for Cu(II):Ni(II): $Co(II)Cl_4^{2-}$, a result which reflects the statistical probability of the occurrence of a

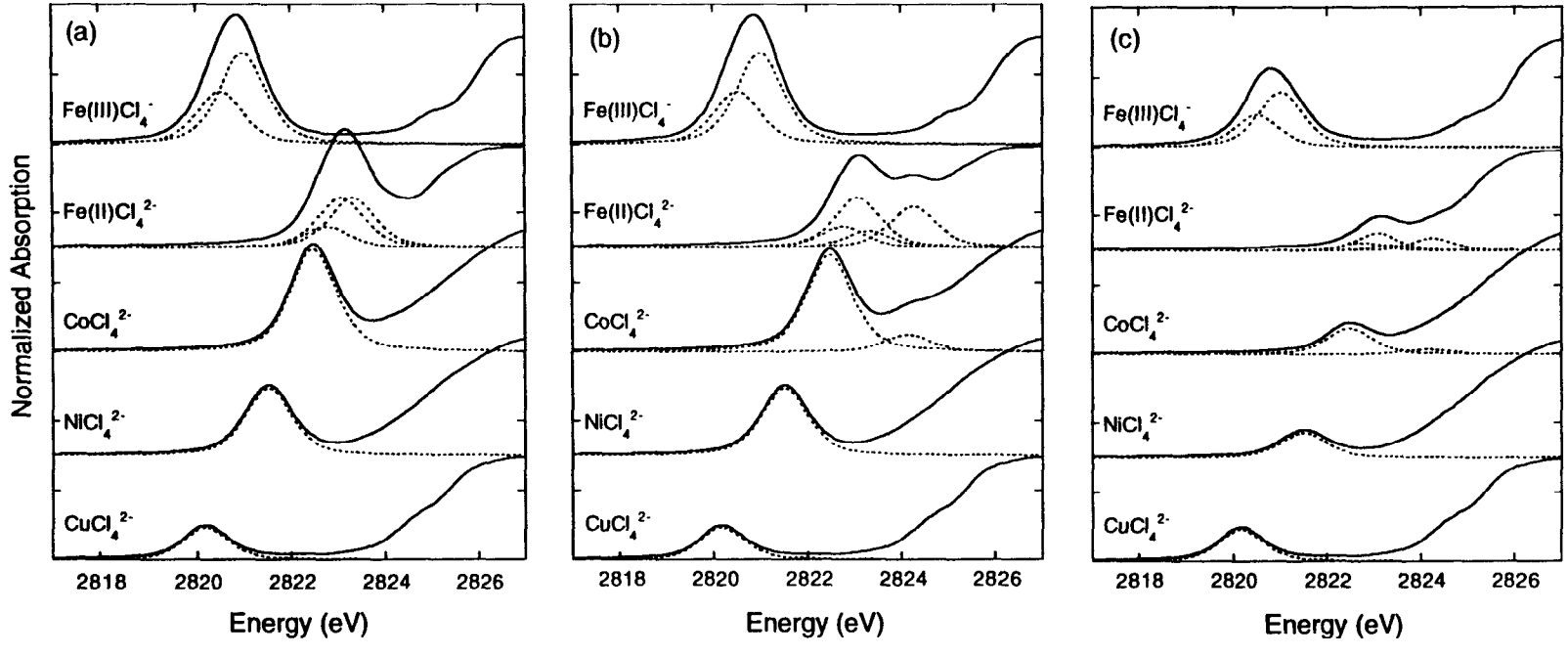

Figure 5.6. (a) Theoretical Cl K-edge XAS spectra of MCl_4^{n-} complexes with i) constant t_2-set covalency (30% Cl), ii) e-set covalency fixed with the ratio determined from Xα calculations and iii) no intermediate ligand field mixing of states. (b) Theoretical Cl K-edge XAS spectra of MCl_4^{n-} complexes with constant t_2-set covalency (30% Cl), ii) e-set covalency fixed with the ratio determined from Xα calculations and iii) intermediate-strength ligand field mixing of states. (c) Experimental Cl K-edge XAS spectra of MCl_4^{n-} complexes.

pre-edge transition for each metal complex. The $Fe(II)Cl_4^{2-}$ pre-edge is somewhat more intense than the $Co(II)Cl_4^{2-}$ (and $Fe(III)Cl_4^{-}$ is more intense than $Fe(II)Cl_4^{2-}$) due to the additional contributions from transitions to the e-set.

The second contribution to pre-edge feature intensity is mixing between excited states in intermediate-strength ligand fields. This mixing lowers the observed pre-edge intensity by distributing some of the pre-edge intensity to higher energy. Figure 5.6b shows theoretical Cl K-edge spectra as they would appear for complexes with the same covalency, with the added effect of excited state mixing in intermediate-strength ligand fields. The magnitude of mixing is that determined in Section 5.4.2.3 and the covalency is as above for Figure 5.6a. The intensity of the pre-edge in $CuCl_4^{2-}$, $NiCl_4^{2-}$, and $Fe(III)Cl_4^{-}$ is the same as in Figure 5.6a, but the intensity of pre-edges in both $CoCl_4^{2-}$ and $Fe(II)Cl_4^{2-}$ is reduced by ~16 and ~35%, respectively, due to higher state mixing. Note that if the covalency were as high as it is fixed to be in these spectra, the $Fe(II)Cl_4^{2-}$ spectrum would exhibit a second, higher energy pre-edge feature.

The final contribution to the pre-edge intensity in ligand K-edges comes from the covalency of ligand 3p character in the metal d-derived orbitals of the complex. The experimental data is shown in Figure 5.6c (on the same scale as in Figure 5.6a and 5.6b). While the statistical probability of a pre-edge transition increases (Figure 5.6a), the covalency decreases across the series from Cu(II) to $Fe(II)Cl_4^{2-}$. Thus, the total observed pre-edge intensity does not vary significantly across the divalent series. Further, between Fe(III) and Fe(II), it is primarily the increase in covalency (augmented by an additional electronic transition to the e-set) which effects the significant increase in pre-edge intensity observed in the spectrum of $Fe(III)Cl_4^{-}$.

Both the statistical probability of the occurrence of a pre-edge transition and the intermediate-strength ligand field excited state mixing can be calculated and their effect on pre-edge intensity determined. Thus, experimental pre-edge intensity which has had these factors taken into account provides a direct probe of the ligand 3p character in the metal d-derived orbitals of a ligand-metal complex.

5.5.2. Covalency in MCl_4^{n-} Complexes

The methodology presented herein allows us to relate ligand XAS pre-edge intensity to metal d-derived orbital covalency in a series of T_d metal-tetrachloride systems. The results are understood in terms of the energetics of bonding. The amount of Cl 3p character in each antibonding HOMO in the series is determined by the difference in energy between the metal d-orbitals and the Cl 3p orbitals. Covalency will

be greatest when the metal d- and Cl 3p-orbitals are closest in energy. Thus, the variations observed in covalency can be correlated with the effective charge on the metal. For increased effective nuclear charge on the metal, the d-orbitals are at deeper binding energy. Analysis of the pre-edge and edge energies of the Cl K-edge spectra shows the d-manifold of the metal centers varies in the order Cu(II) < Ni(II) < Co(II) < Fe(II) and Fe(III) << Fe(II).

For complexes with only t_2-vacancies, the t_2-set covalency is greatest in $CuCl_4^{2-}$, which has the deepest d-manifold energy. The t_2-set covalency is least in $Co(II)Cl_4^{2-}$, which has the highest d-manifold energy. The difference in t_2-set covalency between $CuCl_4^{2-}$ and $NiCl_4^{2-}$ (~30% vs. ~12%) is larger than the difference between $NiCl_4^{2-}$ and $CoCl_4^{2-}$ (12% vs. 9%). This is consistent with the d-manifold energy differences which are 1.5 eV between $CuCl_4^{2-}$ and $NiCl_4^{2-}$ and only 0.7 eV between $NiCl_4^{2-}$ and $CoCl_4^{2-}$. Based on the t_2-set covalency trend in Cu(II)-Ni(II)-$Co(II)Cl_4^{2-}$, and on the fact that the Fe(II) d-manifold is less deep in binding energy than in Co(II) by 0.6 eV, it is reasonable to anticipate that the t_2 covalency in $Fe(II)Cl_4^{2-}$ is somewhat less than in $Co(II)Cl_4^{2-}$, in agreement with $X\alpha$ calculations (Table 5.14). The remaining covalency reflected in the pre-edge intensity of $Fe(II)Cl_4^{2-}$ can be attributed to the additional contribution due to the partially unoccupied e-set.

The difference between the HOMO covalencies obtained for $Fe(III)Cl_4^-$ and $Fe(II)Cl_4^{2-}$ can also be related to the energetics of bonding. The d-manifold of the Fe(III) ion is 3.4 eV deeper than in Fe(II) due to increased effective nuclear charge and is closer to the Cl 3p-orbitals. Both the e- and t_2-set covalency in $Fe(III)Cl_4^-$ is thus increased relative to $Fe(II)Cl_4^{2-}$ because of the increased interaction between the metal d- and ligand p-orbitals.

5.6. Summary

Ligand K-edge X-ray absorption spectroscopy has been shown to be a powerful tool in the study of the electronic structures of ligand-metal interactions in open shell metal ions. The technique was developed previously for application to ligand-Cu(II) covalency, but has now been extended for application to metal ions with more than one electron (or hole). Using the expressions derived and the protocol outlined in this study, ligand pre-edge intensity provides a direct probe of the ligand valence p-orbital covalency of a metal-ligand bond. The technique is extended to other d^n systems by application of the analysis presented in this paper.

Ligand K-edges have already been successfully analyzed to quantitate the covalency in the active site electronic structure of blue copper-containing proteins.[2] With the extension of the technique to other d^n metal centers, this work provides the basis for analyses of other metalloproteins and will be of particular importance in the study of bonding in iron-sulfur and related proteins.

5.7. Acknowledgments

This research was supported by NSF CHE-9217628 (E.I.S.) and CHE91-21576 (K.O.H.) and by NIH RR 01209 (K.O.H). SSRL operations are funded by the Department of Energy, Office of Basic Energy Sciences. The Biotechnology Program is supported by the NIH, Biomedical Research Technology Program, National Center for Research Resources. Further support is provided by the Department of Energy, Office of Health and Environmental Research.

5.8. References and Notes

(1) Hedman, B.; Hodgson, K. O.; Solomon, E. I. *J. Am. Chem. Soc.* **1990**, *112*, 1643-1645.

(2) Shadle, S. E.; Penner-Hahn, J. E.; Schugar, H. J.; Hedman, B.; Hodgson, K. O.; Solomon, E. I. *J. Am. Chem. Soc.* **1993**, *115*, 767-776.

(3) Shadle, S. E.; Hedman, B.; Hodgson, K. O.; Solomon, E. I. *Inorg. Chem.* **1994**, in press.

(4) The geometry of the $CuCl_4^{2-}$ complex in this study is D_{2d}. This geometric distortion from T_d will be addressed as necessary throughout the text.

(5) McGinnety, J. A. *J. Am. Chem. Soc.* **1972**, *94*, 8406-8412.

(6) Sharnoff, M. *J. Chem. Phys.* **1965**, *42*, 3383-3395.

(7) Gill, N. S.; Taylor, F. B. *Inorg. Synth.* **1967**, *9*, 136-142.

(8) Hedman, B.; Frank, P.; Gheller, S. F.; Roe, A. L.; Newton, W. E.; Hodgson, K. O. *J. Am. Chem. Soc.* **1988**, *110*, 3798-3805.

(9) Lytle, F. W.; Greegor, R. B.; Sandstrom, D. R.; Marques, E. C.; Wong, J.; Spiro, C. L.; Huffman, G. P.; Huggins, F. E. *Nucl. Instr. Meth.* **1984**, *226*, 542-548.

(10) Stern, E. A.; Heald, S. M. *Rev. Sci. Instrum.* **1979**, *50*, 1579-1582.

(11) Argonne National Laboratory; B. S. Garbow, K. E. Hillstrom, J. J. More.

(12) Agarwal, B. K. *X-ray Spectroscopy*; Springer-Verlag: Berlin, 1979, pp 276ff.

(13) Tyson, T. A.; Roe, A. L.; Frank, P.; Hodgson, K. O.; Hedman, B. *Phys. Rev. B* **1989**, *39A*, 6305-6315.

(14) Lytle, F. W. In *Applications of Synchrotron Radiation*; Winick, H.; Xian, D.; Ye, M. H.; Huang, T., Ed.; Gordon & Breach: New York, 1989; pp 135.

(15) Gewirth, A. A.; Cohen, S. L.; Schugar, H. J.; Solomon, E. I. *Inorg. Chem.* **1987**, *26*, 1133-1146.

(16) Cook, M.; Case, D. A. *QCPE Program #465* **1991**, *23*, 21-22.

(17) Pauling, P. *Inorg. Chem.* **1966**, *5*, 1498-1505.

(18) Both the Ni and Co complexes used in this study have the same counterion. Since the Co-Cl bond length is not known, the Co-Cl distance was set to the Ni-Cl distance + 0.01 Å based on the fact that in the (Et_4N) and (Me_4N) salts, the Co-Cl bond length was ~0.01-0.02 Å longer than the Ni-Cl distance.

(19) Lauher, J. W.; Ibers, J. A. *Inorg. Chem.* **1975**, *14*, 348-352.

(20) Cotton, F. A.; Murillo, C. A. *Inorg. Chem.* **1975**, *14*, 2467-2469.

(21) Schwarz, K. *Phys. Rev. B* **1972**, *5*, 2466-2468.

(22) Karshipin, T. B.; Gebhard, M. S.; Solomon, E. I.; Raymond, K. N. *J. Am. Chem. Soc.* **1991**, *113*, 2977-2984.

(23) Griffith, J. S. *The Irreducible Tensor Method for Molecular Symmetry Groups*; Prentice-Hall: Englewood Cliffs, NJ, 1962, pp 1-427.

(24) Piepho, S. B.; Schatz, P. N. *Group Theory in Spectroscopy*; Wiley: New York, 1983.

(25) The correlations between allowed excited states and d^{n+1} parent excited states given in Table 5.5d for Fe(II)Cl_4^{2-} are as follows. For transitions to the t_2-set in Fe(II)Cl_4^{2-} there are two parent excited states, $^4T_1$ and $^4T_2$, constructed from the et_2^2 (d^{n+1}) excited configuration, each of which gives rise to allowed $^5T_1$ and $^5T_2$ final states upon coupling of the ligand a_1 and t_2 holes. The analysis described herein does not trace the $^5T_1$ and $^5T_2$ excited states through these et_2^2 parent states, but rather (see equation 5.4) requires the states formed from the core holes and t_2-holes ($a_1^1t_2^2$ and $t_2^1t_2^2$) be constructed first and then the e-hole to be coupled in. In order to determine which $^5T_1$ and $^5T_2$ final states derive from which et_2^2 (d^{n+1}) parent states, the final state wavefunctions were constructed for both cases according to the method of Piepho and Schatz[24] (equation 19.7.6, p. 430) and the projection of these ($a_1^1t_2^2$ or $t_2^1t_2^2$) states onto the appropriate d^{n+1} parent was determined.

(26) Ballhausen, C. J.; Gray, H. B. *Molecular Orbital Theory*; Benjamin Press: New York, 1964, pp 108-109.

(27) Van Der Avoird, A.; Ros, P. *Theoret. Chim. Acta* **1966**, *4*, 13-21.

(28) Wiers, B. H.; Reynolds, W. L. *Inorg. Chem.* **1966**, *5*, 2016-2021.

(29) Bird, B. D.; Day, P. *J. Chem. Phys.* **1968**, *49*, 392-403.

(30) Any one of the appropriate one-electron matrix elements in Table 5.8 will yield the same solution for the one-electron reduced matrix element using equation 5.2' and the substitution $< s \mid \mathbf{r}(x') \mid p_{x'} > = < s \mid \mathbf{r}(y') \mid p_{y'} > = < s \mid \mathbf{r} \mid p_{\pi'} >$.

(31) The $CuCl_4^{2-}$ geometry is actually D_{2d}. This analysis can be lowered to D_{2d} using the chain of groups methodology[24] in which the coupling of states of lower symmetry is given by (reference 24, equation 15.3.4)

$$\left(aa_1, bb_1 \mid cc_1\right)^{G \supset G_1} = H(abc)\frac{|c|^{1/2}}{|c_1|^{1/2}}\begin{pmatrix} c \\ c_1 \end{pmatrix} G G_1 \begin{pmatrix} a & b & c \\ a_1 & b_1 & c_1 \end{pmatrix} G G_1 \qquad \text{(a)}$$

Where a,b,c are states of the higher symmetry group G and a_1, b_1, and c_1 are states of G_1 (the next lowest state along the chain of groups with successively lower symmetry) and $H(abc)$ is a phase factor. For D_{2d} $CuCl_4^{2-}$ G is a state in T_d symmetry and G_1 is the state in D_{2d}. The integrals in the lower symmetry group are then given by

$$\left\langle aa_1 \middle| cc_1 \middle| bb_1 \right\rangle^{G \supset G_1} = \begin{pmatrix} a \\ a_1 \end{pmatrix} \begin{pmatrix} a & b & c \\ a_1 & b_1 & c_1 \end{pmatrix} \left\langle a \middle\| c \middle\| b \right\rangle^G \qquad \text{(b)}$$

Lowering the symmetry to D_{2d} results in a splitting of the t_2 HOMO set into b_2 (HOMO) + e-orbitals and the ligand core holes into $a_1 + b_2 + e$. The application to the case of D_{2d} $CuCl_4^{2-}$ thus involves rewriting the integrals of the T_d analysis as

T_d integrals	D_{2d} integrals chain of groups notation	D_{2d} integrals
$< A_1 \mid T_2 \mid T_2 >$	$< A_1\, A_1 \mid T_2\, B_2 \mid T_2\, B_2 >^{T_d \supset D_{2d}^*}$	$< A_1 \mid B_2 \mid B_2 >^{D_{2d}^*}$
	$< A_1\, A_1 \mid T_2\, E \mid T_2\, E >^{T_d \supset D_{2d}}$	$< A_1 \mid E \mid E >^{D_{2d}}$
$< T_2 \mid T_2 \mid T_2 >$	$< T_2\, E \mid T_2\, E \mid T_2\, B_2 >^{T_d \supset D_{2d}^*}$	$< E \mid E \mid B_2 >^{D_{2d}^*}$
	$< T_2\, E \mid T_2\, B_2 \mid T_2\, E >^{T_d \supset D_{2d}}$	$< E \mid B_2 \mid E >^{D_{2d}}$
	$< T_2\, B_2 \mid T_2\, E \mid T_2\, E >^{T_d \supset D_{2d}}$	$< B_2 \mid E \mid E >^{D_{2d}}$

Since the ground state is B_2 for D_{2d} $CuCl_4^{2-}$, only the first integral in each set (noted with an asterisk [*]) will actually contribute to the dipole strength of a pre-edge transition. Each of these integrals is evaluated using equation (b) to obtain

D_{2d} integral	Is equal to
$\langle A_1\ A_1 \mid T_2\ B_2 \mid T_2\ B_2 \rangle^{Td} \supset D_{2d}$	$\frac{1}{\sqrt{3}} \langle A_1 \| T_2 \| T_2 \rangle^{Td}$
$\langle T_2\ E \mid T_2\ E \mid T_2\ B_2 \rangle^{Td} \supset D_{2d}$	$\frac{1}{\sqrt{3}} \langle T_2 \| T_2 \| T_2 \rangle^{Td}$

The many-electron reduced matrix elements $\langle A_1 \| T_2 \| T_2 \rangle^{Td}$ and $\langle T_2 \| T_2 \| T_2 \rangle^{Td}$ have been evaluated in the Analysis Section of this manuscript (See Table 5a). The dipole strength of the D_{2d} $CuCl_4^{2-}$ can thus be calculated to be $\frac{1}{3} R^2 (c_1^2+c_2^2) \langle Cl\ 1s \mid \mathbf{r} \mid 3p \rangle^2$ which is identical to the result obtained in T_d symmetry.

Xα calculations of the T_d and D_{2d} $CuCl_4^{2-}$ complexes indicate that while the relative σ- and π-covalencies contributions vary, the *total* covalency which is distributed into b_2 and e-sets in D_{2d} is the same as the covalency in the T_d t_2-set. Thus, the analysis herein which calculates $CuCl_4^{2-}$ t_2-covalency using the T_d D_o expression is equivalent to an analysis in D_{2d} which gives the covalency of the b_2-orbital.

(32) Dunn, T. M.; McClure, D. S.; Pearson, R. G. *Some Aspects of Crystal Field Theory*; Harper & Row: New York, 1965, pp 42-45.

(33) Ferguson, J. *Prog. Inorg. Chem.* **1970**, *12*, 159-293.

(34) Support for the pre-edge assignment in Fe(III)Cl_4^- is given by the FWHMs required to fit the data. The FWHM of a pre-edge transition is dependent on the resolution of the experiment and on the core-hole lifetime of the Cl 1s hole, both of which should be relatively constant across this series. In each of the M(II)Cl_4^{2-} spectra the FWHM required to fit the data ranged between 1.04-1.18 eV, while the FWHM required to fit the Fe(III)Cl_4^- was 1.32-1.44 eV. When one function was replaced with two (with the appropriate intensity ratios and energy splitting fixed) in Fe(III)Cl_4^- (Figure 5.4e), the FWHM of each of the two transitions which reproduced the data in the pre-edge region ranged between 1.12-1.22 eV, in better agreement with the FWHM of the rest of the series.

(35) The Cl 1s —> 4p dipole strength for each case, in terms of one-electron reduced matrix elements, is $D_o = 2/3\ [\langle a_1 \| t_2 \| t_2 \rangle^2 + \langle t_2 \| t_2 \| a_1 \rangle^2 + \langle t_2 \| t_2 \| t_2 \rangle^2]$.

(36) Solomon, E. I. *Comments Inorg. Chem.* **1984**, *3*, 297-299.

(37) Karplus, M.; Porter, R. N. *Atoms and Molecules*; W. A. Benjamin, Inc.: Menlo Park, CA, 1970, pp 229.

Chapter 5

5.9. Appendix

Table S5.1. Valence Orbitals from SCF-Xα-SW Calculation of D_{2d} $CuCl_4^{2-}$

					% for Cl		
State	Level	Energy (eV)	Ni (%)	Cl (%)	s	p	d
15	$4B_2$	-3.284	70	30	1	94	4
24	5E	-3.834	74	26	0	96	4
10	$2B_1$	-4.132	75	25	0	92	8
19	$4A_1$	-4.202	74	26	0	95	5
11	$1A_2$	-4.989	4	97	0	100	0
23	4E	-5.156	6	94	0	100	0
18	$3A_1$	-5.831	30	70	0	99	1
14	$3B_2$	-5.849	14	86	0	100	0
22	3E	-6.005	21	79	0	99	1
9	$1B_1$	-6.327	31	69	0	99	1
21	2E	-6.837	37	63	0	98	1
13	$2B_2$	-7.023	45	55	0	97	2
17	$2A_1$	-7.651	34	66	0	95	2
12	$1B_2$	-17.480	13	87	99	0	0
20	1E	-17.546	13	88	99	1	0
16	$1A_1$	-17.845	16	85	98	1	0

Sphere radii (in Bohr units) for calculation: Cu = 3.11, Cl = 2.49

Table S5.2. Valence Orbitals from SCF-Xα-SW Calculation of T_d $NiCl_4^{2-}$

					% for Cl		
State	Level	Energy (eV)	Ni (%)	Cl (%)	s	p	d
17	$4T_2$	-3.032	81	19	1	88	10
10	2E	-3.477	85	15	0	84	16
11	$1T_1$	-5.353	4	96	0	100	0
16	$3T_2$	-5.992	14	86	0	100	0
9	1E	-6.083	20	80	0	99	1
15	$2T_2$	-6.839	33	67	1	98	1
13	$2A_1$	-7.588	32	68	3	96	2
14	$1T_2$	-17.619	10	90	99	0	0
12	$1A_1$	-17.862	13	87	99	1	0

Sphere radii (in Bohr units) for calculation: Ni = 3.11, Cl = 2.49

Table S5.3. Valence Orbitals from SCF-Xα-SW Calculation of T_d $CoCl_4^{2-}$

					% for Cl		
State	Level	Energy (eV)	Co (%)	Cl (%)	s	p	d
17	$4T_2$	-2.268	84	16	2	77	21
10	2E	-2.680	89	11	0	73	27
11	$1T_1$	-5.398	4	96	0	100	0
16	$3T_2$	-5.993	12	88	0	100	0
9	1E	-6.059	15	85	0	100	0
15	$2T_2$	-6.785	30	70	1	98	1
13	$2A_1$	-7.533	31	69	2	96	1
14	$1T_2$	-17.642	10	90	99	0	0
12	$1A_1$	-17.872	12	88	99	1	0

Sphere radii (in Bohr units) for calculation: Co = 3.11, Cl = 2.49

Table S5.4. Valence Orbitals from SCF-Xα-SW Calculation of T_d $FeCl_4^{2-}$

					% for Cl		
State	Level	Energy(eV)	Fe (%)	Cl (%)	s	p	d
17	$4T_2$	-1.773	85	15	2	68	29
10	2E	-2.177	90	10	0	65	35
11	$1T_1$	-5.473	4	96	0	100	0
16	$3T_2$	-6.044	11	89	0	100	0
9	1E	-6.107	13	87	0	100	0
15	$2T_2$	-6.823	29	71	1	98	1
13	$2A_1$	-7.542	30	70	2	96	1
14	$1T_2$	-17.700	10	90	100	0	0
12	$1A_1$	-17.918	12	88	99	1	0

Sphere radii (in Bohr units) for calculation: Fe = 3.11, Cl = 2.49

Table S5.5. Valence Orbitals from SCF-Xα-SW Calculation of T_d $FeCl_4^-$

					% for Cl		
State	Level	Energy (eV)	Fe (%)	Cl (%)	s	p	d
17	$4T_2$	-3.885	74	26	1	86	13
10	2E	-4.540	77	23	0	84	16
11	$1T_1$	-6.476	4	96	0	100	0
16	$3T_2$	-7.259	14	86	0	99	1
9	1E	-7.497	26	74	0	99	1
15	$2T_2$	-8.646	35	65	2	96	2
13	$2A_1$	-9.229	29	71	4	93	3
14	$1T_2$	-19.084	11	89	99	1	0
12	$1A_1$	-19.410	14	86	98	1	1

Sphere radii (in Bohr units) for calculation: Fe = 2.90, Cl = 2.49